

Towards near-atomic resolution imaging of microsecond nanoscale dynamics

Présentée le 3 mars 2023

Faculté des sciences de base
Laboratoire de nanodynamique moléculaire
Programme doctoral en chimie et génie chimique

pour l'obtention du grade de Docteur ès Sciences

par

Gabriele BONGIOVANNI

Acceptée sur proposition du jury

Prof. J. Vanicek, président du jury
Prof. U. Lorenz, directeur de thèse
Prof. D. Flannigan, rapporteur
Prof. A. Kirkland, rapporteur
Prof. H. Stahlberg, rapporteur

Abstract

Time-resolved electron microscopy has made significant progress in recent years, with some groups now working on instruments that offer attosecond temporal resolution. While much of the research in the field revolves around the improvement of temporal resolution, atomic-resolution imaging of nanoscale dynamics has remained elusive.

This thesis describes the development of two methods for time-resolved electron microscopy which afford near-atomic spatial resolution. The first consists of a modification of a commercial transmission electron microscope to generate bright and intense microsecond electron pulses, which are then used to image fast and irreversible nanoscale dynamics with atomic resolution (Chapters 2 and 3). The second is a novel approach to time-resolved cryo-electron microscopy which boosts the temporal resolution to the microsecond timescale (Chapters 4 and 5).

Chapter 2 describes the irradiation of a Schottky emitter with microsecond laser pulses. The temperature of the filament rises to extreme values for brief periods of time, causing a significant increase in emission current. Even though the temperatures reached by the filament tip during laser irradiation are well beyond the maximum value recommended by the manufacturer, we show that the brief and localized heating provided by the focused laser pulse provides a way to extract large currents without damaging the filament.

An electrostatic deflector, placed below the accelerator, chops the laser-boosted electron beam into microsecond pulses, as described in Chapter 3. We show that a 5 μ s pulse generated with this method is brighter than the continuous electron beam and can be used to capture an atomic-resolution image of a gold nanoparticle in a single shot. Two possible applications of these pulses are then discussed. Drift-corrected imaging, especially in the

presence of large amounts of drift, is significantly improved when bright electron pulses are used instead of the continuous beam. In addition, these pulses can be employed to capture irreversible dynamics occurring on the microsecond timescale with atomic spatial resolution. Chapter 4 provides details of a novel method for microsecond time-resolved cryo-electron microscopy. The high temporal resolution is achieved by irradiating a cryo specimen with a laser beam, causing it to locally melt. The embedded biomolecules can undergo dynamics in liquid until the laser is switched off, at which point the sample revitrifies within a few microseconds trapping particles in their intermediate configurations. The chapter shows that it is possible to obtain a near-atomic resolution reconstruction from revitrified sample areas, and the result looks identical to a map obtained from conventional sample areas. In addition, the projection angles are more uniformly distributed after revitrification.

Chapter 5 shows that it is not necessary to modify a transmission electron microscope to perform melting and revitrification experiments on a cryo sample. The chapter introduces a simplified setup, requiring an optical microscope, that allows performing such experiments and verify their outcome on the fly. We present the advantages and disadvantages of this new setup, in the hope it will encourage the adoption of our method by other research groups and boost the development of microsecond time-resolved cryo-electron microscopy.

Keywords: time-resolved electron microscopy, single-shot imaging, high-resolution TEM, time-resolved cryo-EM, microsecond protein dynamics, laser irradiation of cryo samples

Abstract (Italiano)

La microscopia ultraveloce si è sviluppata considerevolmente negli ultimi decenni. La ricerca, tuttavia, si è concentrata principalmente sul miglioramento della risoluzione temporale, trascurando quella spaziale. Per questo motivo, studi dinamici con risoluzione atomica non sono stati adeguatamente esplorati.

Questa tesi descrive due metodi per lo studio di processi dinamici con risoluzione atomica. Il primo consiste nella modifica di un microscopio elettronico a trasmissione, per generare impulsi di elettroni con cui catturare processi irreversibili con risoluzione atomica (Capitoli 2 e 3). Il secondo è un nuovo metodo per la microscopia crioelettronica che consente di catturare processi con una risoluzione di pochi microsecondi (Capitoli 4 e 5).

Il Capitolo 2 descrive l'illuminazione di un emettitore Schottky con impulsi laser della durata di 100 microsecondi. La temperatura del filamento raggiunge valori estremi per brevi periodi, causando un grosso aumento della corrente. Nonostante la temperatura superi di gran lunga il valore massimo consigliato dal fabbricante, dimostriamo che l'aumento è localizzato e non danneggia il filamento.

Il fascio di elettroni, dopo essere stato intensificato grazie all'irradiazione laser, viene diviso in impulsi grazie all'effetto di deflettori elettrostatici inseriti al di sotto dell'acceleratore, come descritto nel Capitolo 3. Mostriamo come un singolo impulso di elettroni della durata di 5 μs può essere usato per catturare un'immagine di una nanoparticella d'oro con risoluzione atomica. Questi impulsi possono trovare applicazione in diversi settori. Per esempio, dimostriamo come sia possibile catturare immagini con risoluzione atomica anche in presenza di rapidi movimenti del campione, che sarebbero troppo elevati per un fascio di elettroni continuo. Inoltre, utilizziamo questi impulsi per catturare la trasformazione irreversibile di un nanocristallo in un solido amorfo con risoluzione atomica.

Il Capitolo 4 descrive un nuovo metodo per la microscopia crioelettronica che garantisce risoluzione del microsecondo. Tale risoluzione è possibile illuminando un campione a temperature criogeniche con un impulso laser, causando uno scioglimento localizzato. Le biomolecole nel campione hanno così modo di muoversi nel liquido fintantoché il laser rimane attivo. Alla fine dell'impulso, il campione rivitrifica in pochi microsecondi, intrappolando le biomolecole in transizione tra diverse configurazioni. Il capitolo dimostra come il metodo non danneggi le proteine; è infatti possibile ottenere una ricostruzione dell'apoferritina con risoluzione quasi atomica a partire da immagini catturate in aree illuminate dal laser. Il risultato è identico a una ricostruzione ottenuta a partire da aree convenzionali. Inoltre, mostriamo come il metodo che proponiamo sia in grado di omogeneizzare gli angoli con cui la biomolecola si orienta nel campione.

Il Capitolo 5 dimostra che non è necessario modificare un microscopio elettronico a trasmissione per rivitrificare accuratamente un campione criogenico. Il capitolo introduce un setup sperimentale, che consente di eseguire i nostri esperimenti e verificarne il successo usando un microscopio ottico.

Presentiamo vantaggi e svantaggi del setup, nella speranza di incoraggiare l'adozione del nostro metodo da parte di altri gruppi di ricerca, accelerando così lo sviluppo della microscopia crioelettronica con risoluzione temporale del microsecondo.

Keywords: microscopia elettronica con sensibilità temporale, single-shot imaging, TEM ad alta risoluzione, cryo-EM con sensibilità temporale, dinamica delle proteine, illuminazione laser di campioni criogenici

Table of Contents

Abstract	1
Abstract (Italiano)	3
Chapter 1 – Introduction	7
1.1 Optical microscopy and its limits.....	7
1.2 Electron microscopy.....	8
1.3 (Single-particle) Cryo-electron microscopy.....	9
1.4 Time-resolved cryo-electron microscopy.....	10
1.5 In-situ TEM.....	11
1.6 Time-resolved electron microscopy.....	13
1.8 Outline.....	17
1.9 References.....	19
Chapter 2 - Intense Microsecond Electron Pulses from a Schottky Emitter	28
2.1 Introduction.....	28
2.2 Results and discussion.....	30
2.3 Conclusion.....	38
2.4 References.....	39
Chapter 3 - Atomic-Resolution Imaging of Fast Nanoscale Dynamics with Bright Microsecond Electron Pulses	44
3.1 Introduction.....	44
3.2 Results and discussion.....	46
3.3 Conclusions.....	57
3.4 Methods.....	59
3.5 References.....	62
Chapter 4 - Near-atomic resolution reconstructions from in situ revitrified cryo samples	65
4.1 Introduction.....	65
4.2 Results and discussion.....	67
4.4 Methods.....	72
4.5 References.....	74
Chapter 5 - Microsecond melting and revitrification of cryo samples with a correlative light-electron microscopy approach	77
5.1 Introduction.....	77
5.2 Results.....	79
5.3 Conclusions.....	85
5.4 Methods.....	88
5.5 References.....	90

Chapter 6 – Conclusions and outlook	94
6.1 References.....	98
Appendix I - Supporting information for Chapter 3.....	101
A1.1 Dose fractionated imaging with microsecond electron pulses in the presence of beam-induced drift	101
A1.2 Estimation of the energy spread.....	101
A1.3 Supplementary Figures	103
A1.4 References	108
Appendix II - Supporting information for Chapter 4.....	109
A2.1 Single-particle reconstructions.....	109
A2.2 Supplementary Figure	111
A2.3 References	112
Appendix III - Supporting information for Chapter 5.....	113
A3.1 Single-particle reconstructions.....	113
A3.2 Supplementary Figures	115
Acknowledgments.....	118
<i>Curriculum Vitae</i>.....	120

Chapter 1 – Introduction

1.1 Optical microscopy and its limits

The ability to visualize magnified objects has been a central scientific interest for centuries. Back in 1538, Italian physicist Girolamo Fracastoro wrote "If anyone should look through two spectacle glasses, one being superimposed on the other, they will see everything much larger and nearer".¹ The idea was realized shortly afterwards by Dutch spectacle makers Hans and Zacharias Jansen, with the birth of the first optical microscope dating to the late 16th century.² The instruments were initially used to study biological specimens, including plant, animal and human samples,^{3,4} giving rise to the field of microbiology. During the 17th and 18th centuries, optical microscopes enabled the observation of cell components and pathogens, laying the foundation for our current understanding of health and disease. The development of the theory of optics and diffraction in the nineteenth century considerably improved the resolving power of the instruments. It was during this time that German physicist Ernst Abbe put forward a theoretical limit for the minimum achievable resolution d :⁵

$$d = \frac{\lambda}{2n \sin \alpha} \quad (1.1)$$

with λ being the wavelength of light, n the refractive index of the medium used and α the convergence semi angle. Using wavelengths in the range of visible light, equation 1.1 suggests that an optical microscope cannot resolve details smaller than a few hundred nanometers. Abbe's limit is rooted in the physics of the diffraction process, so it cannot be overcome with better optical lenses.⁵ However, different approaches have been proposed to circumvent it. One idea is to avoid light diffraction entirely and instead build a map of the sample by studying the variation of some localized property. For example, a sharp tip in close proximity to the specimen surface experiences a variety of forces, including van der Waals, electrostatic and

capillary interactions. Measuring the variation of such forces across the specimen allows to generate a 3D representation of the surface. This is the principle behind atomic-force microscopy, which can achieve a lateral (X-Y) resolution of a few nm and sub-Ångstrom vertical resolution.⁶ In addition, quantum tunneling can be induced between the sample and the tip, if both are conductive. Since the tunneling current decays exponentially with the distance between the sample and the tip, this effect can be used to probe the surface of the sample with extremely high accuracy. This idea is at the core of scanning tunneling microscopy, which enables imaging of a surface at atomic-resolution.⁷

An alternative approach, in the framework of wave diffraction, is to employ waves with a shorter wavelength, to reduce the limit set by Abbe's equation. X-rays, characterized by a wavelength up to 100 000 times smaller than that of visible light, are now routinely used to determine the atomic structure of materials and biomolecules, and have revolutionized our understanding of biology at the molecular level.^{8,9}

1.2 Electron microscopy

Short wavelengths can also be obtained accelerating particles to velocities close to the speed of light. According to the de Broglie equation, a quantum particle with momentum p has a wavelength λ given by:¹⁰

$$\lambda = \frac{h}{p} \quad (1.2)$$

Where h is the Planck constant. Transmission electron microscopes (TEMs) are based on this principle. Compared to a conventional microscope, light is replaced by a beam of electrons, extracted from a cathode, and accelerated to high velocities (typically more than 50% of the

speed of light). Electron lenses, which exploit the Lorentz force to deflect the incoming beam, are used to form a magnified image of the specimen, similarly to their optical counterpart. While the wavelength of the electrons can be made as small as a few pm, the resolution limit of TEMs is typically defined by the aberrations of the lenses, the instabilities of the instrument and by the finite coherence of the electron beam. Nonetheless, continuous technological advances make it now possible to obtain images of the specimen with sub-Å resolution.^{11,12}

1.3 (Single-particle) Cryo-electron microscopy

In order to prevent electrons from scattering with gas molecules before reaching the specimen, the column of a transmission electron microscope is kept under high vacuum. This requirement poses a problem for samples that must be imaged in hydrated conditions, such as biomolecules.

In 1981 Jacques Dubochet published a paper proposing a novel method to image biological samples in an electron microscope.¹³ A liquid solution containing the biomolecules of interest is rapidly plunged into a recipient containing liquid ethane at 77 K. The fast cooling rate causes the sample to vitrify, without significantly perturbing the structure of the molecules under study. While imaging, the vitrified sample is kept at cryogenic temperatures, at which the vapor pressure of glassy water is negligible.¹⁴

In addition to the requirement for hydrated conditions, biological specimens are particularly sensitive to electron beam irradiation, and they unravel after being exposed to electron doses that are not sufficient to form a high-resolution image.¹⁵ The problem is typically overcome in single-particle cryo-electron microscopy (cryo-EM) by averaging images of tens of thousands of particles, each obtained keeping the electron dose to a minimum. These images usually

contain particles seen from different angles, which together can be used to form a 3D reconstruction using the projection-slice theorem.¹⁶

Over the decades since its inception, cryo-EM has developed tremendously, now rivaling X-ray crystallography in terms of number of protein structures solved per year.¹⁷ Recently, it enabled a 3D reconstruction of the spike protein of the SARS-CoV-2,^{18,19} a crucial result in the development of a vaccine for the Covid-19 pandemic.

1.4 Time-resolved cryo-electron microscopy

While static images are fundamental to understand the function of biomolecules, proteins are intrinsically dynamic machines.²⁰ At room temperature they possess sufficient thermal energy to continuously undergo conformational changes, which are associated with movements between minima in a multidimensional energy landscape.^{20,21} Various physiological events, such as ATP binding or pH changes, alter the topography of the energy landscape, biasing the otherwise random motion of proteins in the conformational space towards specific configurations.²¹ It is clear that our understanding of protein function is incomplete without a description of the associated energy landscape under various physiologically relevant conditions.

Cryo-EM is an optimal method to observe the innate structural heterogeneity of flexible proteins. While the crystallization process required for X-ray diffraction forces molecules to take specific conformations,²² the rapid plunge freezing method traps proteins in configurations that closely represent the room-temperature ensemble.¹⁴ Multiple functional states can be reconstructed at once from a single cryo specimen, and their relative occurrence

can be used to experimentally determine parts of the energy landscape.²³ In addition, novel deep-learning based models can now be used to predict the transient configurations between equilibrium states.^{24,25}

Time-resolved cryo-EM adds the temporal domain to the structural studies, enabling experimental observation of short-lived transitory states. Most commonly, a reaction of interest is initiated by rapidly mixing two reactants using a microfluidic device^{26,27} or employing a laser pulse to liberate a caged compound.²⁸ While the process unfolds, the reactants are sprayed onto a grid which is then plunged into the cryogen within a few milliseconds.²⁶ The rapid vitrification quenches the reaction and traps short-lived transient configurations in vitreous ice, where they can subsequently be imaged.^{26,29–31}

The temporal resolution of this method is ultimately determined by the vitrification speed. While different vitrification schemes offer cooling rates that are faster than those achieved through conventional plunge-freezing,³² the time required to cool an entire cryo-EM grid to cryogenic temperatures is around 1 ms,²⁶ too slow to observe a multitude of domain motions associated with protein function.²⁰

1.5 In-situ TEM

While time-resolved cryo-EM is a crucial tool to study the dynamics of biomolecules, in situ electron microscopy has enabled the direct observation of structural transformations in materials. Because nanomaterials do not need to be trapped in vitreous ice, dynamics can be directly initiated inside the electron microscope and imaged over the course of several seconds by recording frames in a movie-like fashion.

Several methods have been proposed to trigger dynamic processes within the electron microscope. Special specimen holders allow the sample to be heated,^{33,34} mechanically stressed,³⁵⁻³⁷ and electrically biased.^{38,39} In addition, specialized enclosed chips allow liquids^{40,41} and gases⁴²⁻⁴⁴ to flow within the microscope column, enabling real-time observation of chemical processes.

In recent years, in-situ experiments have revealed the mechanisms underlying the growth of nanomaterials in solution^{41,45-49} and the factors affecting their morphology.^{50,51} These insights provided researchers with tools to grow customized structures for specific applications,⁵² or to design novel architectures for high-energy-density lithium batteries.⁵³ In addition, liquid-phase microscopy is emerging as an exciting new tool to study protein structures in their native environment.^{54,55}

An alternative trigger for sample dynamics is laser irradiation, which provides a localized stimulus for the experiment. The ability to trigger dynamics only in a circumscribed region is crucial for the study of irreversible processes, that would otherwise require prohibitive amounts of time and sample.⁵⁶

Laser irradiation can also be used to induce a plethora of light-triggered processes, on a broad range of time domains.⁵⁷⁻⁶⁰

The time resolution of in-situ experiments is limited by the frame rate of the camera which, for most commercial CMOS detectors, is on the order of a few milliseconds.⁶¹ The limit is not only set by the camera readout rate, but also by the data transfer speed, as the volume of recorded data becomes significant.⁶²

1.6 Time-resolved electron microscopy

While electron cameras cannot provide high temporal resolution, the ability to visualize fast and ultrafast nanoscale dynamics can shed a light on fundamental phenomena such as protein dynamics,²⁰ light-matter interaction^{63,64} and phase transitions.⁶⁵ It is therefore important to devise new methods that would allow capturing dynamics that occur on the microsecond timescale or faster.

An alternative approach consists in utilizing a pulsed electron source. If images are collected using electron pulses, the temporal resolution is determined by the duration of the pulse rather than the frame rate of the camera, which can boost the temporal resolution by several orders of magnitude.

Several methods to generate short electron pulses have been put forward over the last few decades.

In 1983 Takaoka and Ura proposed a modified design for a field-assisted electron source, with the possibility to pulse the extraction voltage.⁶⁶ In their setup, the authors would lower the extraction fields to a point at which the emission current becomes negligible; they would then rapidly spike the voltage of the extractor anode, generating a short electron pulse.⁶⁶ The method was used to generate pulses as short as 30 μs , which were employed to measure the growth of cracks in polycrystal foils.⁶⁶

The group of Oleg Bostanjoglo proposed a different setup which allows laser irradiation of the electron source, thanks to the insertion of a mirror in the gun assembly.^{67,68} In these experiments the filament of a thermionic emitter is kept at temperatures insufficient to generate appreciable current; nanosecond laser pulses can then be focused on the tip of the filament to either briefly increase its temperature to extreme values,⁶⁷ or to extract electrons exploiting the photoelectric effect.⁶⁸ In both cases, an electron current can be generated for

few tens of nanoseconds or less.^{67,68} While the temporal resolution was markedly improved compared to the approach of Takaoka and Ura, the spatial resolution offered by these nanosecond pulses was around 200 nm, mostly due to the low number of electrons.⁶⁸

Several years later the groups of Geoffrey Campbell and Nigel Browning improved on the approach proposed by Bostanjoglo, obtaining an improvement of the spatial resolution of nanosecond time-resolved experiments of almost two orders of magnitude.⁶⁹ This achievement relied upon a series of technological advancements, including the use of shorter-wavelength UV pulses, which resulted in a 10-fold increase in the quantum efficiency of the photoemission, and modifications of the microscope optics which enabled a more efficient collection of the photoelectrons.⁷⁰ The pulses generated by Browning and colleagues were intense enough to enable single-shot imaging, opening new avenues for the study of irreversible processes.⁷⁰ However, the strong interaction between electrons in such dense pulses causes the beam to spread and lose coherence, significantly compromising the spatial resolution.⁷⁰

If the process under study is completely reversible, however, the single-shot approach is not necessary: the specimen can be excited repeatedly and probed each time with a pulse containing a single electron. After having accumulated several million shots, the superposition of all the pulses forms an image of the unfolding process with high signal. Without charge repulsion, this approach can be used to form atomic-resolution images.⁷¹ By combining this method with ultrafast laser pulses, the group of Ahmed Zewail achieved femtosecond temporal resolution.⁷²

The ability to visualize fast and ultrafast processes has helped elucidate a wide range of fundamental physical phenomena. One of the major milestones in the field was the experimental observation of the absorption of one or more photons by the electron beam,

which is impossible in free space because of their energy-momentum mismatch.⁶³ Short electron pulses were sent through the evanescent field of a metallic nanowire irradiated with femtosecond laser pulses. The confined field provides the complex momentum necessary for the absorption to take place,⁷³ and as a result the electrons gain and lose quanta of photon energy.⁶³ Barwick and colleagues demonstrated this behavior experimentally, by measuring the time-resolved energy spectrum of the interacting electrons. Moreover, the distribution and temporal behavior of the evanescent field could also be measured by forming images with the electrons that gained energy.⁶³

The quantum mechanical details of the interaction between free electrons and photons were elucidated by the group of Claus Ropers, with another ultrafast electron microscopy experiment. During the interaction with the laser pulse, electrons undergo multilevel Rabi oscillations, where each level corresponds to the gain or loss of a quantum of photon energy.⁷⁴ After the interaction, the propagation of the wavepacket follows an intricate scheme, which results in the formation of an attosecond pulse train at a distance from the interaction plane.^{74,75} Such pulses open up new possibilities in the field of quantum optics, and a similar setup for electron pulse compression has been proposed as a way to achieve attosecond time-resolved electron microscopy.⁷⁶

Fast and ultrafast experiments have also enabled the observation of a wide range of nanoscale phenomena, shedding a light on previously inaccessible processes. Time-resolved electron microscopy has been used to monitor the nucleation and propagation of acoustic phonons at defect locations in crystalline materials;⁷⁷ it provides a crucial tool to visualize nanoscale fluid dynamics and the properties that emerge from liquid confinement;⁷⁸ it can also be used to observe phase transitions in materials, revealing the structural pathways and the domain wall dynamics involved in the transformation.^{65,79}

1.7 Spatial resolution of time-resolved experiments

Time-resolved electron microscopy has already generated remarkable discoveries; however, atomic-resolution imaging of fast and ultrafast dynamics has remained elusive. While stroboscopic single-electron experiments can, in principle, achieve atomic resolution, the superposition of individual electrons leads to a blurred image if the specimen drifts over time. In addition, this approach is not suitable to observe irreversible processes.

Several avenues to increase the spatial resolution limit of time-resolved electron microscopy are currently being explored. Long-term drift can be computationally corrected if the recorded frames contain sufficient signal for some key features in the image to be recognized and aligned.⁸⁰⁻⁸³ The minimum dose necessary for drift-correction algorithms depends on the detective quantum efficiency of the electron camera, and the recent development of direct detectors has enabled sub-nm imaging of picosecond dynamics.⁸⁴

Another approach consists in accelerating electrons to energies in the mega- or giga-electron volt range, where relativistic effects strongly reduce the repulsion between electrons.⁸⁵⁻⁸⁷ However, the convoluted setup required and the large energy spread that results from such acceleration make these ultra-relativistic beams difficult to use in practice.⁸⁸

Lastly, novel gun designs for maximized coherence and emission current have been proposed. For example, the group of Peter Kruit simulated the effect of laser irradiation on a Schottky emitter, showing that the combination of photoemission, (laser-assisted) thermal emission and field emission would produce an extremely bright electron beam with limited energy spread.⁸⁹ Unfortunately, the extreme laser intensities required to obtain an appreciable effect are not accessible since they would damage the filament.⁸⁹

1.8 Outline

This thesis describes the development of two methods to image microsecond nanoscale dynamics with near-atomic spatial resolution. The first approach involves the modification of a commercial transmission electron microscope to generate microsecond electron pulses from a Schottky emitter. These pulses are brighter and more intense than the electron beam which can be extracted under typical operating conditions. The performance boost is achieved through laser irradiation of the Schottky filament. As described in Chapter 2, we have inserted a mirror on the focusing electrode of our assembly, which we use to direct short laser pulses onto the filament. As a result, the filament heats up to extreme temperatures, significantly boosting the emission current. The high temperature should completely evaporate the layer of zirconia covering the surface. However, we demonstrate that the short duration of the laser pulse enables the extraction of large currents without damaging the filament. We show through numerical simulations that the laser pulse heats up only the tip of the filament, which allows the layer of zirconia to be readily replenished as the filament cools down.

Microsecond electron pulses are obtained from the boosted electron beam using an electrostatic deflector placed below the electron gun, as detailed in Chapter 3. In this chapter we characterize the brightness and imaging capabilities of the electron pulses. In addition, we show applications of these pulses in dose-fractionated imaging and in time-resolved electron microscopy of irreversible dynamics with atomic resolution.

The second part of the thesis is a characterization of a novel approach to microsecond time-resolved cryo-EM. The high temporal resolution is achieved by locally melting a cryo sample with a laser beam, allowing the embedded particles to undergo structural dynamics in liquid.

As the laser is switched off the irradiated area quickly cools down and revitrifies within a few microseconds, trapping particles in their transient configurations.

Chapter 4 provides important details to validate the suitability of this method to study protein dynamics. We show that it is possible to obtain a near-atomic resolution reconstruction of apoferritin from laser-melted and revitrified sample areas. Within the resolution that we achieve, the reconstruction looks undistinguishable from one obtained from a conventional cryo sample. Additionally, we analyze the change in the distribution of the angular projection orientations after revitrification.

While the melting and revitrification experiments of Chapter 4 were conducted in a modified transmission electron microscope that allows in situ laser irradiation, such a complex experimental setup is not necessary for microsecond time-resolved cryo-EM. In Chapter 5 we show that it is possible to melt and revitrify a cryo sample using an optical microscope coupled with a laser system. Despite the drastic simplification, this setup still allows the user to assess the outcome of the revitrification experiment on the fly. Irradiated grids can then be transferred to a high-resolution electron microscope to image transient states with high spatial and temporal resolution.

The chapter ends with a discussion of the advantages and drawbacks of the optical setup compared to in situ irradiation in an electron microscope.

Finally, the conclusions and outlook of the thesis are laid out in Chapter 6.

1.9 References

1. Fracastoro, Girolamo. Hieronymi Fracastorii homocentrica. Eiusdem de causis criticorum dierum per ea quae in nobis sunt. Zanetti, 1538.
2. Wollman, A. J. M., Nudd, R., Hedlund, E. G. & Leake, M. C. From Animaculum to single molecules: 300 years of the light microscope. *Open Biol.* 5, 150019 (2015).
3. Hooke, R. *Micrographia: Or Some Physiological Descriptions of Minute Bodies Made by Magnifying Glasses, with Observations and Inquiries Thereupon.* (Courier Corporation, 2003).
4. Leeuwenhoek, A. van. *The Select Works of Anthony Van Leeuwenhoek: Containing His Microscopical Discoveries in Many of the Works of Nature.* (London, translated by G. Sidney, 1800).
5. Abbe, E. Beiträge zur Theorie des Mikroskops und der mikroskopischen Wahrnehmung. *Archiv f. mikrosk. Anatomie* 9, 413–468 (1873).
6. Gan, Y. Atomic and subnanometer resolution in ambient conditions by atomic force microscopy. *Surface Science Reports* 64, 99–121 (2009).
7. Bai, C. *Scanning Tunneling Microscopy and Its Application.* (Springer Science & Business Media, 2000).
8. Mikla, V. I. & Mikla, V. V. 1 - Advances in Imaging from the First X-Ray Images. in *Medical Imaging Technology* (eds. Mikla, V. I. & Mikla, V. V.) 1–22 (Elsevier, 2014). doi:10.1016/B978-0-12-417021-6.00001-0.
9. Ilari, A. & Savino, C. Protein Structure Determination by X-Ray Crystallography. in *Bioinformatics: Data, Sequence Analysis and Evolution* (ed. Keith, J. M.) 63–87 (Humana Press, 2008). doi:10.1007/978-1-60327-159-2_3.

10. Feynman, R. P. QED: The Strange Theory of Light and Matter. (Princeton University Press, 2006).
11. Tiemeijer, P. C., Bischoff, M., Freitag, B. & Kisielowski, C. Using a monochromator to improve the resolution in TEM to below 0.5Å. Part I: Creating highly coherent monochromated illumination. *Ultramicroscopy* 114, 72–81 (2012).
12. Tiemeijer, P. C., Bischoff, M., Freitag, B. & Kisielowski, C. Using a monochromator to improve the resolution in TEM to below 0.5Å. Part II: Application to focal series reconstruction. *Ultramicroscopy* 118, 35–43 (2012).
13. Dubochet, J. & McDowell, A. w. Vitrification of Pure Water for Electron Microscopy. *Journal of Microscopy* 124, 3–4 (1981).
14. Dubochet, J. Cryo-electron microscopy of vitrified specimens. *Quarterly Reviews of Biophysics* 21, 129–228 (1988).
15. Henderson, R. The potential and limitations of neutrons, electrons and X-rays for atomic resolution microscopy of unstained biological molecules. *Quarterly Reviews of Biophysics* 28, 171–193 (1995).
16. Frank, J. Chapter 5 - Three-Dimensional Reconstruction. in *Three-Dimensional Electron Microscopy of Macromolecular Assemblies* (ed. Frank, J.) 182–246 (Academic Press, 1996). doi:10.1016/B978-012265040-6/50005-9.
17. Kühlbrandt, W. The Resolution Revolution. *Science* 343, 1443–1444 (2014).
18. Ke, Z. et al. Structures and distributions of SARS-CoV-2 spike proteins on intact virions. *Nature* 588, 498–502 (2020).
19. Wrapp, D. et al. Cryo-EM structure of the 2019-nCoV spike in the prefusion conformation. *Science* 367, 1260–1263 (2020).

20. Henzler-Wildman, K. & Kern, D. Dynamic personalities of proteins. *Nature* 450, 964–972 (2007).
21. Seitz, E. Analysis of Conformational Continuum and Free-energy Landscapes from Manifold Embedding. (Columbia University, 2022).
22. Frank, J. Three-Dimensional Electron Microscopy of Macromolecular Assemblies: Visualization of Biological Molecules in Their Native State. (Google eBook) (2006).
23. Giraldo-Barreto, J. et al. A Bayesian approach to extracting free-energy profiles from cryo-electron microscopy experiments. *Sci Rep* 11, 13657 (2021).
24. Zhong, E. D., Bepler, T., Berger, B. & Davis, J. H. CryoDRGN: reconstruction of heterogeneous cryo-EM structures using neural networks. *Nat Methods* 18, 176–185 (2021).
25. Levy, A., Wetzstein, G., Martel, J., Poitevin, F. & Zhong, E. D. Amortized Inference for Heterogeneous Reconstruction in Cryo-EM. Preprint at <https://doi.org/10.48550/arXiv.2210.07387> (2022).
26. Frank, J. Time-resolved cryo-electron microscopy: Recent progress. *Journal of Structural Biology* 200, 303–306 (2017).
27. Shaikh, T. R. et al. Initial bridges between two ribosomal subunits are formed within 9.4 milliseconds, as studied by time-resolved cryo-EM. *Proceedings of the National Academy of Sciences* 111, 9822–9827 (2014).
28. Shaikh, T. R., Barnard, D., Meng, X. & Wagenknecht, T. Implementation of a flash-photolysis system for time-resolved cryo-electron microscopy. *Journal of Structural Biology* 165, 184–189 (2009).
29. Berriman, J. & Unwin, N. Analysis of transient structures by cryo-microscopy combined with rapid mixing of spray droplets. *Ultramicroscopy* 56, 241–252 (1994).

30. Kontziampasis, D. et al. A cryo-EM grid preparation device for time-resolved structural studies. *IUCrJ* 6, 1024–1031 (2019).
31. Dandey, V. P. et al. Time-resolved cryoEM using Spotiton. *Nat Methods* 17, 897–900 (2020).
32. Ravelli, R. B. G. et al. Cryo-EM structures from sub-nl volumes using pin-printing and jet vitrification. *Nat Commun* 11, 2563 (2020).
33. Panciera, F. et al. Phase Selection in Self-catalyzed GaAs Nanowires. *Nano Lett.* 20, 1669–1675 (2020).
34. Nakayama, H., Nagata, M., Abe, H. & Shimizu, Y. In Situ TEM Study of Rh Particle Sintering for Three-Way Catalysts in High Temperatures. *Catalysts* 11, 19 (2021).
35. Legros, M., Cabié, M. & Gianola, D. S. In situ deformation of thin films on substrates. *Microscopy Research and Technique* 72, 270–283 (2009).
36. Lepinoux, J. & Kubin, L. P. In situ TEM observations of the cyclic dislocation behaviour in persistent slip bands of copper single crystals. *Philosophical Magazine A* 51, 675–696 (1985).
37. Castany, P. & Legros, M. Preparation of H-bar cross-sectional specimen for in situ TEM straining experiments: A FIB-based method applied to a nitrided Ti–6Al–4V alloy. *Materials Science and Engineering: A* 528, 1367–1371 (2011).
38. Hsueh, Y.-H., Ranjan, A., Lyu, L.-M., Hsiao, K.-Y. & Lu, M.-Y. In situ TEM observations of void movement in Ag nanowires affecting the electrical properties under biasing. *Chem. Commun.* 57, 11221–11224 (2021).
39. Yang, L. et al. Direct View on the Origin of High Li⁺ Transfer Impedance in All-Solid-State Battery. *Advanced Functional Materials* 31, 2103971 (2021).
40. Ross, F. M. *Liquid Cell Electron Microscopy*. (Cambridge University Press, 2016).

41. Yuk, J. M. et al. High-Resolution EM of Colloidal Nanocrystal Growth Using Graphene Liquid Cells. *Science* 336, 61–64 (2012).
42. Mølhave, K., Madsen, D. N., Dohn, S. & Bøggild, P. Constructing, connecting and soldering nanostructures by environmental electron beam deposition. *Nanotechnology* 15, 1047–1053 (2004).
43. Takeda, S. & Yoshida, H. Atomic-resolution environmental TEM for quantitative in-situ microscopy in materials science. *Microscopy* 62, 193–203 (2013).
44. Ye, F. et al. In Situ TEM Studies of Catalysts Using Windowed Gas Cells. *Catalysts* 10, 779 (2020).
45. Zheng, H. et al. Observation of Single Colloidal Platinum Nanocrystal Growth Trajectories. *Science* 324, 1309–1312 (2009).
46. Woehl, T. J., Evans, J. E., Arslan, I., Ristenpart, W. D. & Browning, N. D. Direct in Situ Determination of the Mechanisms Controlling Nanoparticle Nucleation and Growth. *ACS Nano* 6, 8599–8610 (2012).
47. Woehl, T. J. Metal Nanocrystal Formation during Liquid Phase Transmission Electron Microscopy: Thermodynamics and Kinetics of Precursor Conversion, Nucleation, and Growth. *Chemistry of Materials* 32, 7569–7581 (2020).
48. Wen, C.-Y. et al. Periodically Changing Morphology of the Growth Interface in Si, Ge, and GaP Nanowires. *Phys. Rev. Lett.* 107, 025503 (2011).
49. Jacobsson, D. et al. Interface dynamics and crystal phase switching in GaAs nanowires. *Nature* 531, 317–322 (2016).
50. Bealing, C. R., Baumgardner, W. J., Choi, J. J., Hanrath, T. & Hennig, R. G. Predicting Nanocrystal Shape through Consideration of Surface-Ligand Interactions. *ACS Nano* 6, 2118–2127 (2012).

51. Xia, Y., Xiong, Y., Lim, B. & Skrabalak, S. E. Shape-Controlled Synthesis of Metal Nanocrystals: Simple Chemistry Meets Complex Physics? *Angewandte Chemie International Edition* 48, 60–103 (2009).
52. Panciera, F. et al. Controlling nanowire growth through electric field-induced deformation of the catalyst droplet. *Nat Commun* 7, 12271 (2016).
53. Liu, Y. et al. Making Li-metal electrodes rechargeable by controlling the dendrite growth direction. *Nat Energy* 2, 1–10 (2017).
54. Keskin, S. & de Jonge, N. Reduced Radiation Damage in Transmission Electron Microscopy of Proteins in Graphene Liquid Cells. *Nano Lett.* 18, 7435–7440 (2018).
55. Wang, C., Qiao, Q., Shokuhfar, T. & Klie, R. F. High-Resolution Electron Microscopy and Spectroscopy of Ferritin in Biocompatible Graphene Liquid Cells and Graphene Sandwiches. *Advanced Materials* 26, 3410–3414 (2014).
56. Taheri, M. L. et al. Laser-based in situ techniques: novel methods for generating extreme conditions in TEM samples. *Microsc Res Tech* 72, 122–130 (2009).
57. Olshin, P. K., Bongiovanni, G., Drabbels, M. & Lorenz, U. J. Atomic-Resolution Imaging of Fast Nanoscale Dynamics with Bright Microsecond Electron Pulses. *Nano Lett.* 21, 612–618 (2021).
58. Kim, J. S. et al. Imaging of Transient Structures Using Nanosecond in Situ TEM. *Science* 321, 1472–1475 (2008).
59. Voss, J. M., Olshin, P. K., Charbonnier, R., Drabbels, M. & Lorenz, U. J. In Situ Observation of Coulomb Fission of Individual Plasmonic Nanoparticles. *ACS Nano* 13, 12445–12451 (2019).
60. Bongiovanni, G. et al. The fragmentation mechanism of gold nanoparticles in water under femtosecond laser irradiation. *Nanoscale Adv.* 3, 5277–5283 (2021).

61. McMullan, G., Faruqi, A. R., Clare, D. & Henderson, R. Comparison of optimal performance at 300keV of three direct electron detectors for use in low dose electron microscopy. *Ultramicroscopy* 147, 156–163 (2014).
62. Stevens, A. et al. Applying compressive sensing to TEM video: a substantial frame rate increase on any camera. *Adv Struct Chem Imag* 1, 10 (2015).
63. Barwick, B., Flannigan, D. J. & Zewail, A. H. Photon-induced near-field electron microscopy. *Nature* 462, 902–906 (2009).
64. Wang, K. et al. Coherent interaction between free electrons and a photonic cavity. *Nature* 582, 50–54 (2020).
65. Danz, T., Domröse, T. & Ropers, C. Ultrafast nanoimaging of the order parameter in a structural phase transition. *Science* 371, 371–374 (2021).
66. Takaoka, A. & Ura, K. Stroboscopic TEM with Time Resolution of 30 μ s. *Journal of Electron Microscopy* 32, 299–304 (1983).
67. Bostanjoglo, O. & Heinrich, F. Producing high-current nanosecond electron pulses with a standard tungsten hairpin gun. *J. Phys. E: Sci. Instrum.* 20, 1491–1493 (1987).
68. Dömer, H. & Bostanjoglo, O. High-speed transmission electron microscope. *Review of Scientific Instruments* 74, 4369–4372 (2003).
69. LaGrange, T. et al. Nanosecond time-resolved investigations using the in situ of dynamic transmission electron microscope (DTEM). *Ultramicroscopy* 108, 1441–1449 (2008).
70. LaGrange, T. et al. Approaches for ultrafast imaging of transient materials processes in the transmission electron microscope. *Micron* 43, 1108–1120 (2012).
71. Park, H. S., Baskin, J. S., Kwon, O.-H. & Zewail, A. H. Atomic-Scale Imaging in Real and Energy Space Developed in Ultrafast Electron Microscopy. *Nano Lett.* 7, 2545–2551 (2007).

72. Gahlmann, A., Park, S. T. & Zewail, A. H. Ultrashort electron pulses for diffraction, crystallography and microscopy: theoretical and experimental resolutions. *Phys. Chem. Chem. Phys.* 10, 2894–2909 (2008).
73. Abajo, F. J. G. de & Kociak, M. Electron energy-gain spectroscopy. *New J. Phys.* 10, 073035 (2008).
74. Feist, A. et al. Quantum coherent optical phase modulation in an ultrafast transmission electron microscope. *Nature* 521, 200–203 (2015).
75. Priebe, K. E. et al. Attosecond electron pulse trains and quantum state reconstruction in ultrafast transmission electron microscopy. *Nature Photon* 11, 793–797 (2017).
76. Ryabov, A., Thurner, J. W., Nabben, D., Tsarev, M. V. & Baum, P. Attosecond metrology in a continuous-beam transmission electron microscope. *Science Advances* 6, eabb1393 (2020).
77. Cremons, D. R., Plemmons, D. A. & Flannigan, D. J. Femtosecond electron imaging of defect-modulated phonon dynamics. *Nature Communications* 7, (2016).
78. Lorenz, U. J. & Zewail, A. H. Observing liquid flow in nanotubes by 4D electron microscopy. *Science* 344, 1496–1500 (2014).
79. Baum, P., Yang, D.-S. & Zewail, A. H. 4D Visualization of Transitional Structures in Phase Transformations by Electron Diffraction. *Science* 318, 788–792 (2007).
80. Reddy, B. S. & Chatterji, B. N. An FFT-based technique for translation, rotation, and scale-invariant image registration. *IEEE Trans. on Image Process.* 5, 1266–1271 (1996).
81. Punjani, A., Rubinstein, J. L., Fleet, D. J. & Brubaker, M. A. cryoSPARC: algorithms for rapid unsupervised cryo-EM structure determination. *Nat Methods* 14, 290–296 (2017).
82. Kaspi, O., Yosipof, A. & Senderowitz, H. RANdom SAmple Consensus (RANSAC) algorithm for material-informatics: application to photovoltaic solar cells. *J Cheminform* 9, 34 (2017).

83. Dou, J., Qin, Q. & Tu, Z. Robust image matching based on the information of SIFT. *Optik* 171, 850–861 (2018).
84. Kim, Y.-J., Jung, H., Han, S. W. & Kwon, O.-H. Ultrafast Electron Microscopy Visualizes Acoustic Vibrations of Plasmonic Nanorods at the Interfaces. *Matter* 1, 481–495 (2019).
85. Musumeci, P. et al. Novel Radio-Frequency Gun Structures for Ultrafast Relativistic Electron Diffraction. *Microscopy and Microanalysis* 15, 290–297 (2009).
86. Rimjaem, S., Farias, R., Thongbai, C., Vilaithong, T. & Wiedemann, H. Femtosecond electron bunches from an RF-gun. *Nuclear Instruments and Methods in Physics Research Section A: Accelerators, Spectrometers, Detectors and Associated Equipment* 533, 258–269 (2004).
87. Weathersby, S. P. et al. Mega-electron-volt ultrafast electron diffraction at SLAC National Accelerator Laboratory. *Review of Scientific Instruments* 86, 073702 (2015).
88. Zhang, L., Hoogenboom, J. P., Cook, B. & Kruit, P. Photoemission sources and beam blankers for ultrafast electron microscopy. *Structural Dynamics* 6, 051501 (2019).
89. Cook, B., Bronsgeest, M., Hagen, K. & Kruit, P. Improving the energy spread and brightness of thermal-field (Schottky) emitters with PHAST—PHoto Assisted Schottky Tip. *Ultramicroscopy* 109, 403–412 (2009).

Chapter 2 - Intense Microsecond Electron Pulses from a Schottky Emitter*

2.1 Introduction

Field emitters have greatly advanced a range of applications in electron microscopy that particularly benefit from their high brightness and coherence.¹⁻⁶ More recently, they have also found application in the rapidly developing field of time-resolved electron microscopy,⁷⁻¹² enabling for example the coherent manipulation of single-electron wavepackets with laser fields¹³ or time-resolved holography.^{9,12} While field emitters made from carbon nanotubes,¹⁴ LaB₆ nanowires,¹⁵ or single atoms¹⁶ have set brightness records, tungsten field emitters are most widely used, as they offer stable operation over extended periods of time, as well as a lifetime of years.^{17,18} Schottky emitters consist of a single-crystalline tungsten to which a high extraction field is applied. They are coated with a layer of zirconium oxide to reduce the work function of the (100) emitting surface,³ and are typically operated at temperatures up to 1800 K. This also reduces the buildup of contaminations and allows the zirconia layer on the emitting surface to continuously be replenished through diffusion from a reservoir on the body of the emitter.¹⁹

For many experiments with high time-resolution, in particular for imaging with short electron pulses, the available probe current is a critical figure of merit that limits the amount of information that can be obtained in a short amount of time.^{20,21} Given the excellent source properties of Schottky emitters, it is therefore tempting to try and extract larger currents.

*Reproduced from G. Bongiovanni, P.K. Olshin, M. Drabbels and U.J. Lorenz, *Appl. Phys. Lett.* 116, 234103 (2020), with the permission of AIP Publishing.

Authors Contributions: G.B and P.K.O. performed the experiments; G.B. analysed the data; M.D. and U.J.L. supervised the project; U.J.L. wrote the manuscript with the contribution from all authors.

However, practical considerations limit the ability to do so by simply raising the extraction voltage or the operating temperature. At high extraction fields, tungsten atoms migrate towards the tip, which leads to unstable emission and causes the end facet to grow, ultimately shortening the lifetime of the emitter.^{22,3,17,18} The tip geometry is only stable over extended periods of time if the pull of the extraction field is exactly counterbalanced by the surface tension of the tip, which drives atoms to migrate in the opposite direction.^{22,3,17,18} For a typical gun geometry, the stable extraction voltage is about 3-4 kV.²² It is also impractical to raise the temperature of the emitter significantly above 1800 K, where evaporation rapidly depletes the zirconium oxide reservoir and thus shortens the lifetime of the emitter.³ Above 1950 K, the emission current begins to drop, as the zirconia coverage of the emitting surface decreases,²² and at 2400 K, the zirconium oxide layer evaporates entirely, making operation impossible.²³ It has been reported that under extreme conditions, at 1950 K and with about twice the stable extraction voltage, a stable emission current of 500 μA can be sustained for several days.^{22,24} However, under practical operating conditions, the emission current is typically about 100 μA .²²

Here, we demonstrate that it is possible to boost emission from a Schottky emitter by temporarily operating it at extreme temperatures. When we heat the emitter tip with a microsecond laser pulse to an estimated temperature of over 2500 K, the emission current increases to nearly 450 μA . We envision that in combination with a beam blanker, this will enable the generation of intense microsecond electron pulses of high brightness. While femtosecond and nanosecond photoelectron pulses from field emitters have previously been demonstrated,^{8,9,25-28} photoemission does not provide a convenient mechanism to access the microsecond timescale. Because of the low photoelectron yields involved, the laser powers required to sustain a large photoemission current would rapidly heat the emitter to

temperatures at which thermal emission vastly exceeds photoemission.²⁹ Our experiments demonstrate the generation of intense microsecond electron pulses from a field emitter, which will particularly benefit atomic-resolution imaging of fast processes occurring on the microsecond timescale.

2.2 Results and discussion

Experiments were carried out with a modified JEOL Schottky field emission gun, whose emitter assembly is illustrated in Fig. 1a. The emitter (430 nm tip radius) protrudes from a hole in the suppressor, which is held at -300 V with respect to the emitter. The extractor is located at a distance of 350 μm from the tip and biased to +3.0 kV. The assembly is completed by the so-called anode 2, which serves as an electrostatic lens (typically +7.8 kV). Unless otherwise noted, the emitter temperature is set to 1720 K, the operating temperature recommended by the manufacturer of the gun, at which we obtain an emission current of 120 μA . In order to transiently boost emission, we heat the emitter tip with a high-power continuous laser (532 nm wavelength), as illustrated in Fig. 1b. The laser beam is chopped into microsecond pulses with an acousto-optic modulator, expanded, and focused onto the tip of the emitter (17 μm FWHM laser spot size), which it strikes under an angle of 16° with respect to the electron optical axis. A piezo-controlled mirror facilitates alignment. The reported laser powers refer to the power that reaches the emitter, where we have accounted for losses on optics. For the experiments reported in Fig. 2, the electron gun was mounted on a JEOL 2010F transmission electron microscope and operated at 200 kV accelerating voltage. The probe current was measured on the phosphor screen of the microscope, with a fast transimpedance amplifier connected to record the temporal structure of the electron pulses. For the experiments in Fig. 4, the emitter

assembly was removed from the gun and mounted in a dedicated vacuum chamber. The electron beam was monitored on a phosphor screen at a distance of 25 cm from the emitter.

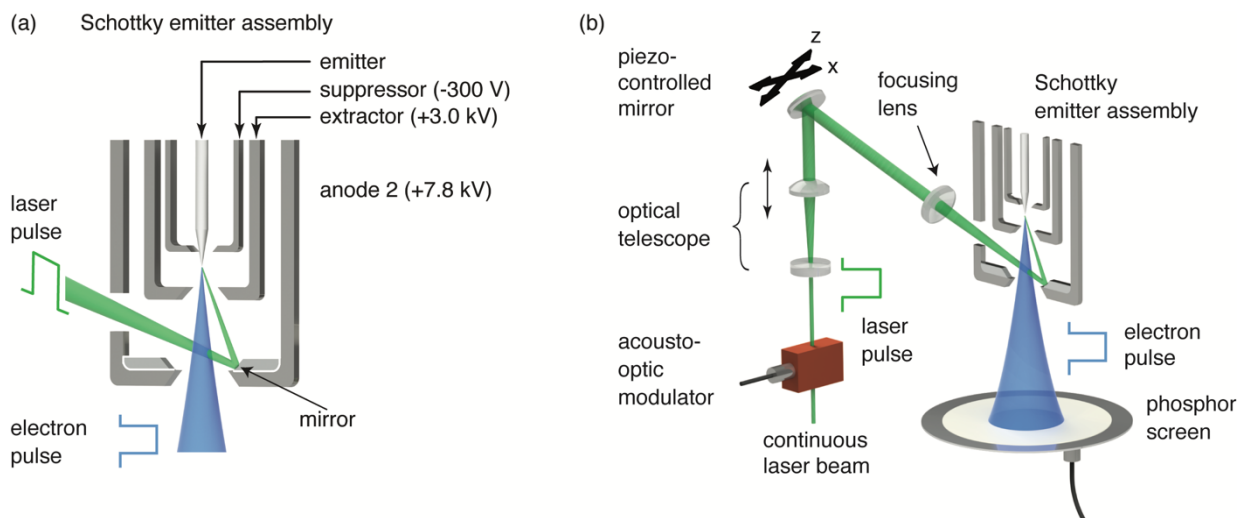


Figure 1. Illustration of the experimental setup. (a) Geometry of the emitter assembly. Operating voltages are indicated relative to the emitter. (b) The emission current is boosted by heating the tip of the emitter with microsecond laser pulses.

Figure 2a demonstrates that laser heating the tip of the emitter can be used to significantly boost electron emission for a duration of hundreds of microseconds. Under irradiation with a $100 \mu\text{s}$ laser pulse (red curve, 1 kHz repetition rate), the probe current (blue) increases rapidly, by more than three times at the end of the laser pulse, before it slowly returns to its initial value. We obtain a rise time of the electron pulse of $11 \mu\text{s}$ from a fit with the sum of an exponential and a linear function, which appears to give a good description for a range of pulse lengths. The tail of the pulse follows a biexponential decay with timescales of $14 \mu\text{s}$

and 85 μs (75 % and 25 % weight). For simplicity, we report 80 % to 20 % fall times in the following, for which we measure 36 μs here.

Figure 2b shows that the peak probe current increases linearly with laser power (100 μs pulses, 20 Hz), reaching 210 nA at 0.64 W, which corresponds to an enhancement of 3.7 times and an emission current of nearly 450 μA . The linear increase of the probe current is consistent with the high-temperature behavior of Schottky emitters. While below 1600 K, the emission current follows Schottky theory and grows exponentially with temperature,¹ between 1600 K and 1850 K, it only increases linearly,³ which is due to a linear increase of the work function in this temperature range.²³ For our emitter, the probe current increases by 20 nA per 100 K, which allows us to estimate the peak temperature of the tip. (Fig. 2b, top axis). For the highest laser power, the tip reaches over 2500 K, vastly exceeding the recommended maximum operating temperature (1850 K), and well above the temperature at which zirconium oxide is completely removed from a tungsten surface (2400 K).²³ While continuous operation at such an extreme temperature would be all but impossible, we are evidently able to outrun the evaporation of zirconia from the end facet. This process likely requires tens of seconds, the time it takes the emission current to stabilize after a sudden temperature change.³ We note that for high current densities, Coulomb interactions ultimately limit the brightness^{24,30}. We therefore expect the increase in brightness to be lower than the increase in current.

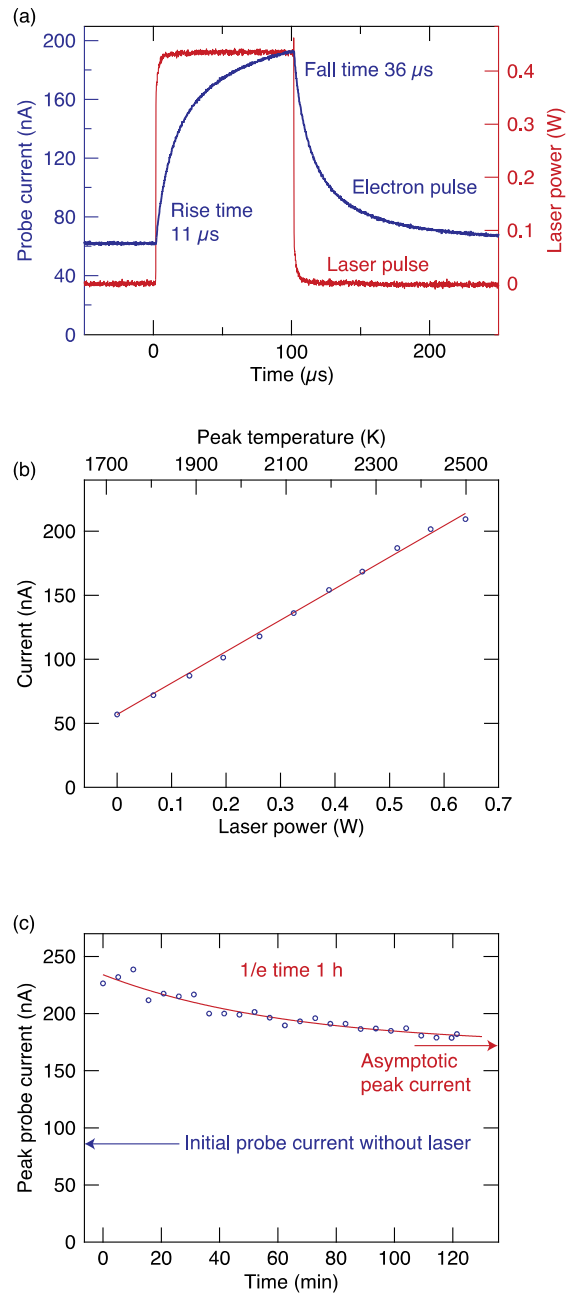


Figure 2. Generation of intense electron pulses. (a) Temporal evolution of the electron probe current (blue) when the emitter tip is illuminated with 100 μs laser pulses (red). (b) Peak probe current as a function of laser power. (c) Measurement of the long-term stability of the peak probe current at high repetition rate (0.39 W, 100 μs pulses, 1 kHz).

If the emitter is continuously exposed to intense laser pulses, the peak probe current slowly decreases over time, as shown in Fig. 2c. Under irradiation with 100 μs pulses of 0.44 W at 1 kHz repetition rate, the enhancement of the peak probe current is initially three, but then slowly drops to two, with a time constant of one hour. Apparently, under these conditions, the rate at which the laser pulses remove zirconium oxide from the end facet exceeds the rate at which it can be replenished through diffusion. The zirconium oxide coverage therefore decreases, and with it the peak current, until an equilibrium is established in which both rates are equal. We note that after we stop irradiating it, the emitter slowly recovers, and the peak probe current returns to its initial value. Moreover, we do not observe any significant changes in the emission characteristics over time, suggesting that the tip shape remains stable, as is expected when the emitter is operated with a stable extraction voltage. At higher repetition rates, the enhancement of the peak probe current is initially the same, with the drop occurring faster accordingly.

Finite element simulations (Comsol Multiphysics) provide additional insights into the heating and cooling dynamics of the emitter. As illustrated in Fig. 3a, we model an emitter of typical dimensions with the thermal properties of tungsten³¹ and an initial temperature of 1720 K. A tip of 500 nm radius tops a 1.4 μm long cylindrical shaft, which widens in a 300 μm long conical section to the diameter of the body of the emitter (125 μm). The emitter is heated by a Gaussian laser beam (17 μm FWHM) that is centered onto the base of the shaft and strikes it under an angle of 16° with respect to the electron optical axis (inset). We neglect the variation of the absorbance with local incidence angle and instead assume an average absorbance of 21 %.³²

Figure 3b shows the temperature evolution of the emitting surface under irradiation with a 0.8 W laser pulse of 100 μs duration. We obtain heating and cooling times of 7 μs and 33 μs , respectively, in reasonable agreement with the experiment. The temperature jump is somewhat lower, most likely reflecting differences between the simulated and actual emitter geometry. The surface temperature distribution at the end of the laser pulse (Fig. 3a, color) reveals that only the very tip of the emitter is being heated up significantly, while the temperature of the emitter body remains unchanged. At a distance of only 30 μm from the tip, the laser induced temperature jump decreases by half. Such very localized heating is favorable for the purpose of creating intense electron pulses, since loss of zirconium oxide that inevitably occurs at extreme temperatures is mostly limited to the tip. Diffusion from adjacent areas can therefore rapidly replenish the zirconium oxide layer on the end facet. In contrast, heating the entire emitter to extreme temperatures would remove zirconium oxide from its whole surface, thus making operation impossible.

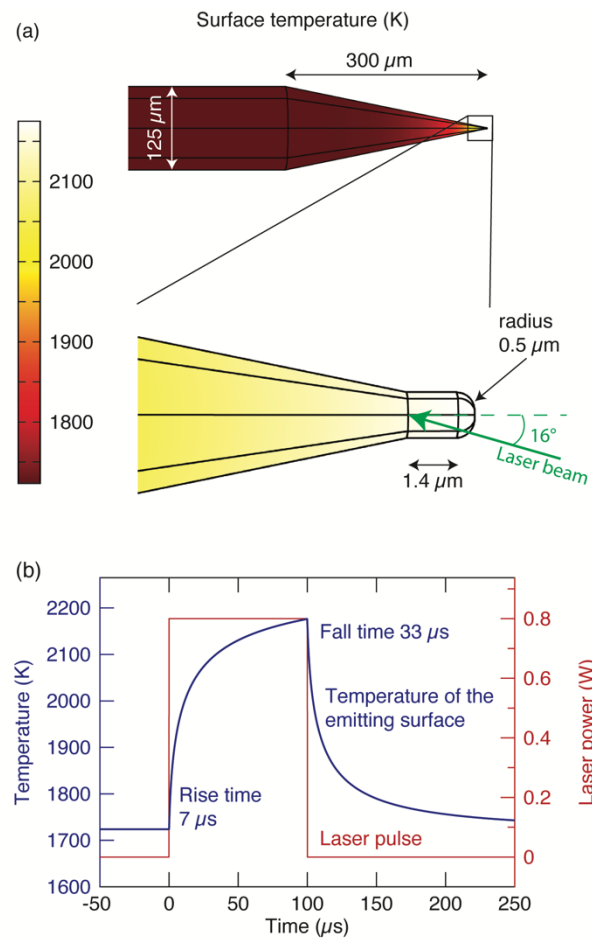


Figure 3. Simulation of the temperature evolution of the emitter under laser illumination. (a) Surface temperature of the emitter after illumination with a $100 \mu\text{s}$ laser pulse. The laser beam ($17 \mu\text{m}$ FWHM) is indicated with a green arrow. (b) Temperature evolution of the emitting surface (blue) during illumination with a $100 \mu\text{s}$ laser pulse (red).

The electron yield and pulse shape are sensitive to the alignment of the laser. This is evident in Fig. 4a, which displays the number of electrons emitted per pulse as the laser beam is being rastered over the emitter by means of the piezo-controlled mirror (see Fig. 1b; $100 \mu\text{s}$ laser pulses at 0.2 W , with the emitter temperature lowered to 1400 K , so that no emission occurs without laser). For reference, the orientation of the emitter is indicated above the plot, together

with the directions in which the laser beam is scanned. The electron yield roughly maps out the profile of the emitter, with the conical body faintly visible on the left, and the tip marked by an intense maximum in the center. This maximum appears elongated, with a FWHM of $218\ \mu\text{m}$ along the emitter axis, and $17\ \mu\text{m}$ orthogonal to it. Since the tip of the emitter is small ($430\ \text{nm}$ radius), we infer that the laser beam diameter at the emitter is about $17\ \mu\text{m}$ FWHM. As the laser is scanned towards the emitter body, it has to heat up a larger volume, which results in a lower temperature of the end facet and thus a lower emission current. For the same reason, we also observe slower rise and fall times with the laser aligned to the conical part of the emitter. We conclude that a fast response of the emitter as well as large peak currents are obtained with the laser focus centered near the tip. Under such conditions, the laser spot size can be easily minimized by monitoring the emission current. When we change the length of the beam expanding telescope (see Fig. 1b), the peak current goes through a maximum (Fig. 4b), which indicates optimum focusing conditions. Focusing the laser as tightly as possible is desirable in order to obtain the most localized heating and thus the fastest thermal response of the emitter.

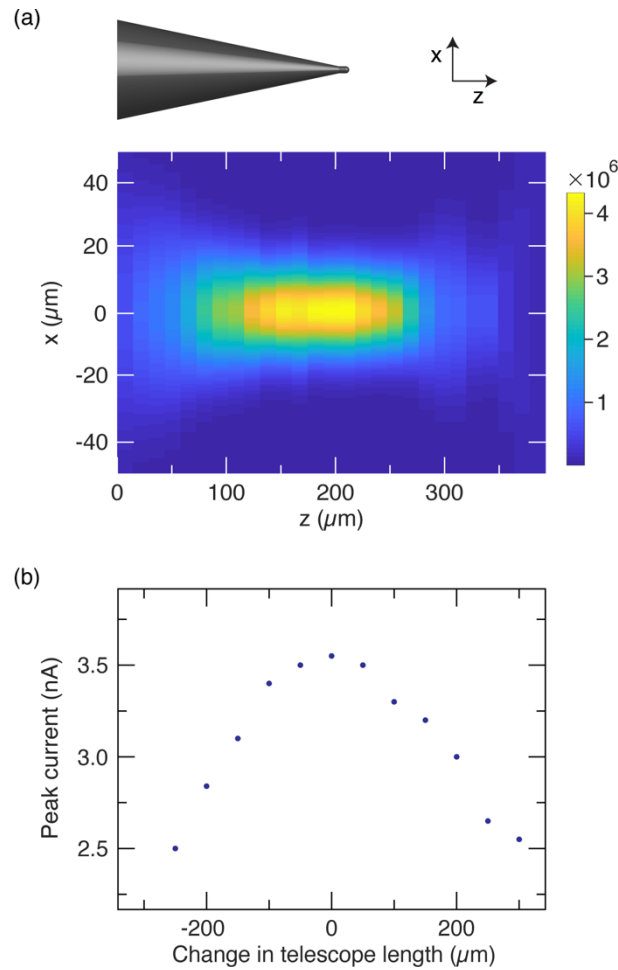


Figure 4. Electron yield as a function of the laser focus position and beam diameter. (a) Number of electrons as a function of the laser focus position. The orientation of the emitter is illustrated above the plot. (b) Peak probe current as a function of the length of the beam expanding telescope (see Fig. 1b).

2.3 Conclusion

In the future, we envision adding a beam blocker²¹ to our microscope in order to chop the laser boosted electron beam into pulses of desired duration. The generation of intense microsecond electron pulses from a field emitter promises to enable atomic-resolution single-

shot^{33,34} as well as stroboscopic imaging of fast processes occurring on the microsecond timescale. A particular appeal of such an approach lies in the fact that it would allow one to align and operate the microscope under standard conditions and then switch on the fly to pulsed operation with a laser boosted electron beam. The laser power should be chosen based on the desired application. For single-shot imaging or stroboscopic imaging with a limited number of electron pulses, it is desirable to extract the largest number of electrons and therefore use the highest laser power. Pulsed operation over extended periods of time may require reducing the laser power in order to limit the removal of zirconia from the end facet. Finally, we note that emission currents can also be further increased by raising the extraction voltage, which, however, will reduce the lifetime of the emitter.

2.4 References

1. L. Swanson and G. Schwind, Handbook of Charged Particles Optics, 2nd ed. (CRC Press, 2008), pp. 1–28
2. Swanson, L. W. & Schwind, G. A. A Review of the Cold-Field Electron Cathode. *Advances in Imaging and Electron Physics* S 159, 63–100 (2009).
3. Bronsgeest, M. S. *Physics of Schottky Electron Sources*. (Technical University of Delft, 2009).
4. Otten, M. T. & Coene, W. M. J. High-resolution imaging on a field emission TEM. *Ultramicroscopy* 48, 77–91 (1993).

5. Bogner, A., Jouneau, P.-H., Thollet, G., Basset, D. & Gauthier, C. A history of scanning electron microscopy developments: Towards "wet-STEM" imaging. *Micron* 38, 390–401 (2007).
6. Lichte, H. & Lehmann, M. Electron holography - basics and applications. *Rep Prog Phys* 71, (2008).
7. Mohammed, O. F., Yang, D.-S., Pal, S. K. & Zewail, A. H. 4D Scanning Ultrafast Electron Microscopy: Visualization of Materials Surface Dynamics. *J. Am. Chem. Soc.* 133, 7708--7711 (2011).
8. Feist, A. et al. Ultrafast transmission electron microscopy using a laser-driven field emitter: Femtosecond resolution with a high coherence electron beam. *Ultramicroscopy* 176, 63–73 (2017).
9. Houdellier, F., Caruso, G. M., Weber, S., Kociak, M. & Arbouet, A. Development of a high brightness ultrafast Transmission Electron Microscope based on a laser-driven cold field emission source. *Ultramicroscopy* 186, 128–138 (2018).
10. Das, P. et al. Stimulated electron energy loss and gain in an electron microscope without a pulsed electron gun. *Ultramicroscopy* 203, 44–51 (2019).
11. Zhu, C. et al. Development of analytical ultrafast transmission electron microscopy based on laser-driven Schottky field emission. *Ultramicroscopy* 209, 112887 (2020).
12. Niermann, T., Lehmann, M. & Wagner, T. Gated interference for time-resolved electron holography. *Ultramicroscopy* 182, 54–61 (2017).
13. Feist, A. et al. Quantum coherent optical phase modulation in an ultrafast transmission electron microscope. *Nature* 521, 200–203 (2015).
14. Houdellier, F. et al. Development of TEM and SEM high brightness electron guns using cold-field emission from a carbon nanotip. *Ultramicroscopy* 151, 107–115 (2015).

15. Zhang, H. et al. An ultrabright and monochromatic electron point source made of a LaB₆ nanowire. *Nature Nanotech* 11, 273–279 (2016).
16. Ishikawa, T. et al. Highly efficient electron gun with a single-atom electron source. *Appl. Phys. Lett.* 90, 143120 (2007).
17. Liu, K., Schwind, G. A., Swanson, L. W. & Campbell, J. A. Field induced shape and work function modification for the ZrO/W(100) Schottky cathode. *Journal of Vacuum Science & Technology B, Nanotechnology and Microelectronics: Materials, Processing, Measurement, and Phenomena* 28, C6C26-C6C33 (2010).
18. Bahm, A., Schwind, G. & Swanson, L. The ZrO/W(100) Schottky cathode: Morphological modification and its effect on long term operation. *Journal of Applied Physics* 110, 054322 (2011).
19. Tiemeijer, P. C., Bischoff, M., Freitag, B. & Kisielowski, C. Using a monochromator to improve the resolution in TEM to below 0.5Å. Part I: Creating highly coherent monochromated illumination. *Ultramicroscopy* 114, 72–81 (2012).
20. Armstrong, M. R. et al. Practical considerations for high spatial and temporal resolution dynamic transmission electron microscopy. *Ultramicroscopy* 107, 356–367 (2007).
21. Zhang, L., Hoogenboom, J. P., Cook, B. & Kruit, P. Photoemission sources and beam blankers for ultrafast electron microscopy. *Structural Dynamics* 6, 051501 (2019).
22. van Veen, A. H. V., Hagen, C. W., Barth, J. E. & Kruit, P. Reduced brightness of the ZrO/W Schottky electron emitter. *Journal of Vacuum Science & Technology B: Microelectronics and Nanometer Structures Processing, Measurement, and Phenomena* 19, 2038–2044 (2001).
23. Danielson, L. R. The Zr-O-W(100) emitter and coadsorption of zirconium and carbon monoxide on W(100). *Journal of Applied Physics* 52, 6769–6776 (1981).

24. Cook, B., Verduin, T., Hagen, C. W. & Kruit, P. Brightness limitations of cold field emitters caused by Coulomb interactions. *J Vac Sci Technol B* 28, C6c74-C6c79 (2010).
25. Hommelhoff, P., Kealhofer, C. & Kasevich, M. A. Ultrafast electron pulses from a tungsten tip triggered by low-power femtosecond laser pulses. *Phys Rev Lett* 97, (2006).
26. Ehberger, D. et al. Highly Coherent Electron Beam from a Laser-Triggered Tungsten Needle Tip. *Phys Rev Lett* 114, (2015).
27. Hoffrogge, J. et al. Tip-based source of femtosecond electron pulses at 30 keV. *J Appl Phys* 115, (2014).
28. Bormann, R., Strauch, S., Schäfer, S. & Ropers, C. An ultrafast electron microscope gun driven by two-photon photoemission from a nanotip cathode. *Journal of Applied Physics* 118, 173105 (2015).
29. Cook, B., Bronsgeest, M., Hagen, K. & Kruit, P. Improving the energy spread and brightness of thermal-field (Schottky) emitters with PHAST-PHoto Assisted Schottky Tip. *Ultramicroscopy* 109, 403–412 (2009).
30. Bach, N. et al. Coulomb interactions in high-coherence femtosecond electron pulses from tip emitters. *Structural Dynamics* 6, 014301 (2019).
31. Talias, P. Analytical expressions for thermophysical properties of solid and liquid tungsten relevant for fusion applications. *Nuclear Materials and Energy* 13, 42–57 (2017).
32. Ordal, M. A., Bell, R. J., Alexander, R. W., Newquist, L. A. & Query, M. R. Optical properties of Al, Fe, Ti, Ta, W, and Mo at submillimeter wavelengths. *Appl. Opt.* 27, 1203 (1988).
33. Browning, N. D. et al. Recent developments in dynamic transmission electron microscopy. *Curr Opin Solid St M* 16, 23–30 (2012).

34. Picher, M., Bücken, K., LaGrange, T. & Banhart, F. Imaging and electron energy-loss spectroscopy using single nanosecond electron pulses. *Ultramicroscopy* 188, 41–47 (2018).

Chapter 3 - Atomic-Resolution Imaging of Fast Nanoscale

Dynamics with Bright Microsecond Electron Pulses**

3.1 Introduction

Specimen drift presents a fundamental challenge for high-resolution imaging, particularly for in situ experiments where rapid changes of the sample temperature or some other variable induce large amounts of drift.¹ But even the exposure of the sample to the electron beam itself may cause beam-induced sample motion. Specimen motion can be corrected *a posteriori*, if the total electron dose is recorded over several frames in a movie-like fashion. The frames are then aligned before they are added up, allowing one to computationally remove the drift of the sample.² This dose-fractionated imaging method has become crucial in cryo-electron microscopy, thanks to the development of "noise-free" direct electron detectors.² Nevertheless, if the amount of drift present in a movie frame exceeds the target resolution, it has to be discarded. This is frequently the case for the first frames of cryo-electron micrographs, which are particularly affected by beam-induced drift.²

The electron camera's capability of acquiring frames in a sequential manner is also used to observe processes in real time that are purposefully induced in situ, for example with electrical impulses, through mechanical deformation, heating, or laser irradiation of the sample.³⁻⁷ The time resolution of such in-situ experiments is ultimately limited by the frame rate of the electron camera, as is the amount of drift that can be removed with dose-fractionated imaging.

** Adapted from P.K. Olshin, G. Bongiovanni, M. Drabbels, and U.J. Lorenz, Nano Lett. 2021, 21, 1, 612–618. P.K.O. and G.B. contributed equally. Authors Contributions: G.B and P.K.O. performed the experiment and analysed the data; U.J.L. conceived the research; M.D. and U.J.L. designed the experiments; U.J.L. wrote the manuscript with the contribution from all authors.

A vastly higher time resolution can be obtained by imaging with short electron pulses, a principle that is employed in time-resolved electron microscopy to capture processes even on the femtosecond timescale.⁸ However, atomic-resolution imaging with short electron pulses has largely remained elusive. For example, while it has been proposed that it should be possible to image the dynamics of proteins at atomic resolution with a single electron pulse,^{9,10} the spatial resolution currently achieved in such single-shot experiments is several nanometers.¹⁰ The challenge here lies in the creation of electron pulses that are coherent enough to enable atomic-resolution imaging, but also contain a sufficiently large number of electrons to be able to capture the image information in a single shot, or a small number of pulses if the image is recorded stroboscopically.

Here, we demonstrate that such intense, high-brightness electron pulses can be generated by temporarily driving a Schottky field emitter into extreme conditions and thus boosting its emission current to near its limit.¹¹ As illustrated in Fig. 1a,b we do so by irradiating the emitter tip with a microsecond laser pulse, which is generated by chopping the output of a continuous laser beam (532 nm) with an acousto-optic modulator. A mirror embedded within the emitter assembly directs the laser beam at the tip of the Schottky emitter (Fig. 1a), where it is focused to a spot size of 17 μm FWHM. As shown in Fig. 1c, illumination with a 100 μs laser pulse of 0.44 W (green curve) temporarily boosts the probe current (blue) from 60 nA to a peak of 200 nA. Under these conditions, the emitter tip reaches an estimated temperature of about 2500 K, significantly above the maximum safe operating temperature of 1850 K (Ref. 12), which briefly increases the emission current to an extreme value¹¹ that can otherwise not be sustained without damaging the emitter.^{12,13}

3.2 Results and discussion

As illustrated in Fig. 1a, the laser boosted electron beam is chopped into pulses by means of an electrostatic deflector that is placed after the accelerator of the gun and that sweeps the beam over a small aperture. This allows us to generate electron pulses of microsecond duration, as demonstrated in Fig. 1d, and even pulses as short as 100 ns. These laser-boosted pulses are not only intense, but also possess a high instantaneous brightness, 1.7 times higher than without laser enhancement (Appendix I), which is crucial for high-resolution imaging.¹⁴ While we are not able to directly measure the energy spread of the pulsed source, we estimate an increase of about 10% compared to the standard beam (Appendix I). As illustrated in Fig. 1b, the electron gun and deflector assembly are mounted on a JEOL 2010F transmission electron microscope that we have modified for time-resolved experiments.¹⁵ Dynamics of the specimen are initiated in situ with pulses from a 405 nm diode laser that is directed at the sample with a mirror mounted above the upper pole piece of the objective lens (34 μm spot size in the sample plane). A laser boosted electron pulse is then used to capture a snapshot of the dynamics with the electron camera.

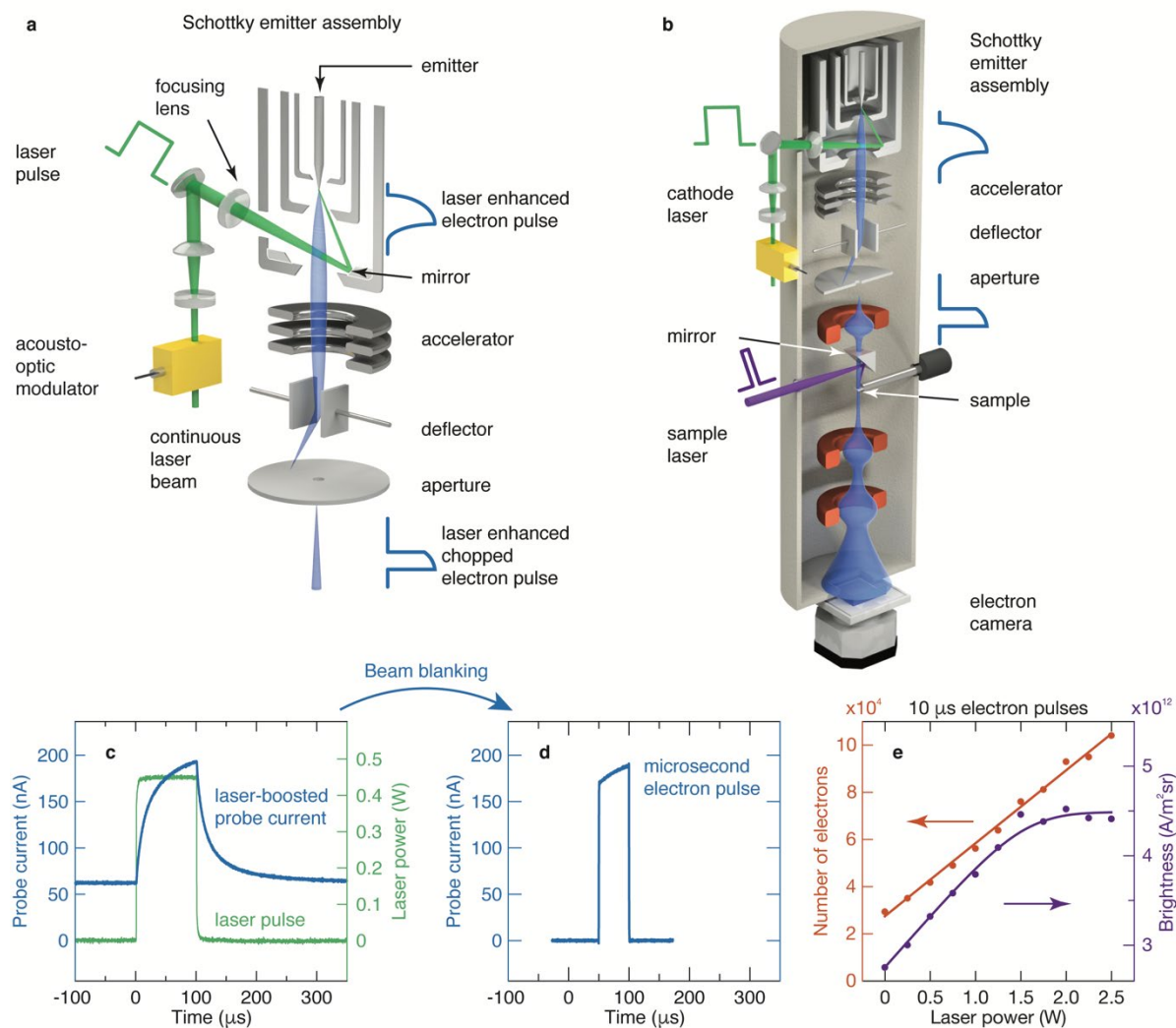


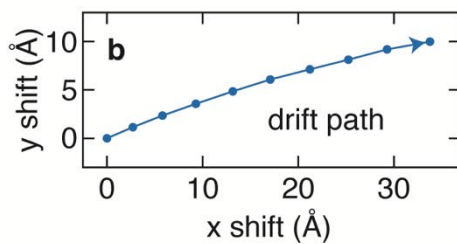
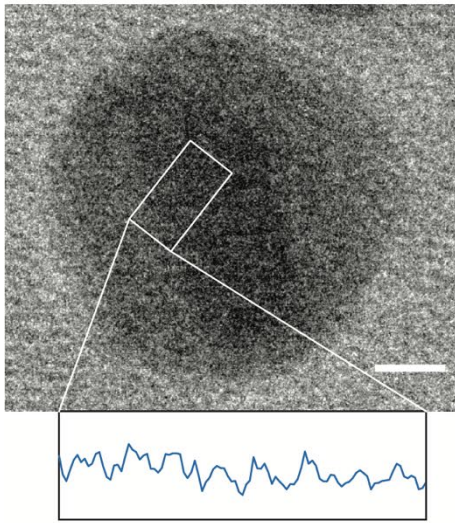
Figure 1. Generation of intense microsecond electron pulses of high brightness. (a) A microsecond laser pulse heats the tip of a Schottky emitter to boost emission, while an electrostatic deflector chops the electron beam into microsecond pulses. (b) Illustration of the time-resolved electron microscope. Dynamics of the sample are initiated with a short laser pulse and probed with a microsecond electron pulse. (c) The probe current (blue) is boosted when the emitter tip is heated with a microsecond laser pulse (green). (d) An intense microsecond electron pulse is obtained by chopping the boosted electron beam with the deflector. (e) Number of electrons in a 10 μs electron pulse (red) and instantaneous brightness (purple) as a function of laser power. The solid lines serve as a guide for the eye.

We first demonstrate the potential of our laser boosted electron pulses to improve the resolution of drift-corrected imaging by delivering the electron dose per movie frame in a short burst instead of spreading it out evenly, so that even larger amounts of drift can be outrun. Figure 2a displays a micrograph of a 15 nm diameter gold particle on an amorphous carbon substrate (full frame image in Supplementary Fig. 2 in Appendix I) acquired with a continuous electron beam while the sample drifted with a speed of 9 nm/s. In order to induce a well-defined amount of drift, the sample was irradiated with a continuous laser beam whose power was increased linearly during acquisition. The image was recorded as a movie of 10 frames of 41 ms duration each, corresponding to the fastest frame rate of our camera at full frame read-out (410 ms total exposure time), and subsequently drift corrected with cisTEM.¹⁶ The drift path obtained in the alignment procedure reveals that the sample drifted by about 3.5 Å per frame (Fig. 2b), which explains the blurry appearance of the image. In contrast, if we acquire each movie frame with a laser-boosted electron pulse of 480 μs duration, the image resolution is markedly improved, as shown in Fig. 2c (same total electron dose and drift, see Fig. 2d). The gold nanoparticle now exhibits lattice fringes, which are also evident in the intensity profile (inset) of the area marked with a rectangle and which are entirely absent in the image recorded with a continuous electron beam.

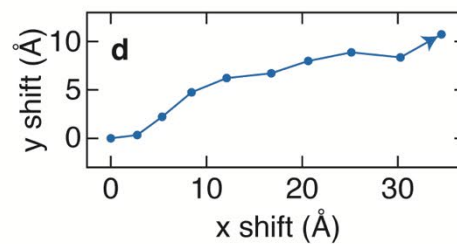
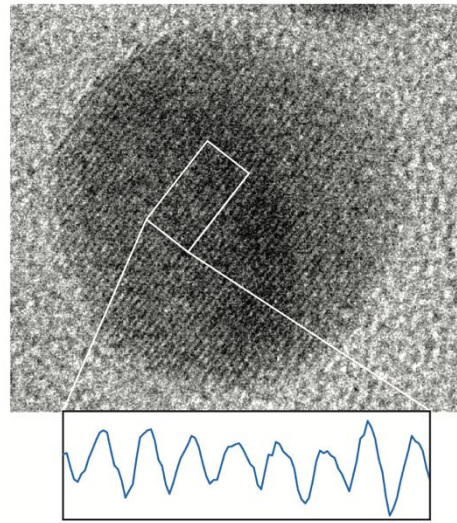
Drift-corrected imaging with microsecond electron pulses

Drift velocity: 9 nm/s

a Continuous electron beam

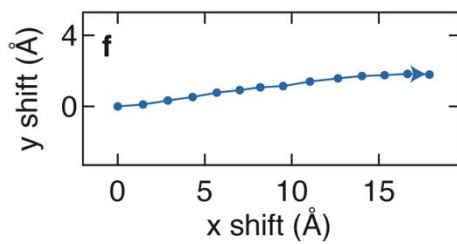
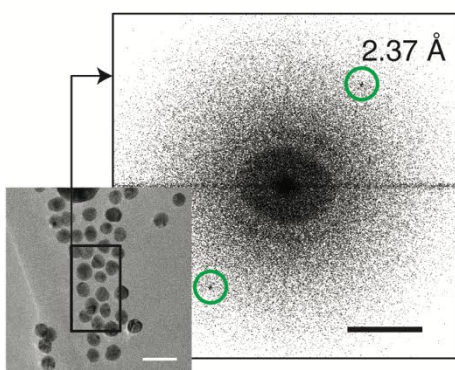


c Electron pulses (480 μ s)



Drift velocity: 3 nm/s

e Continuous electron beam



g Electron pulses (480 μ s)

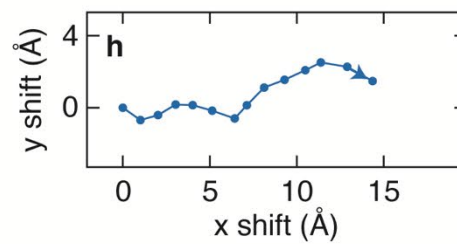
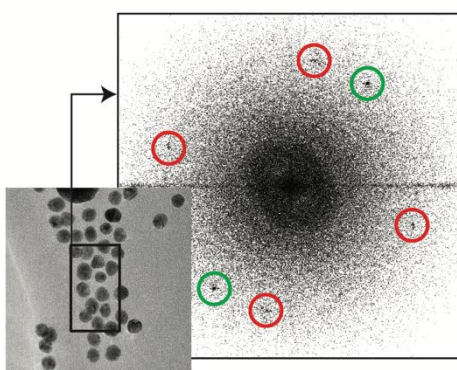


Figure 2. Drift-corrected imaging with microsecond electron pulses. (a, c) Drift-corrected images of a gold nanoparticle (from the full frame micrographs in Supplementary Fig. 2 in Appendix I), recorded with a continuous electron beam (a) and with 480 μs electron pulses (c) in the presence of a drift velocity of 9 nm/s. When imaged with electron pulses, the particle exhibits lattice fringes, as evident in the intensity profile of the region marked with a white rectangle. Scale bar, 3 nm. (b, d) Drift path of the sample during acquisition of the images in (a) and (c), respectively. (e, g) Drift-corrected images of an ensemble of gold nanoparticles, recorded with a continuous electron beam (e) and with 480 μs electron pulses (g) in the presence of a drift velocity of 3 nm/s. Diffractograms of the area marked with a black rectangle reveal several reflections of the gold nanoparticles (2.37 \AA) that are present in the image recorded with a pulsed electron beam, but absent when recorded with a continuous beam. Scale bars, 30 nm and 2.5 nm^{-1} . (f, h) Drift path of the sample during acquisition of the images in (e) and (g), respectively.

Imaging with intense microsecond electron pulses affords an improved resolution even at lower drift rates, similar for example to those encountered in the first movie frames of cryo-electron micrographs.² When we image an ensemble of gold nanoparticles on lacey carbon (Fig. 2e,g) in the presence of about 1.4 \AA drift per frame (Fig. 2f,h), diffractograms of the area marked with a rectangle reveal several reflections (red circles, 2.37 \AA) for the micrograph recorded with pulsed illumination (Fig. 2g) that are absent or much weaker with a continuous beam (Fig. 2e). As we demonstrate in Supplementary Fig. 3 (Appendix I), imaging with electron pulses is also advantageous if drift is not induced by an external stimulus, but instead results from the exposure of the sample to the electron beam itself.

Next, we demonstrate the ability of our intense electron pulses to capture microsecond single-shot images with atomic resolution. Figure 3a displays a 15 nm diameter gold nanoparticle that was imaged with 15 laser-boosted electron pulses of 10 μ s duration. In order to obtain the highest electron dose, the electron beam is almost fully converged, to an area barely larger than the object. Even under such extreme imaging conditions, the particle features lattice fringes, which are also evident in the intensity profile of the area marked with a rectangle as well as the diffractogram of the image (insets). An individual single-shot micrograph is shown in Fig. 3b. Even though it is noisier, it demonstrates that atomic-resolution information can be captured with just a single 10 μ s electron pulse. Another example is presented in Fig. 3c, which shows a micrograph of negatively stained Bacteriophage T4 (Ref. 17), imaged with 20 pulses of 50 μ s duration. An intensity profile and diffractogram (insets) of the phage tail (white bracket) reveal the characteristic 39 Å spacing of the tail sheath proteins,¹⁷ which are also evident in an individual single-shot image (Fig. 3d). We conclude that pulses of tens of microseconds offer sufficient contrast for single-shot imaging while being coherent enough to achieve atomic resolution.

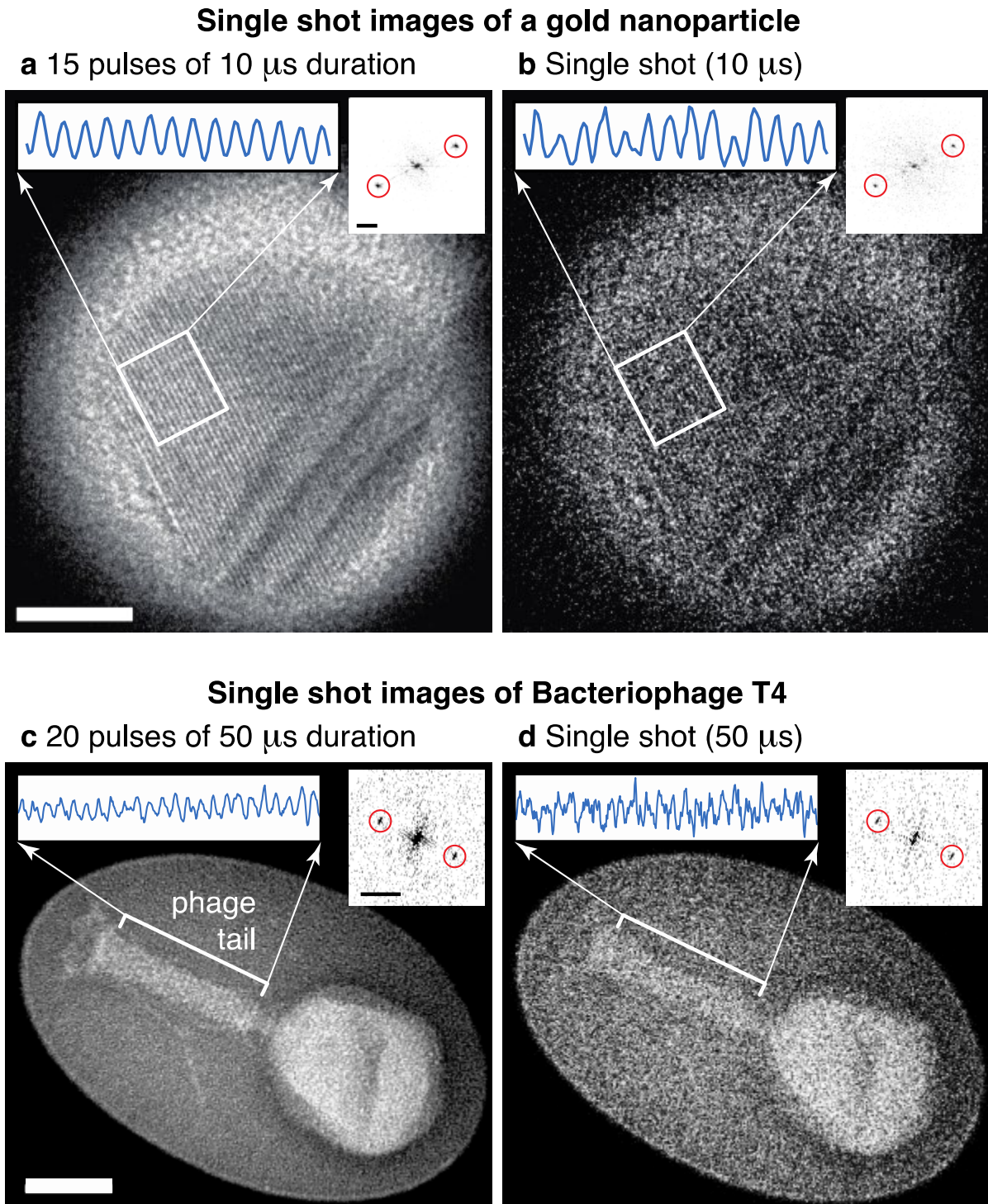


Figure 3. Atomic-resolution single-shot imaging. (a, b) Single-shot images of a gold nanoparticle recorded with 10 μs electron pulses. In (a), 15 pulses of 10 μs duration are averaged, while (b) shows an image recorded with an individual 10 μs pulse. Line profiles of the area marked with a rectangle (left insets) and diffractograms of the particle (right insets)

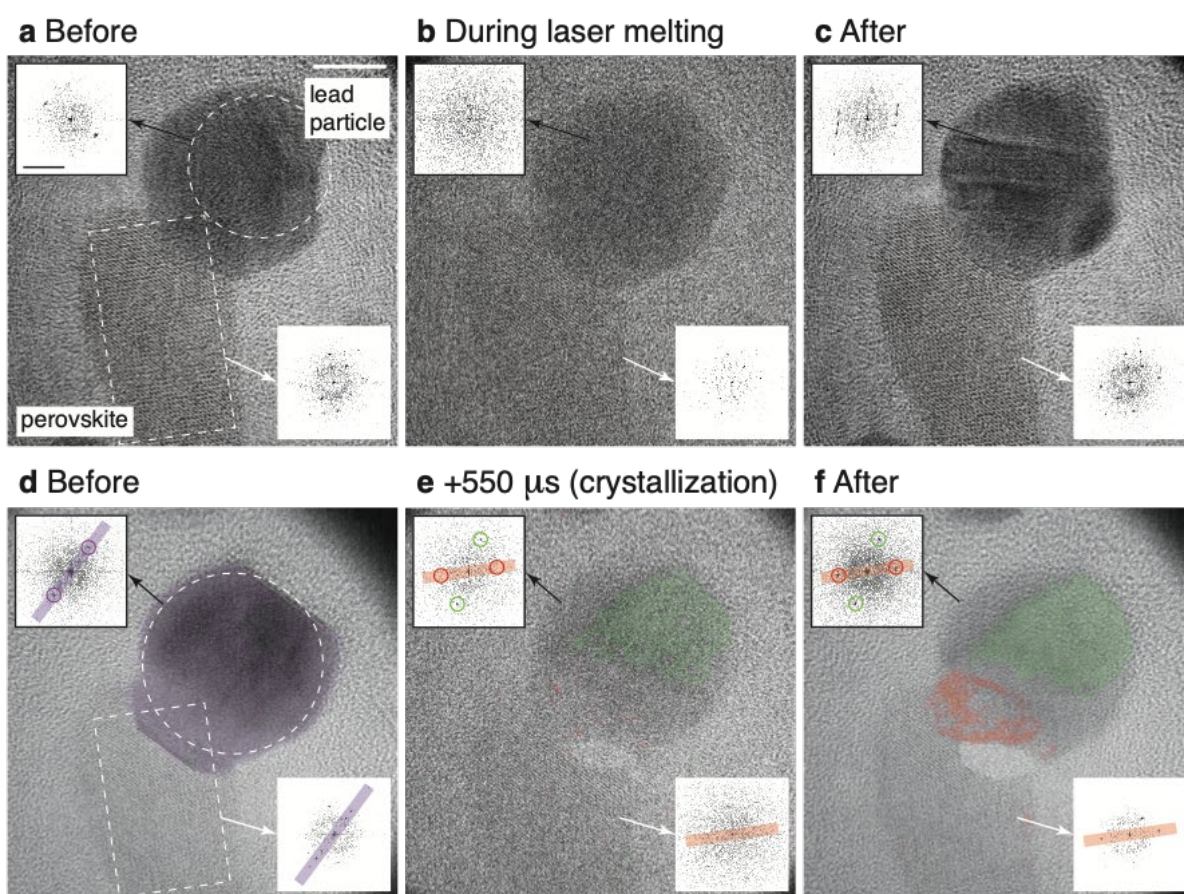
reveal lattice fringes with a spacing of 2.35 Å. Scale bars, 5 nm, as well as 2 nm⁻¹ in the inset. (c, d) Single-shot images of negatively stained Bacteriophage T4 recorded with 50 μs electron pulses. In (c), 20 pulses of 50 μs duration are averaged, while (d) shows an image recorded with an individual 50 μs pulse. Intensity profiles (left insets) and diffractograms (right insets) of the area corresponding to the phage tail (marked with a white bracket) reveal the spacing of the tail sheath proteins of 39.0 Å. Scale bars, 50 nm, as well as 0.25 nm⁻¹ in the inset.

Finally, we demonstrate that our laser-boosted electron pulses allow us to capture fast, atomic-scale transformations in a single shot. We illustrate this by studying the competing crystallization pathways of an individual lead nanoparticle (Fig. 4a, circle), which we melt in situ with a laser pulse (500 μs, 1 mW), before letting it rapidly crystallize in the presence of an adjacent CsPbBr₃ perovskite nanocrystal (rectangle) that provides a nucleation seed. A single-shot image recorded during the laser pulse (Fig. 4b) establishes that the lead particle is completely melted, while the perovskite remains crystalline (see also the diffractograms of the particles in the insets). Subsequently, the lead particle crystallizes in a new configuration with several crystalline domains (Fig. 4c).

When we repeat the crystallization process, different configurations are randomly obtained. Frequently however, the perovskite nanocrystal appears to act as a nucleation seed (Supplementary Fig. 4 in Appendix I) creating configurations such as the one in Fig. 4d in which the lattice fringes of the lead particle are parallel to a set of planes of the perovskite crystal. This is also evident in the diffractograms, where the corresponding sets of reflections of both particles fall onto the same line (highlighted with purple bars). The lead particle has formed a

single-crystal, as evident from the purple overlay highlighting areas of the same crystal orientation that was obtained by Fourier filtering with the reflections selected that are circled in the diffractogram. Melting and recrystallization creates yet another configuration (Fig. 4f), which appears to result from the competition of different crystallization pathways. While the lattice fringes visible in the top (green) are randomly oriented, those in the bottom (red) are aligned with another set of lattice planes of the adjacent perovskite crystal (red bars in the diffractograms). A snapshot of the crystallization process yields insights into the crystallization trajectory (Fig. 4e). Surprisingly, formation of the randomly oriented domain (green) precedes that of the heterogeneously nucleated domain (red), which appears to be just forming in the single-shot image. Such real-time observations promise to elucidate a range of phenomena that have so far only been studied theoretically for rapidly crystallizing metal nanoparticles, such as the cross-nucleation of polymorphs¹⁸ or the fate of crystallization seeds during crystal growth.¹⁹

Crystallization of an individual lead nanoparticle



Amorphization of a perovskite nanocrystal

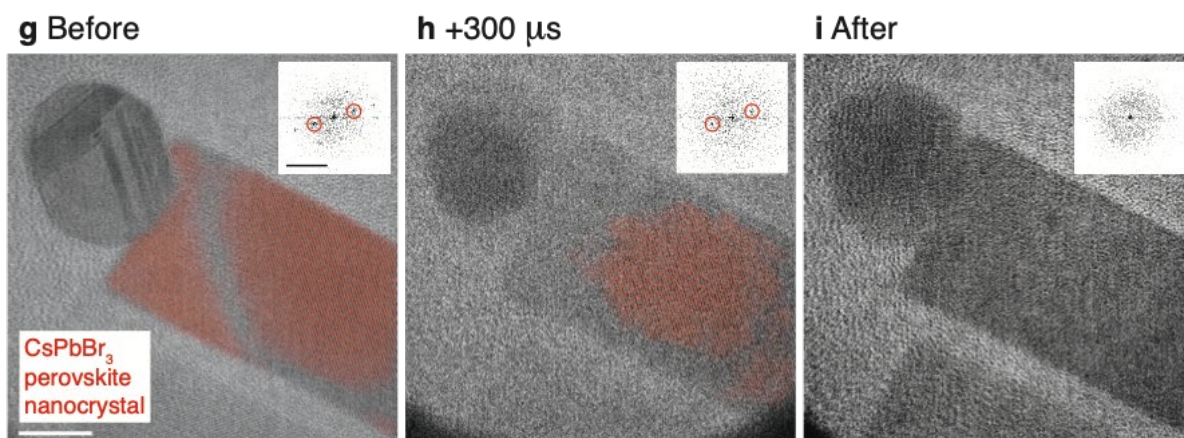


Figure 4. Single-shot imaging of atomic-scale transformations of nanoparticles. (a-f) Competing crystallization pathways of an individual lead nanoparticle. The lead particle (marked with circle in a) is melted in situ with a laser pulse (500 μ s, 1 mW), with the adjacent perovskite nanocrystal

(rectangle) providing a nucleation seed for the subsequent crystallization process. A snapshot recorded during laser irradiation (b) reveals that the lead particle is completely melted, while the perovskite remains crystalline (100 μs electron pulse, 200 μs before the end of the laser pulse). After the laser pulse, the lead particle cools and recrystallizes in a different configuration (c). The insets show diffractograms of both particles. (d-f) The melting and recrystallization process is repeated (500 μs laser pulse, 2 mW), creating another configuration of the lead particle with several crystalline domains (f). Colored overlays highlight domains of different orientation and are obtained by Fourier filtering the images with the reflections selected that are circled in the diffractograms in the insets. A snapshot taken during the crystallization process (e, 550 μs after the end of the laser pulse) reveals that the formation of the domain highlighted in green precedes that of the domain highlighted in red. Colored bars in the diffractograms highlight sets of reflections of the lead particle and the perovskite that are parallel to each other, suggesting that the perovskite acted as a nucleation seed in the crystallization process. Scale bars, 10 nm and 5 nm^{-1} . g-i, Amorphization of a perovskite nanocrystal under laser heating. The CsPbBr_3 nanocrystal in g is rendered amorphous after illumination with a 500 μs laser pulse of 1 mW power (i), as evident from the diffractogram of the crystal in the inset. A snapshot recorded after 300 μs of laser irradiation (h) reveals that amorphization is initiated at the crystal boundaries (100 μs electron pulse). The red overlay highlights crystalline domains and is obtained by Fourier filtering the images with the reflections selected that are circled in the diffractogram in the inset. Scale bars, 10 nm and 5 nm^{-1} .

As another example, we study the structural transformations that CsPbBr₃ perovskite nanocrystals^{20,21} undergo at elevated temperatures. The perovskite nanocrystal in Fig. 4g features a single crystalline domain highlighted in red. Heating the crystal with a 500 μ s laser pulse (1 mW) renders it amorphous (Fig. 4i), a process that is known to be associated with the degradation of the performance of perovskite nanocrystals in optoelectronic applications and that hinders their use in high-power devices.²² A snapshot taken during laser irradiation provides a subparticle picture of the mechanism involved, revealing that amorphization is initiated at the crystal boundaries and propagates inward (Fig. 4h). We estimate that the amorphous domain expands with a speed of 35 nm/ms along the long axis of the crystal, and with 5-12 nm/ms along its short axis. These observations suggest that interfaces play an important role in the high-temperature amorphization of perovskite nanocrystals and that their modification may provide a means to improve temperature stability.

3.3 Conclusions

In conclusion, we demonstrate both static and dynamic atomic-resolution imaging with intense, high-brightness electron pulses from a field emitter. We show that such electron pulses enable high-resolution imaging in the presence of large amounts of drift. For example, if 0.2 \AA drift per frame are acceptable, then even a staggering drift rate of 40 nm/s can be tolerated if one images with 500 μ s electron pulses, as we have done here. This particularly stands to benefit the field of in situ electron microscopy, where drift presents a fundamental challenge,¹ but may also be useful for any kind of high-resolution imaging affected by beam induced drift, such as cryo-electron microscopy. Atomic-resolution single-shot imaging with microsecond time resolution will enable the study of a wide range of irreversible atomic-scale

processes. Of particular interest are the dynamics of proteins whose relevant motions frequently occur on the microsecond to millisecond timescale.²³ Our experiments suggest that single-shot imaging of proteins in liquid in the presence of negative stain will be possible.¹⁰ For unstained samples, it may be necessary to increase the pulse duration or image stroboscopically. Finally, we note that a particularly appealing feature of our method is that switching the microscope to pulsed operation can be done on the fly and without changing alignment.¹

3.4 Methods

Time-resolved transmission electron microscopy

Experiments were performed with a modified JEOL 2010F transmission electron microscope that we have previously described.¹⁵ Intense, high-brightness electron pulses of microsecond duration are generated with a Schottky field emission gun operating at 200 kV accelerating voltage. For the duration of the electron pulse, the emission current is boosted by illuminating the emitter tip with an intense microsecond laser pulse.¹¹ To this end, the output of a continuous laser (532 nm, 1.5 W, Coherent Verdi) is chopped into microsecond pulses with an acousto-optic modulator (AA Opto-Electronic, 50 ns rise time). The laser beam is then directed onto the emitter tip (Fig. 1a,b) where it is focused to a spot size of 17 μm FWHM. Laser illumination temporarily heats the emitter tip to an extreme temperature of 2500 K, almost quadrupling the emission current and increasing it to near its limit without damaging the emitter.¹¹ The boosted electron beam is then chopped into pulses of variable duration by means of an electrostatic deflector that we installed between the electron gun and the microscope column (Fig. 1a,b) and that consists of two stainless steel plates (2 mm distance, 11 mm height, and 8 mm width). By applying a 400 V pulse to one of the plates with a fast high-voltage switch (Behlke), the beam is swept over a 300 μm aperture located at a distance of about 10 cm from the deflector (Fig. 1a,b). We can thus obtain laser-boosted electron pulses of microsecond duration, and even pulses as short as 100 ns. In order to induce sample drift or trigger dynamics, the sample is illuminated with the modulated output of a 405 nm diode laser (Cobolt, 2.5 ns rise/fall time), which is focused to a spot size of 34 μm FWHM, as measured with a knife-edge scan at the sample position.

Drift-corrected imaging with microsecond electron pulses

For the experiments in Fig. 2, reproducible amounts of drift were induced by illuminating the sample with a continuous laser beam. In Fig. 2a,c, the laser power was held at 0.31 mW and linearly ramped to 2.6 mW during image acquisition (about 1 s total exposure time), resulting in an average sample drift velocity of 9 nm/s. In Fig. 2e,g, the laser power was set to 0.26 mW and ramped to 0.8 mW, resulting in a drift of 3 nm/s. All images in Fig. 2 were recorded as 1 s movies (full-frame) of 25 frames. While the images in Fig. 2a,e were acquired with a continuous electron beam and a dose rate of 9 electrons/pixel/s, those in Fig. 2c,g were recorded with 480 μ s electron pulses (one pulse per movie frame) and the same total electron dose. We note that for pulsed illumination, the electron beam is more converged than in the images acquired with a continuous electron beam.

In order to ensure a fair comparison between the drift-corrected images recorded with a continuous electron beam and those acquired with electron pulses, the following procedure was followed. First, both movies were cropped to show exactly the same area of the sample, so that the effectiveness of the drift correction algorithm would not be affected by the visibility of different features in the two movies. The movie frames were then aligned with cisTEM¹⁶ to determine the drift path of the sample. Since the drift paths of both movies differed slightly at the beginning and at the end, the initial and final frames were discarded, leaving only 10 frames in the micrographs of Fig. 2a,c and 14 frames in the micrographs of Fig. 2e,g. Finally, these remaining frames were again aligned with cisTEM to yield the images shown in Fig. 2.

Atomic-resolution single-shot imaging

Single-shot experiments with laser-boosted electron pulses are performed with the electron beam almost fully converged on the sample and the illuminated area of the sample barely

larger than the object under observation. In the micrographs of bacteriophage T4 in Fig. 3c,d, the condenser lens stigmators were used to adjust the beam shape to the dimensions of the object. The micrographs in Fig. 3a,c were obtained by recording 15 and 20 single-shot images, respectively, which were then drift-corrected and averaged.

In-situ growth of perovskite nanoparticles and in-situ synthesis of lead nanoparticles

For the experiment on the high-temperature amorphization of perovskite nanocrystals (Fig. 4g-i), a CsPbBr₃ perovskite nanocrystal of suitable dimensions was grown in situ. We laser evaporate an ensemble of CsPbBr₃ perovskite quantum dots (Sigma-Aldrich) that had been deposited on a graphene oxide on lacey carbon specimen grid. At a distance from the laser focus where the temperature of the specimen grid is lower, the vapor condenses, and perovskite nanocrystals with a characteristic rectangular outline grow, such as the one in Fig. 4g. Our in-situ growth of perovskite nanoparticles resembles various vapor-phase epitaxy protocols that have previously been described.²⁴

The lead nanoparticle in Fig. 4a-f was formed in situ as a side product of laser irradiation of CsPbBr₃ perovskite quantum dots. The identity of the particle is confirmed by the diffractograms of its various configurations that we created by recrystallizing the particle in situ. Synthesizing the lead particle in situ avoids the formation of an oxide layer on its surface.

3.5 References

1. Taheri, M. L. et al. Current status and future directions for in situ transmission electron microscopy. *Ultramicroscopy* 170, 86–95 (2016).
2. Cheng, Y., Grigorieff, N., Penczek, P. A. & Walz, T. A Primer to Single-Particle Cryo-Electron Microscopy. *Cell* 161, 438–449 (2015).
3. Westenfelder, B. et al. Graphene-based sample supports for in situ high-resolution TEM electrical investigations. *J. Phys. D: Appl. Phys.* 44, 055502 (2011).
4. Zeng, Z. et al. Visualization of Electrode–Electrolyte Interfaces in LiPF₆/EC/DEC Electrolyte for Lithium Ion Batteries via in Situ TEM. *Nano Lett.* 14, 1745–1750 (2014).
5. Liu, Z. et al. Tensile deformation and fracture mechanisms of Cu/Nb nanolaminates studied by in situ TEM mechanical tests. *Extreme Mechanics Letters* 25, 60–65 (2018).
6. Foster, D. M., Pavludis, Th., Kioseoglou, J. & Palmer, R. E. Atomic-resolution imaging of surface and core melting in individual size-selected Au nanoclusters on carbon. *Nat Commun* 10, 2583 (2019).
7. Voss, J. M., Olshin, P. K., Charbonnier, R., Drabbels, M. & Lorenz, U. J. In Situ Observation of Coulomb Fission of Individual Plasmonic Nanoparticles. *ACS Nano* 13, 12445–12451 (2019).
8. Zewail, A. H. Four-Dimensional Electron Microscopy. *Science* 328, 187–193 (2010).
9. Evans, J. E. & Browning, N. D. Enabling direct nanoscale observations of biological reactions with dynamic TEM. *Microscopy-Jpn* 62, 147–156 (2013).
10. Zhang, L., Hoogenboom, J. P., Cook, B. & Kruit, P. Photoemission sources and beam blankers for ultrafast electron microscopy. *Structural Dynamics* 6, 051501 (2019).
11. Bongiovanni, G., Olshin, P. K., Drabbels, M. & Lorenz, U. J. Intense microsecond electron pulses from a Schottky emitter. *Appl. Phys. Lett.* 116, 234103 (2020).

12. van Veen, A. H. V., Hagen, C. W., Barth, J. E. & Kruit, P. Reduced brightness of the ZrO/W Schottky electron emitter. *Journal of Vacuum Science & Technology B: Microelectronics and Nanometer Structures Processing, Measurement, and Phenomena* 19, 2038–2044 (2001).
13. Cook, B., Verduin, T., Hagen, C. W. & Kruit, P. Brightness limitations of cold field emitters caused by Coulomb interactions. *J Vac Sci Technol B* 28, C6c74-C6c79 (2010).
14. Tiemeijer, P. C., Bischoff, M., Freitag, B. & Kisielowski, C. Using a monochromator to improve the resolution in TEM to below 0.5Å. Part I: Creating highly coherent monochromated illumination. *Ultramicroscopy* 114, 72–81 (2012).
15. Olshin, P. K., Drabbels, M., & Lorenz, U. J. Characterization of a Time-Resolved Electron Microscope with a Schottky Field Emission Gun. *Structural Dynamics* 7, in press (2020).
16. Grant, T., Rohou, A. & Grigorieff, N. cisTEM, user-friendly software for single-particle image processing. *eLife* 7, e35383 (2018).
17. Kostyuchenko, V. A. et al. The tail structure of bacteriophage T4 and its mechanism of contraction. *Nat Struct Mol Biol* 12, 810–813 (2005).
18. Desgranges, C. & Delhommelle, J. Molecular Mechanism for the Cross-Nucleation between Polymorphs. *J. Am. Chem. Soc.* 128, 10368–10369 (2006).
19. Allahyarov, E., Sandomirski, K., Egelhaaf, S. U. & Löwen, H. Crystallization seeds favour crystallization only during initial growth. *Nature Communications* 6, 7110 (2015).
20. Protesescu, L. et al. Nanocrystals of Cesium Lead Halide Perovskites (CsPbX₃, X = Cl, Br, and I): Novel Optoelectronic Materials Showing Bright Emission with Wide Color Gamut. *Nano Lett.* 15, 3692–3696 (2015).

21. Akkerman, Q. A., Rainò, G., Kovalenko, M. V. & Manna, L. Genesis, challenges and opportunities for colloidal lead halide perovskite nanocrystals. *Nature Mater* 17, 394–405 (2018).
22. Liao, M., Shan, B. & Li, M. In Situ Raman Spectroscopic Studies of Thermal Stability of All-Inorganic Cesium Lead Halide (CsPbX₃, X = Cl, Br, I) Perovskite Nanocrystals. *J. Phys. Chem. Lett.* 10, 1217–1225 (2019).
23. Henzler-Wildman, K. & Kern, D. Dynamic personalities of proteins. *Nature* 450, 964–972 (2007).
24. Wang, Y. et al. Epitaxial Growth of Large-Scale Orthorhombic CsPbBr₃ Perovskite Thin Films with Anisotropic Photoresponse Property. *Advanced Functional Materials* 29, 1904913 (2019).

Chapter 4 - Near-atomic resolution reconstructions from in situ revitrified cryo samples

4.1 Introduction

Proteins play a crucial role in most biological processes. They catalyze reactions, regulate gene expression, receive and transmit biological signals, and participate in the recognition of pathogens.¹⁻⁴ To perform their tasks, they undergo large-scale domain motions that bear resemblance to those of man-made machines.⁵ However, because of the fast timescale of these motions, typically microseconds, it has largely remained impossible to observe them directly, which has left our understanding of protein function fundamentally incomplete.⁶⁻⁸ In fact, it has been argued that understanding protein function represents the next frontier in structural biology.⁹

We have recently introduced a novel approach to time-resolved cryo-EM that affords microsecond time resolution. It thus promises to significantly advance our understanding of protein function by enabling direct observations of the motions of proteins.¹⁰⁻¹² Our approach involves rapidly melting a cryo sample with a laser beam. Once the sample is liquid, conformational dynamics are triggered with a suitable stimulus, for example by releasing a caged compound or directly exciting a photoactive protein with a second laser pulse.¹³⁻¹⁵ As the particle dynamics unfold, the heating laser is switched off at a well-defined point in time, and the sample revitrifies within just a few microseconds, trapping the particles in their transient configurations, in which they can subsequently be imaged with conventional cryo-EM techniques.¹⁰

We have previously described two different implementations of our technique. Melting and revitrification experiments can be performed in an optical microscope, using a correlative light-electron microscopy approach.¹⁶ Alternatively, such experiments can be carried out in situ¹⁰⁻¹² with a modified transmission electron microscope.¹⁷ In situ experiments offer the advantage that electron micrographs of revitrified areas can provide an immediate feedback on conformational changes of the proteins. It is even possible to perform on-the-fly reconstructions to guide the search for suitable experimental parameters. Moreover, it is straightforward to determine the diameter of the revitrified area from electron micrographs, which can be monitored to adjust the laser power in revitrification experiments, as we have previously described.¹¹ A potential drawback of in situ experiments is that the sample has to be exposed to a small electron dose (about 10^{-3} electrons/Å²) in order to locate a suitable area and aim the laser beam. This is a potential issue since we have previously observed that exposure to a dose as low as a few electrons/Å² prior to revitrification induces enough beam damage to cause the particles to disassemble once the sample has turned liquid.¹⁰ We have recently demonstrated that in situ revitrification does not alter the structure of the proteins.¹² However, the resolution of the reconstructions we obtained was limited by the performance of our instrument to a few Angstroms. This leaves open the question whether in situ revitrification might induce structural changes that only become evident at higher spatial resolution or might even limit the obtainable resolution.

Here, we show that near-atomic resolution reconstructions can be obtained from in situ revitrified cryo samples by transferring them to a high-resolution electron microscope for cryo imaging. Interestingly, our analysis reveals that rapid melting and revitrification reshuffles the particles, creating a more homogeneous angular distribution.

4.2 Results and discussion

Figure 1 illustrates the experimental workflow. A cryo sample of mouse heavy-chain apoferritin was prepared on a UltrAuFoil specimen support, which features a holey gold film (1.2 μm diameter holes) on a 300 mesh gold grid (Figure 1a). In situ melting and revitrification experiments were then performed with a JEOL 2200FS transmission electron microscope that we have modified for time-resolved experiments (Figure 1b).¹⁷ The melting laser (532 nm) is directed at the sample with the help of an aluminum mirror placed above the upper pole piece of the objective lens, so that the laser beam strikes the sample at close to normal incidence. To perform a melting and revitrification experiment, the laser beam was aimed at the center of a grid square, and a 20 μs laser pulse was used to revitrify an area of typically about 25 holes. The sample was then transferred to a Titan Krios G4 (Thermo Fisher Scientific) for high-resolution imaging (Figure 1c). Micrographs were collected from 16 revitrified areas as well as 11 conventional areas that had not been exposed to the laser beam. Finally, single-particle reconstructions of both data sets were performed with CryoSPARC¹⁸ to yield near-atomic resolution maps (Figure 1d).

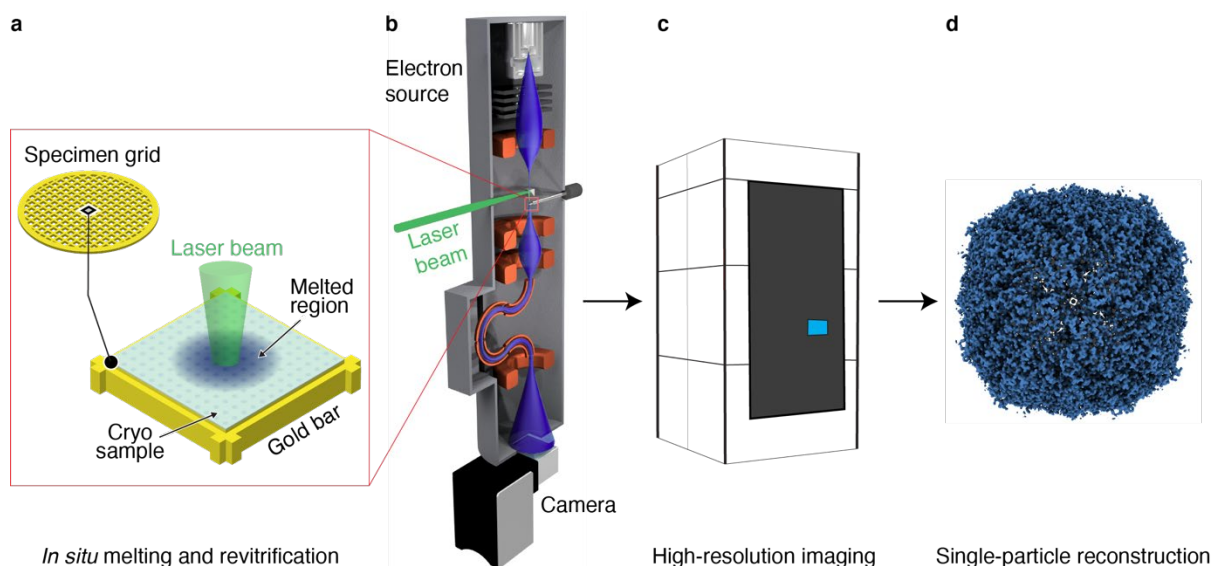


Figure 1. Illustration of the workflow to obtain for near-atomic resolution reconstruction from in situ revitrified cryo samples. (a,b) Cryo samples on UltrAuFoil grids are melted and revitrified in situ with a modified JEOL 2200F transmission electron microscopes. (c) The samples are then transferred to a Titan Krios G4 for high-resolution imaging. (d) Single-particle reconstructions from the revitrified areas yield near-atomic resolution maps.

Figure 2 compares the reconstructions obtained from the conventional (left) and revitrified areas (right). Within our resolution (1.61 Å and 1.59 Å, respectively), the maps are undistinguishable. This is also evident in the details of side chains shown in Figure 2b, which reveal well-resolved densities of aromatic rings as well as individual water molecules. A model of mouse heavy-chain apoferritin is shown¹⁹ that we have placed into the density through rigid-body fitting. These results confirm our previous observations that the in situ melting and revitrification process leaves the proteins intact.¹² Moreover, we can determine to atomic-scale precision that under our experimental conditions, in situ revitrification does not alter the structure of the particles, nor does reduce the obtainable spatial resolution. Evidently, the small

electron dose of about 10^{-3} electrons/Å² that the sample is exposed to in an in situ experiment prior to revitrification does not cause sufficient beam damage to deteriorate the resolution.

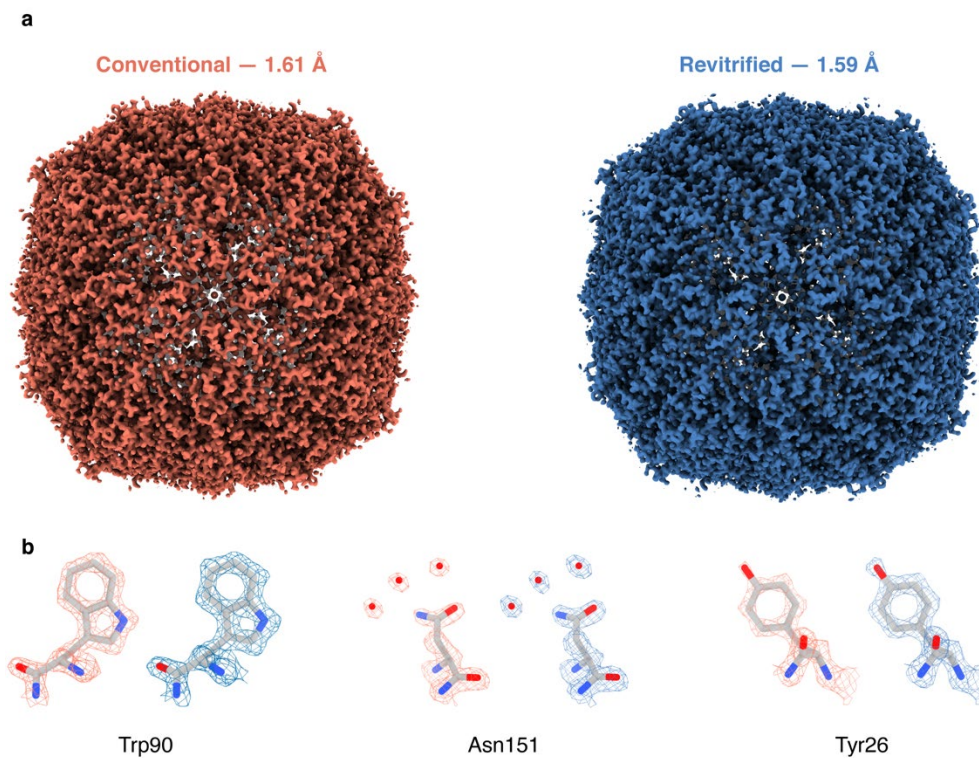


Figure 2. Near-atomic resolution reconstructions of apoferritin from conventional and revitrified areas. (a) The maps from conventional (left) and revitrified areas (right) are indistinguishable within the resolution obtained (~ 1.6 Å). (b) Details of the reconstructions show well-resolved side chain densities as well as individual water molecules. A model of apoferritin¹⁹ is placed into the density through rigid body fitting.

Interestingly, melting and revitrification results in a more homogeneous angular distribution of the particles. This is evident in Figure 3a, which compares the distributions for the conventional (left) and revitrified sample areas (right). Preferred particle orientations in cryo samples are thought to arise due to the adhesion of hydrophobic regions of the protein surface to the air-water interface.²⁰ Such effects are small for apoferritin, which exhibits little

orientational preference. The angular distribution features six narrow, symmetry equivalent maxima. Each is surrounded by eight broad, shallow minima, which fall into two groups of four that are related to each other by symmetry. After revitrification, this distribution is markedly broadened, with the ratio of the populations of the most and least probable orientation decreasing from 1.6 to 1.3.

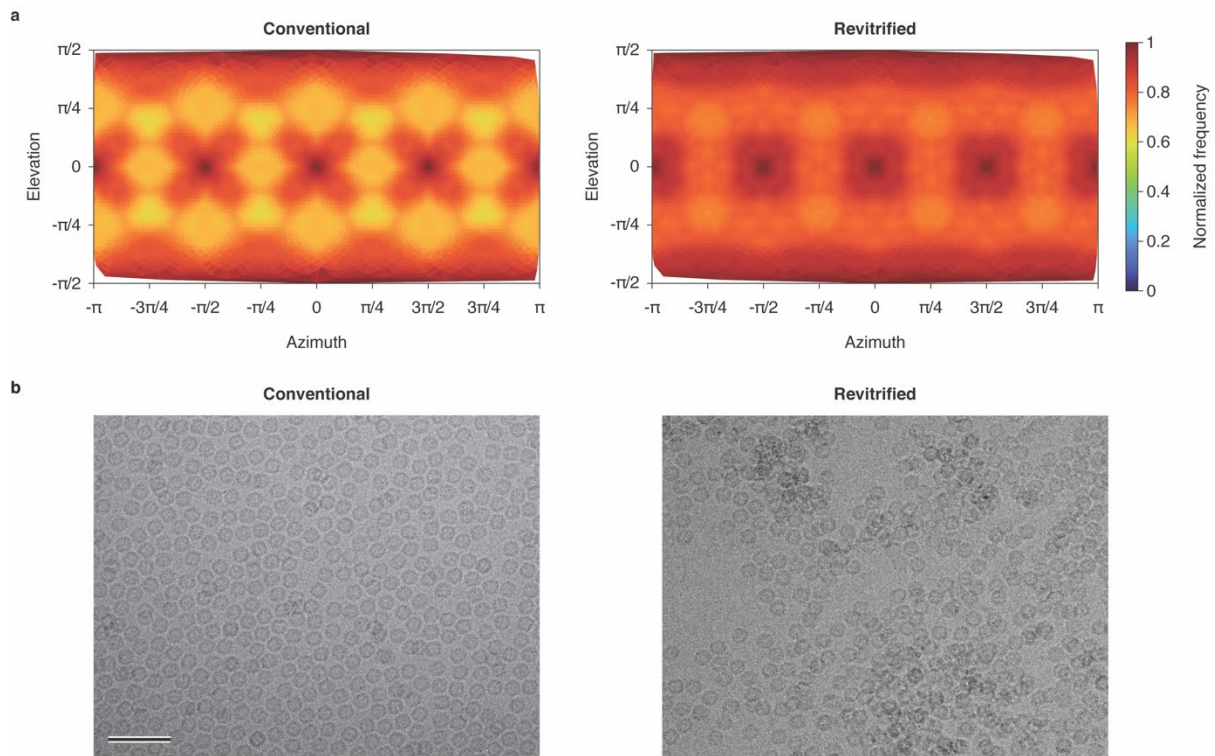


Figure 3. Revitrification reshuffles the particles, which results in a more homogeneous angular distribution. (a) Distribution of particle views in the conventional (left) and revitrified sample areas (right). The distributions are shown with octahedral symmetry applied. (b) A micrograph of a conventional sample area shows a homogeneous distribution of the particles (left), whereas an uneven particle distribution is observed in revitrified areas (right). Scalebar 50 nm.

The broadening of the angular distribution upon revitrification is accompanied by changes in the spatial distribution of the particles, which provides hints as to the underlying mechanism.

Figure 3b shows that while conventional samples typically feature a homogeneous particle distribution (left), revitrification results in an uneven distribution, with the particles clustering in some areas. Evidently, rapid laser melting of the sample reshuffles the particles and creates a non-equilibrium spatial and angular distribution. The time window during which the sample is liquid ($< 20 \mu\text{s}$) is manifestly insufficient to reestablish an equilibrium distribution as it is initially prepared during the plunge freezing process, where the sample is given about 1 s to equilibrate between blotting and plunging. Revitrification therefore traps a non-equilibrium distribution. This is also consistent with the expected rotational timescales. The rms rotation angle of freely diffusing apoferritin is about 80 degrees on a timescale of $10 \mu\text{s}$. However, near a surface, particles frequently experience so-called anomalous diffusion, with diffusion coefficients lowered by several orders of magnitude.²¹ The rms rotation angle in our experiment is therefore likely lower than the separation between the maxima and minima of the angular distribution (Figure 3a).

Several phenomena may potentially explain the reshuffling of the particles during the melting process. As we have previously described, the sample partially crystallizes during rapid laser heating when it traverses so-called no man's land.¹¹ It is conceivable that the formation of ice crystallites and their subsequent melting exert small forces upon the particles that scramble their distribution. Another possibility is that stresses present in the vitreous ice film that build up during plunge freezing due to the difference in expansion coefficient between gold and water²² are unevenly released during rapid laser melting, causing a microscopic flow of the liquid to reshuffle the particles. Further experiments will be needed to definitively settle this point.

4.3 Conclusion

Our experiments demonstrate that near-atomic resolution reconstructions can be obtained from in situ melted and revitrified cryo samples, in agreement with previous results for samples that we revitrified in an optical microscope.¹⁶ This strongly suggests that the revitrification process does not impose a fundamental limit on the obtainable spatial resolution. Evidently, the small electron dose that the sample is exposed to in an in situ experiment prior to melting and revitrification does not alter the protein structure or the achievable resolution. This is an important result since in situ experiments offer the advantage over revitrification with an optical microscope that they can provide an immediate feedback, which speeds up the search for suitable experimental parameters.

The observed scrambling of the angular distribution of the particles during revitrification may potentially offer a means to overcome issues with preferred orientation that in some samples cause views to be underrepresented or even absent, making it difficult to obtain a reconstruction.²³ While tilting the sample during imaging can be used to mitigate this effect,^{23,24} tilting to high angles reduces the obtainable resolution.²³ Instead, laser revitrification may potentially be employed to repopulate hidden views without the need for tilting. Further experiments will be needed to determine whether this will be possible in samples with a strong preferred orientation and to find experimental parameters that maximize the effect.

4.4 Methods

Cryo specimens were prepared on UltrAuFoil R1.2/1.3 300 mesh grids (Quantifoil). The grids were plasma cleaned for 1 min to render them hydrophilic (Tedpella "EasyGlow").

Subsequently, 3 μl of the sample solution (mouse heavy chain apoferritin, 8.5 mg/ml in 20 mM HEPES buffer with 300 mM sodium chloride at pH 7.5) were applied, and the samples were plunge-frozen using a Vitrobot Mark IV (Thermo Fisher Scientific, 3 s blotting time, 95% relative humidity at a temperature of 10 °C).

In-situ revitrification experiments were carried out with a modified JEOL 2200FS transmission electron microscope,¹⁷ using a Gatan Elsa single-tilt cryo holder. Microsecond laser pulses for melting and revitrification (76 mW) were obtained by modulating the output of a 532 nm continuous wave laser (Laser Quantum, Ventus 532) with an acousto-optic modulator (AA optoelectronics). The beam was focused in the sample plane, giving an elliptical spot of 62 μm \times 165 μm FWHM, as determined from a knife edge scan. Before transferring the sample for high-resolution imaging, an atlas was recorded, which allowed us to readily identify the revitrified areas later.

The micrographs in Figure 3b were recorded with the JEOL 2200FS. High-resolution micrographs for single-particle reconstructions (Figure 2 and 3) were collected on a Titan Krios G4 (Thermo Fisher Scientific), which was operated at 300 kV acceleration voltage. Zero-loss filtered images (Selectris X energy filter, 10 eV slit width) were recorded with a Falcon 4 camera, using an exposure time of about 2.5 s for a total dose of 50 electrons/ \AA^2 . The pixel size was set to 0.455 \AA . Defocus values were in the range of 0.5–1.2 μm .

Single-particle reconstructions were performed in cryoSPARC 3.3.1 (Ref. 18) (details in the Supporting Information). The conventional (revitrified) dataset — both recorded on the same specimen grid — contained 4745 (1591) images, which were patch motion corrected. After CTF

estimation, 1815 (1552) micrographs with a resolution better than 6 Å were retained. Template-based particle picking yielded 114414 (88004) particles. After two rounds of 2D classification, 91541 (74468) particles were retained, which were used for ab initio reconstruction (C1 symmetry), followed by heterogeneous refinement using 2 classes (C1 symmetry). The 72270 (72811) particles in the most populated class were then used for homogeneous refinement with O symmetry, giving a map with 1.61 Å (1.59 Å) resolution.

4.5 References

1. Benkovic, S. J. & Hammes-Schiffer, S. A Perspective on Enzyme Catalysis. *Science* 301, 1196–1202 (2003).
2. Buccitelli, C. & Selbach, M. mRNAs, proteins and the emerging principles of gene expression control. *Nat Rev Genet* 21, 630–644 (2020).
3. Wootten, D., Christopoulos, A., Marti-Solano, M., Babu, M. M. & Sexton, P. M. Mechanisms of signalling and biased agonism in G protein-coupled receptors. *Nat Rev Mol Cell Biol* 19, 638–653 (2018).
4. Kumar, H., Kawai, T. & Akira, S. Pathogen recognition in the innate immune response. *Biochemical Journal* 420, 1–16 (2009).
5. Alberts, B. The Cell as a Collection of Protein Machines: Preparing the Next Generation of Molecular Biologists. *Cell* 92, 291–294 (1998).
6. Henzler-Wildman, K. & Kern, D. Dynamic personalities of proteins. *Nature* 450, 964–972 (2007).

7. Otsu, T., Ishii, K. & Tahara, T. Microsecond protein dynamics observed at the single-molecule level. *Nat Commun* 6, 7685 (2015).
8. Persson, E. & Halle, B. Nanosecond to Microsecond Protein Dynamics Probed by Magnetic Relaxation Dispersion of Buried Water Molecules. *J. Am. Chem. Soc.* 130, 1774–1787 (2008).
9. Ourmazd, A., Moffat, K. & Lattman, E. E. Structural biology is solved — now what? *Nat Methods* 19, 24–26 (2022).
10. Voss, J. M., Harder, O. F., Olshin, P. K., Drabbels, M. & Lorenz, U. J. Rapid melting and revitrification as an approach to microsecond time-resolved cryo-electron microscopy. *Chemical Physics Letters* 778, 138812 (2021).
11. Voss, J. M., Harder, O. F., Olshin, P. K., Drabbels, M. & Lorenz, U. J. Microsecond melting and revitrification of cryo samples. *Structural Dynamics* 8, 054302 (2021).
12. Harder, O. F., Voss, J. M., Olshin, P. K., Drabbels, M. & Lorenz, U. J. Microsecond melting and revitrification of cryo samples: protein structure and beam-induced motion. *Acta Crystallogr D Struct Biol* 78, (2022).
13. Klein-Seetharaman, J. Dynamics in Rhodopsin. *ChemBioChem* 3, 981–986 (2002).
14. Ellis-Davies, G. C. R. Caged compounds: photorelease technology for control of cellular chemistry and physiology. *Nat Methods* 4, 619–628 (2007).
15. Shigeri, Y., Tatsu, Y. & Yumoto, N. Synthesis and application of caged peptides and proteins. *Pharmacology & Therapeutics* 91, 85–92 (2001).
16. Bongiovanni, G., Harder, O. F., Drabbels, M. & Lorenz, U. J. Microsecond melting and revitrification of cryo samples with a correlative light-electron microscopy approach. *Frontiers in Molecular Biosciences* 9, (2022).

17. Olshin, P. K., Drabbels, M. & Lorenz, U. J. Characterization of a time-resolved electron microscope with a Schottky field emission gun. *Structural Dynamics* 7, 054304 (2020).
18. Punjani, A., Rubinstein, J. L., Fleet, D. J. & Brubaker, M. A. cryoSPARC: algorithms for rapid unsupervised cryo-EM structure determination. *Nat Methods* 14, 290–296 (2017).
19. Wu, M., Lander, G. C. & Herzik, M. A. Sub-2 Angstrom resolution structure determination using single-particle cryo-EM at 200 keV. *Journal of Structural Biology: X* 4, 100020 (2020).
20. Taylor, K. A. & Glaeser, R. M. Retrospective on the Early Development of Cryoelectron Microscopy of Macromolecules and a Prospective on Opportunities for the Future. *J Struct Biol* 163, 214–223 (2008).
21. Jamali, V. et al. Anomalous nanoparticle surface diffusion in LCTEM is revealed by deep learning-assisted analysis. *Proceedings of the National Academy of Sciences* 118, e2017616118 (2021).
22. Thorne, R. E. Hypothesis for a mechanism of beam-induced motion in cryo-electron microscopy. *IUCrJ* 7, 416–421 (2020).
23. Tan, Y. Z. et al. Addressing preferred specimen orientation in single-particle cryo-EM through tilting. *Nat Methods* 14, 793–796 (2017).
24. Penczek, P. A. & Frank, J. Resolution in Electron Tomography. in *Electron Tomography: Methods for Three-Dimensional Visualization of Structures in the Cell* (ed. Frank, J.) 307–330 (Springer, 2006). doi:10.1007/978-0-387-69008-7_11.

Chapter 5 - Microsecond melting and revitrification of cryo samples with a correlative light-electron microscopy approach^{***}

5.1 Introduction

Structure determination of proteins has made rapid progress in the last decade, particularly thanks to the resolution revolution in cryo-EM,¹⁻³ which now appears set to become the preferred method in structural biology,⁴ and the advent of machine learning approaches for protein structure prediction.^{5,6} At the same time, these advances put into relief our incomplete understanding of the dynamics and the function of proteins.⁷ In fact, it has been argued that understanding and ultimately predicting protein function is the next frontier in structural biology.⁸

Our incomplete understanding of protein function is to a large extent a consequence of the difficulty of observing proteins as they perform their task. This requires not only near-atomic spatial resolution, but also a time resolution that is sufficient to observe the domain motions that are frequently associated with the activity of a protein and that typically occur on short timescales of microsecond to milliseconds.^{7,9} Time-resolved cryo-EM has enabled observations of a range of processes.¹⁰⁻¹² Typically, dynamics are initiated by rapidly mixing two reactants and spraying them onto a specimen grid, which is then rapidly plunge frozen to trap short-lived intermediates.^{10,13-16} However, the time resolution of this method is fundamentally limited by the time required for plunge freezing, which is on the order of one millisecond,¹⁰ too slow to observe many relevant dynamics.

^{***} Reproduced from G. Bongiovanni, O.F.Harder, M. Drabbels and U.J.Lorenz, *Front. Mol. Biosc.* 2022, 9.
Authors Contributions: UL conceived the research. MD and UL designed the experiment, GB and OH performed the experiments. GB and MD analyzed data. GB and UL wrote the manuscript with contributions from all authors

We have recently introduced a novel approach to time-resolved cryo-EM that affords microsecond time resolution.¹⁷⁻¹⁹ This is notably fast enough to enable the observation many domain motions. We employ a laser beam to locally melt a cryo sample for several tens of microseconds, providing a well-defined time window during which the proteins can undergo conformational motions in liquid. A range of stimuli is conceivable that can be used to initiate specific dynamics. For example, caged compounds can be used to release ATP, ions, small peptides, or induce a pH jump.^{20,21} As the dynamics of the particles unfold, the heating laser is switched off, so that the sample rapidly cools and revitrifies, arresting the particles in their transient configurations.

We have demonstrated the viability of our approach and characterized the spatial and temporal resolution it affords. Proof-of-principle experiments confirm that once the sample is laser melted, particles can undergo motions in liquid and that upon revitrification, we can trap them in their transient states with microsecond time resolution.^{17,18} The success of a revitrification experiment can be assessed on the fly. In a successful experiment, the revitrified area in the center of the laser focus is surrounded by a region in which the sample has crystallized since its temperature has not exceeded the melting point. By adjusting the laser power to keep the diameter of the revitrified area constant, one can thus ensure that in each experiment, the sample undergoes the same temperature evolution.¹⁸ We have also demonstrated that the melting and revitrification process leaves the proteins intact.¹⁹ Near-atomic resolution reconstructions can be obtained from revitrified cryo samples, suggesting that the revitrification process does not fundamentally limit the obtainable spatial resolution

(manuscript in preparation; see also Ref. 22). With all crucial aspects of our method established, we have recently also begun to apply it to study the fast dynamics of a variety of systems.

By enabling atomic-resolution observations of the microsecond dynamics of proteins, our method promises to fundamentally advance our understanding of protein function. However, for our technique to achieve this goal, it is crucial to ensure that it is easily accessible, so that a large number of groups can adopt it. We currently perform our melting and revitrification experiments *in situ*, using a transmission electron microscope that we have modified for time-resolved experiments.²³ Setting up such an instrument, which few labs have at their disposal, presents a significant hurdle for the adoption of our technique. It is therefore desirable to develop a technically less involved variant.

Here, we present a simple implementation of our technique that uses an optical microscope to melt and revitrify cryo samples. Optical microscopes are already being used in many cryo-EM groups for correlative light and electron microscopy.²⁴ They are also simpler to operate, more cost-effective, as well as more straightforward to adapt to time-resolved experiments, all of which should facilitate their adoption.

5.2 Results

Figure 1A shows a photograph of the optical microscope (Leica DM6000 CFS) that we have adapted for melting and revitrification experiments (Methods). Bright field images are recorded with a CMOS camera placed on top of the instrument, with the sample illuminated with white light from below. The melting laser beam (532 nm, indicated in green) enters the

microscope head from the left and is reflected by a dichroic mirror that overlaps it with the optical axis and directs it at the sample. Microsecond laser pulses are obtained by chopping the output of a continuous laser with an acousto-optic modulator. The sample is held by a cryo stage for correlative microscopy (Linkam CMS 196), which maintains it at liquid nitrogen temperature and prevents the condensation of water vapor (Fig. 1B).

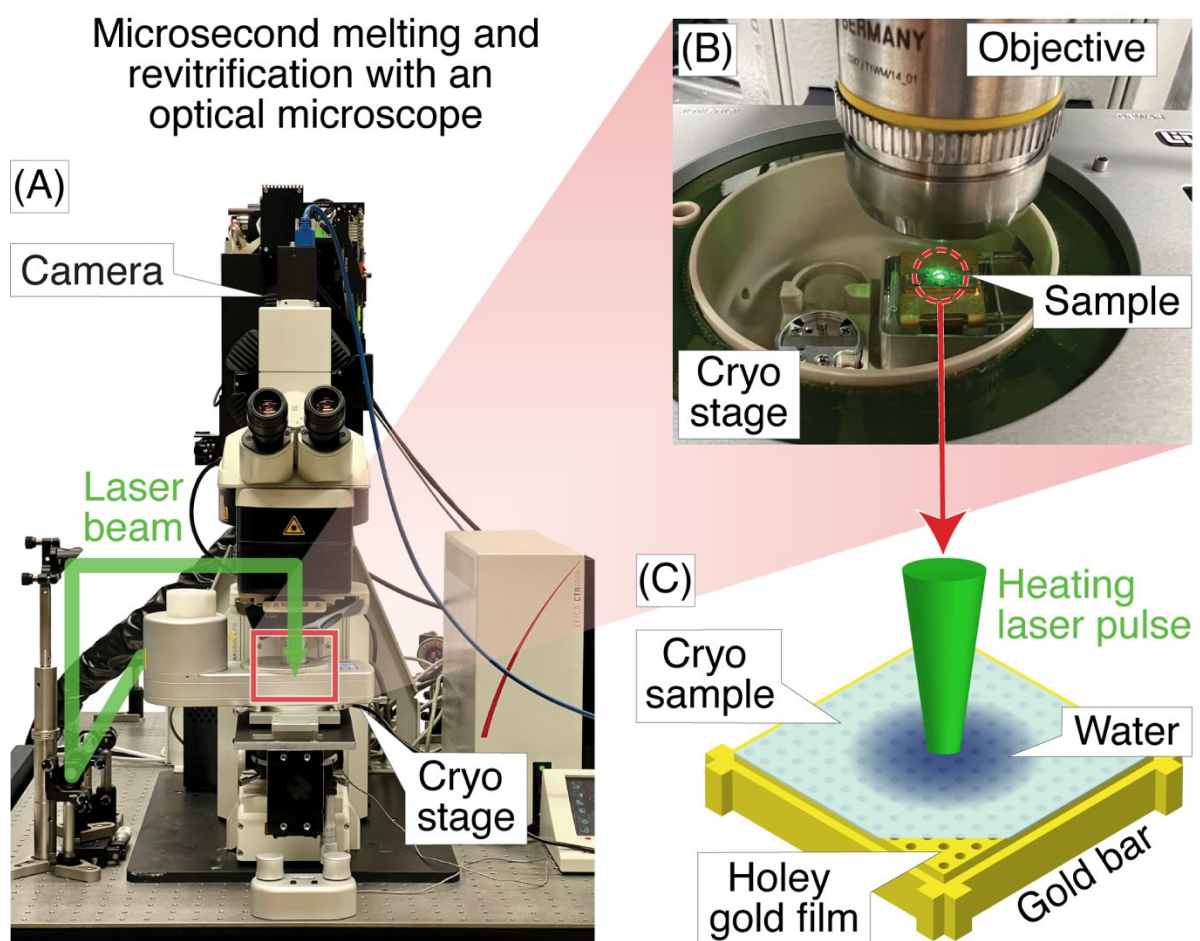


Figure 1. Melting and revitrification of cryo samples with an optical microscope.

(a) Photograph of the optical microscope and cryo stage. The laser beam (532 nm, indicated in green) enters the head of the microscope from the left and is focused onto the sample. (b) Detail of the cryo stage, with the laser beam striking the sample. (c) Illustration of the sample

geometry. A microsecond laser pulse is used to melt and revitrify the cryo sample in the center of a grid square.

The geometry of a melting and revitrification experiment is illustrated in Figure 1C. The cryo sample is prepared on an UltrAuFoil specimen support, which features a holey gold film on a 300 mesh gold grid. The heating laser is focused onto the center of a grid square (25 μm FWHM beam diameter in the sample plane). Under laser irradiation, the gold film rapidly heats up in the vicinity of the laser beam, causing the cryo sample to melt, so that the embedded particles can undergo unhindered motions in liquid phase. Within a few microseconds, the sample temperature stabilizes near room temperature.¹⁸ When the laser is switched off, the sample cools within just a few microseconds, as previously shown through experiments and simulations.¹⁷ At such high cooling rates, the sample revitrifies and traps the particles in their transient configurations in which they can subsequently be imaged.¹⁷ The short cooling time is a consequence of the fact that the laser heats the sample only locally, while its surroundings remain at cryogenic temperature, so that the heat is efficiently dissipated after the end of the laser pulse.

Figure 2 demonstrates that melting and revitrification experiments can be successfully performed with our optical microscope. Figure 2A shows an optical micrograph of a typical grid square of an apoferritin cryo sample. Melting and revitrification with a 40 μs laser pulse (45 mW) barely causes the image contrast to change. However, a characteristic signature of successful melting and revitrification is readily apparent in a difference image (Figure 2B), which is obtained by subtracting a micrograph recorded before revitrification from one

recorded after. The revitrified area in the center of the grid square is surrounded by a thin, dark ring and features a dark patch in its center.

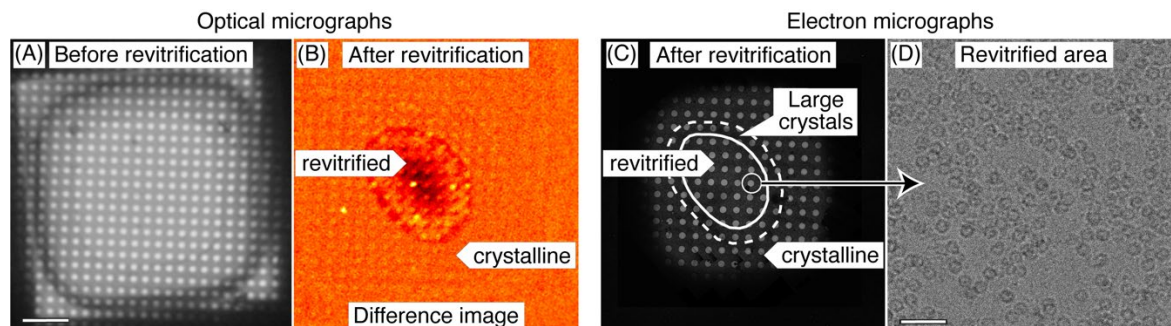


Figure 2. Correlative light-electron microscopy of a cryo sample that was revitrified in the optical microscope. (a) Optical micrograph of a typical grid square of an apoferritin cryo sample. (b) Difference image of the sample after melting and revitrification with a 40 μ s, obtained by subtracting the image before revitrification from one recorded after. The revitrified area in the center of the grid square features a thin, dark outline that arises from the formation of crystals in the surrounding area. A dark patch in the center indicates thinning of the sample due to evaporation. (c) An electron micrograph of the same area confirms the interpretation of the image contrast in (b). The outline of the revitrified area is marked with a solid line. A dashed line indicates the region in which the formation of large crystals is observed. (d) Micrograph recorded in the area circled in (c), showing intact apoferritin particles. Scale bars, 10 μ m in (a) and 40 nm in (d).

An electron micrograph of the same area (Figure 2C) confirms the success of the revitrification experiment and elucidates the nature of the features visible in the difference image. The micrograph shows that the sample has melted and revitrified in the vicinity of the laser focus,

while it has crystallized in the surrounding areas (details in Supplementary Figure S2 in Appendix II). The outline of the revitrified area (solid line) closely agrees with the inner boundary of the thin, dark ring that is visible in the difference image of Figure 2B. This ring seems to originate from the large ice crystals that have formed at the border of the revitrified area (dashed line, see also Supplementary Figure S2 in Appendix II for a magnified view), as previously observed.¹⁸ The dark spot visible in the center of the revitrified area does not seem to correspond to any feature in the electron micrograph. We propose that it results from the thinning of the sample due to evaporation that occurs during laser heating and which is most pronounced in the center of the laser focus, where the sample reaches the highest temperature.¹⁸ This interpretation is supported by the fact that the dark spot becomes most pronounced when the sample is evaporated entirely in the center of the grid square (Supplementary Figure S1D in Appendix II). Note that in the electron micrograph of Figure 2C, fewer holes are visible than in the optical micrograph of Figure 2A. This is because areas with thick ice close to the grid bars do not transmit electrons, whereas they are transparent in the optical micrograph.

We conclude that difference images can be used to assess the success of a melting and revitrification experiment on the fly, which can be inferred from the presence of a thin, dark ring that surrounds a dark spot, which marks the center of the laser focus. As illustrated in Supplementary Figure S1 (Appendix II), these features are absent if the laser power is too low to induce melting and revitrification. It is also straightforward to detect if the laser power is too high, so that the sample is evaporated entirely in the vicinity of the laser focus. In this case, a pronounced dark spot results in the center of the grid square, with the holes of the gold film appearing bright (Supplementary Figure S1C, D in Appendix II). In order to ensure that the

sample undergoes a reproducible temperature evolution, the diameter of the revitrified area should be kept constant.¹⁸ This can be achieved by monitoring the diameter of the dark ring in the difference images and adjusting the laser power accordingly.

Melting and revitrification with our optical microscope leaves the proteins intact, as evidenced by an electron micrograph collected from a hole within the revitrified area (Figure 2D). Single-particle reconstructions corroborate this result and show that revitrification does not alter the structure of the apoferritin particles. We revitrified 17 areas of a fresh cryo sample in the optical microscope and imaged them on a Titan Krios G4. A comparable number of images were collected of areas that had not been exposed to the laser beam. The reconstructions from the conventional and revitrified areas feature a resolution of 1.47 Å and 1.63 Å, respectively (Figure 3A). At this resolution, side chain densities are clearly resolved, and individual water molecules can be distinguished (Figure 3B). Within the near-atomic resolution of these reconstructions, the structure of the particles in the conventional and revitrified areas is indistinguishable. We conclude that revitrification in our optical microscope does not alter the protein structure.

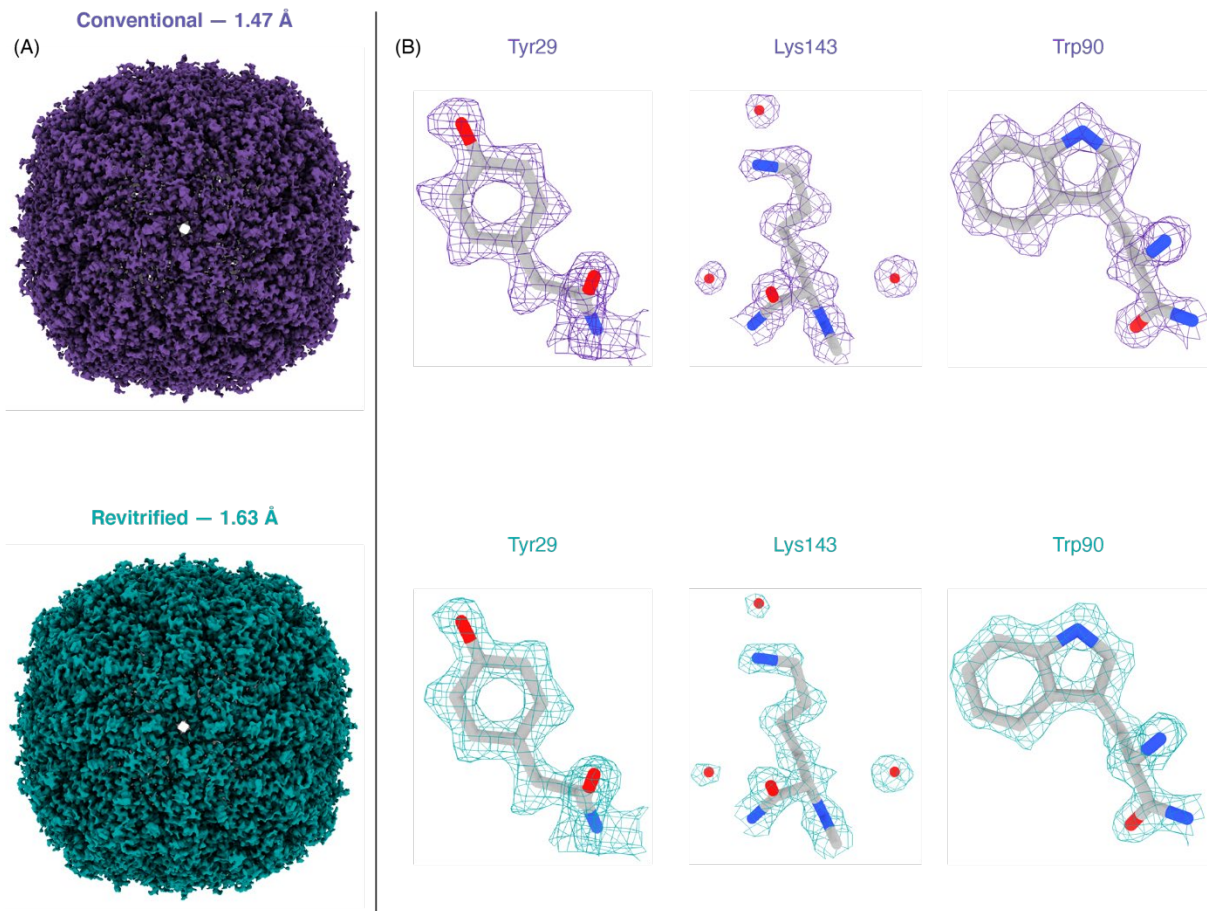


Figure 3. Reconstructions of apoferritin from conventional and revitrified sample areas. Within the spatial resolution of the reconstruction, the structure of the particles is indistinguishable. (a) Reconstructions from conventional (purple, 1.47 Å resolution) and from revitrified areas (green, 1.62 Å). (b) Details of the reconstructions, showing that the side chain densities are clearly resolved and that single water molecules are visible. A molecular model of apoferritin (PDB 6v21, Ref 25) has been placed into the density through rigid body fitting.

5.3 Conclusions

In summary, we have demonstrated that microsecond time-resolved cryo-EM experiments can be performed with a correlative light-electron microscopy approach. The success of a melting

and revitrification experiment can be assessed on the fly by monitoring characteristic signatures in an optical difference image. We have also shown that revitrification in our optical microscope setup preserves the protein structure, allowing us to obtain near-atomic resolution reconstructions. This suggests that the revitrification process does not fundamentally limit the obtainable spatial resolution.

Revitrification with an optical microscope is in several respects complementary to the *in situ* approach we have previously described,¹⁷⁻¹⁹ with each approach offering distinct advantages. It is usually more straightforward to determine the diameter of the revitrified area in an *in situ* experiment, since the surrounding crystalline region offers a strong contrast in an electron microscope, whereas it may be more difficult to detect in optical difference images if the crystallites are too small. It should however be possible to obtain a better contrast by using different optical imaging modes. *In situ* experiments also offer the advantage that the behavior of the particles during revitrification can be assessed immediately, either by visual inspection or from an on-the-fly reconstruction, so that the laser parameters can be adjusted as needed. Moreover, *in situ* experiments will likely be indispensable to further characterize and advance the experimental approach. For example, we have previously been able to infer that cryo samples partially crystallize during laser melting.¹⁸ To better understand the phase behavior of cryo samples during rapid heating, we have therefore embarked on time-resolved *in situ* experiments that employ intense high-brightness electron pulses of microsecond duration²⁶ to capture the structural evolution of the cryo sample. Finally, controlling the plateau temperature that the sample reaches during the laser pulse is somewhat easier for *in situ* experiments, where evaporative cooling in the vacuum of the microscope can be used to provide a negative feedback that limits the sample temperature at high laser powers.¹⁸ In

revitrification experiments with the optical microscope, this feedback effect is likely much reduced due to the lower evaporation rate of water at ambient pressure.²⁷

The correlative revitrification approach described here offers the significant advantage that its implementation is technically less involved, which we hope will encourage other research groups to use our technique and explore its potential for elucidating the fast dynamics of a variety of systems. Once suitable experimental conditions for a time-resolved experiment have been established, samples for high-resolution imaging can be most conveniently revitrified with the optical microscope. Because of the simplicity of the setup, the experimental workflow involved can also be easily automated, which we have begun to do. Imaging the sample with the optical microscope also does not damage the particles, in contrast to *in situ* experiments with the electron microscope, where the sample has to be exposed to a small electron dose in order to locate and center areas for revitrification at low magnification. This is significant because the exposure to a dose of only a few electrons/Å² induces so much fragmentation that the proteins will completely unravel once the sample is melted.^{17,18} It is therefore sensible to avoid exposure even to the small dose required for low-magnification imaging, which may potentially cause some proteins to lose their function even though no structural damage is evident.²⁸

Using an optical microscope for revitrification may also enable new types of experiments. The simple optical layout of the instrument makes it straightforward to combine different laser beams and wavelengths, which may be used to trigger different dynamics or monitor the revitrification process. For example, it would be straightforward to use a separate UV laser beam to release a caged compound in selected grid squares, such as caged ATP, ions, or even

peptides.²⁰⁻²¹ With the sample still in its vitreous state, the proteins are unable to react to this change in their chemical environment. However, once the sample is laser melted, the compound becomes available to initiate conformational dynamics.¹⁷ By releasing different quantities of the caged compound in different grid squares, it would then be possible to study how the concentration of the compound affects the dynamics, with all experiments conducted on the very same specimen grid, thus guaranteeing the most reproducible conditions. It will also become possible to combine revitrification experiments with other types of correlative microscopy. It is even conceivable to perform experiments on entire cells, as long the heat transfer in the sample can be engineered to be fast enough, so that vitrification can be achieved after the end of the laser pulse. Finally, our optical microscope setup may also provide a practical approach to improve the quality of conventional cryo samples. Melting and revitrification can be used to turn some crystalline areas vitreous or reduce the ice thickness through evaporation. It may also be possible to reduce beam induced specimen motion by releasing stress in the vitreous ice film through irradiation with a sequence of laser pulses.¹⁹

5.4 Methods

Cryo samples were prepared on UltrAuFoil R1.2/1.3 300 mesh grids (Quantifoil), which were rendered hydrophilic through plasma cleaning for 1 min (Tedpella “Easy glow” discharge system, negative polarity with a plasma current of 0.8 mA and a residual air pressure of 0.2 mbar). A volume of 3 μ l of the sample solution (mouse heavy chain apoferritin, 8.5 mg/ml in 20 mM HEPES buffer with 300 mM sodium chloride at pH 7.5) was applied to the specimen grid, which was then plunge-frozen with a Vitrobot Mark IV (Thermo Fisher Scientific, 3 s

blotting time, 95% relative humidity at a temperature of 10 °C). The grids were screened on a JEOL 2200FS (Ref. 23) before revitrifying them in the optical microscope.

Revitrification experiments were performed with a modified Leica DM6000 CFS optical microscope equipped with a Linkam CMS 196 cryo stage (Figure 1A). Microsecond laser pulses for melting and revitrification are obtained by chopping the output of a 532 nm continuous wave laser (Laser Quantum, Ventus 532) with an acousto-optic modulator (AA-optoelectronic). As shown in Figure 1A, the laser beam enters the microscope head from the left and is reflected by a dichroic mirror that overlaps it with the optical axis. The beam is focused to a spot size of 25 μm FWHM in the sample plane, as determined from an image of the beam recorded with a CCD camera placed in the sample location. Optical bright field images are recorded with a Teledyne FLIR Grasshopper3 camera. Difference images for assessing the success of a revitrification experiment (Figure 2B) were obtained by subtracting an image of the sample before laser irradiation from one recorded after. Both images were acquired as averages of 15 exposures each (1 s), which were aligned using phase correlation-based image registration.²⁹

The electron micrographs of Figure 2C, D were recorded on a JEOL 2200FS. (Ref. 23) The image in Figure 2C was obtained by stitching together several micrographs acquired at higher magnification, in which the crystalline areas can be more readily identified. Micrographs for single-particle reconstructions (Figure 3) were acquired with a Titan Krios G4 (Thermo Fisher Scientific) operated at 300 kV accelerating voltage and using a 10 eV slit width (Selectris X energy filter). The micrographs were recorded with a Falcon 4 camera, with an exposure time of about 2.5 s and a total dose of 50 electrons \AA^{-2} . The pixel size was 0.455 \AA , and defocus values were in the range of 0.9–1 μm .

Single-particle reconstructions were performed in CryoSPARC 3.3.2 (Ref. 30), as detailed in Supplementary Material 1. Briefly, the conventional (revitrified) apoferritin dataset comprises 10145 (12047) images. Patch motion correction and CTF estimation yielded 6242 (3671) images with a resolution better than 6 Å, which were kept for further processing. Using template-based particle picking, 2937383 (1714924) particles were identified. Following two rounds of 2D classification, 534606 (212377) particles were retained for *ab initio* reconstruction (*C1* symmetry), followed by heterogeneous refinement (*O* symmetry) using three classes. After re-extraction, the 447704 (95786) particles found in the most populated classes were then used for homogeneous refinement (*O* symmetry) to give a final map with a resolution of 1.47 Å (1.63 Å).

Reconstructions were visualized with Chimera X (Ref. 31), using contour levels of 0.077 and 0.24 in Figure 3A and Figure 3B, respectively. The molecular model displayed in Figure 3B (PDB 6v21, Ref. 25) was placed into the map using rigid body fitting.

5.5 References

1. Kühlbrandt, W. The Resolution Revolution. *Science* **343**, 1443–1444 (2014).
2. Nakane, T. *et al.* Single-particle cryo-EM at atomic resolution. *Nature* **587**, 152–156 (2020).
3. Yip, K. M., Fischer, N., Paknia, E., Chari, A. & Stark, H. Atomic-resolution protein structure determination by cryo-EM. *Nature* **587**, 157–161 (2020).
4. Hand, E. Cheap shots. *Science* **367**, 354–358 (2020).

5. Jumper, J. *et al.* Highly accurate protein structure prediction with AlphaFold. *Nature* **596**, 583–589 (2021).
6. Baek, M. *et al.* Accurate prediction of protein structures and interactions using a three-track neural network. *Science* **373**, 871–876 (2021).
7. Henzler-Wildman, K. & Kern, D. Dynamic personalities of proteins. *Nature* **450**, 964–972 (2007).
8. Ourmazd, A., Moffat, K. & Lattman, E. E. Structural biology is solved — now what? *Nature Methods* **19**, 24–26 (2022).
9. Boehr, D. D., Dyson, H. J. & Wright, P. E. An NMR Perspective on Enzyme Dynamics. *Chem. Rev.* **106**, 3055–3079 (2006).
10. Frank, J. Time-resolved cryo-electron microscopy: Recent progress. *Journal of Structural Biology* **200**, 303–306 (2017).
11. Fu, Z. *et al.* The structural basis for release-factor activation during translation termination revealed by time-resolved cryogenic electron microscopy. *Nat Commun* **10**, 2579 (2019).
12. Carbone, C. E. *et al.* Time-resolved cryo-EM visualizes ribosomal translocation with EF-G and GTP. *Nat Commun* **12**, 7236 (2021).
13. Berriman, J. & Unwin, N. Analysis of transient structures by cryo-microscopy combined with rapid mixing of spray droplets. *Ultramicroscopy* **56**, 241–252 (1994).
14. Kontziampasis, D. *et al.* A cryo-EM grid preparation device for time-resolved structural studies. *IUCr* **6**, 1024–1031 (2019).
15. Dandey, V. P. *et al.* Time-resolved cryoEM using Spotiton. *Nat Methods* **17**, 897–900 (2020).

16. Klebl, D. P. *et al.* Sample deposition onto cryo-EM grids: from sprays to jets and back. *Acta Cryst D* **76**, 340–349 (2020).
17. Voss, J. M., Harder, O. F., Olshin, P. K., Drabbels, M. & Lorenz, U. J. Rapid melting and revitrification as an approach to microsecond time-resolved cryo-electron microscopy. *Chemical Physics Letters* **778**, 138812 (2021).
18. Voss, J. M., Harder, O. F., Olshin, P. K., Drabbels, M. & Lorenz, U. J. Microsecond melting and revitrification of cryo samples. *Structural Dynamics* **8**, 054302 (2021).
19. Harder, O. F., Voss, J. M., Olshin, P. K., Drabbels, M. & Lorenz, U. J. Microsecond melting and revitrification of cryo samples: protein structure and beam-induced motion. *Acta Crystallogr D Struct Biol* **78**, (2022).
20. Shigeri, Y., Tatsu, Y. & Yumoto, N. Synthesis and application of caged peptides and proteins. *Pharmacology & Therapeutics* **91**, 85–92 (2001).
21. Ellis-Davies, G. C. R. Caged compounds: photorelease technology for control of cellular chemistry and physiology. *Nat Methods* **4**, 619–628 (2007).
22. Lorenz, U. J. Towards Microsecond Time-Resolved Cryo-Electron Microscopy. (2022).
23. Olshin, P. K., Drabbels, M. & Lorenz, U. J. Characterization of a time-resolved electron microscope with a Schottky field emission gun. *Structural Dynamics* **7**, 054304 (2020).
24. de Boer, P., Hoogenboom, J. P. & Giepmans, B. N. G. Correlated light and electron microscopy: ultrastructure lights up! *Nat Methods* **12**, 503–513 (2015).
25. Wu, M., Lander, G. C. & Herzik, M. A. Sub-2 Angstrom resolution structure determination using single-particle cryo-EM at 200 keV. *Journal of Structural Biology: X* **4**, 100020 (2020).

26. Olshin, P. K., Bongiovanni, G., Drabbels, M. & Lorenz, U. J. Atomic-Resolution Imaging of Fast Nanoscale Dynamics with Bright Microsecond Electron Pulses. *Nano Lett.* **21**, 612–618 (2021).
27. Marek, R. & Straub, J. Analysis of the evaporation coefficient and the condensation coefficient of water. *Int. J. Heat Mass Transfer* **15** (2001) doi:10.1016/S0017-9310(00)00086-7.
28. Glaeser, R. M. Specimen Behavior in the Electron Beam. in *Methods in Enzymology* vol. 579 19–50 (Elsevier, 2016).
29. Reddy, B. S. & Chatterji, B. N. An FFT-based technique for translation, rotation, and scale-invariant image registration. *IEEE Trans. on Image Process.* **5**, 1266–1271 (1996).
30. Punjani, A., Rubinstein, J. L., Fleet, D. J. & Brubaker, M. A. cryoSPARC: algorithms for rapid unsupervised cryo-EM structure determination. *Nat Methods* **14**, 290–296 (2017).
31. Goddard, T. D. *et al.* UCSF ChimeraX: Meeting modern challenges in visualization and analysis: UCSF ChimeraX Visualization System. *Protein Science* **27**, 14–25 (2018).

Chapter 6 – Conclusions and outlook

This thesis covers the development of new tools to image microsecond dynamics with near-atomic spatial resolution.

In Chapter 2 a novel approach to temporarily boost the emission current of a Schottky emitter is presented. We use a laser pulse to briefly heat up the tip of the Schottky filament, which as a result reaches an estimated temperature of over 2500 K. While the high temperature would not be sustainable for prolonged periods, we show that we avoid damaging the emitter thanks to the short duration of the heating pulse. The emission current is, at the highest temperature reached during the laser pulse, 3.7 times higher than what the filament delivers in standard operating conditions.

Chapter 3 details a method to generate bright microsecond electron pulses by combining an electrostatic beam blanker with the laser setup described in the previous chapter. The brightness of such pulses is 1.7 times higher than that of the Schottky emitter operated in standard conditions. The chapter also shows potential applications of this pulsed setup. Microsecond pulses can capture atomic-resolution micrographs in the presence of large amounts of drift, significantly outperforming the continuous electron beam. In addition, they can be used to image irreversible dynamics with atomic resolution.

Chapter 4 details a new approach to time-resolved cryo-electron microscopy, which involves locally melting a cryo sample with a laser beam. While the temporal resolution of conventional time-resolved cryo-EM is limited by the cooling time of an entire grid, in our experiments the specimen is warmed up only locally. As a result, the cooling rates are three orders of magnitude higher than what is achieved with conventional plunge-freezing, which brings the same improvement to the temporal resolution of time-resolved cryo-EM.

The chapter demonstrates the suitability of the technique to image protein dynamics by showing that it is possible to obtain a near-atomic resolution reconstruction from revitrified sample areas, and the result is undistinguishable from a map of the same protein recorded on a conventional sample. In addition, we show that the rapid melting and revitrification process reorients the particles, making the distribution of projection angles more homogeneous.

Chapter 5 explains how the melting and revitrification experiments can be carried out using an optical microscope instead of a modified electron microscope. The simplified setup should encourage the adoption of the technique by other research groups and will hopefully boost the development of microsecond time-resolved cryo-EM. In addition, this new method provides some advantages compared to *in situ* irradiation in an electron microscope. For example, because the outcome of the experiment can be assessed without imaging with an electron beam, protein damage prior to revitrification is avoided.

The methods described in this thesis enable near-atomic resolution imaging of microsecond dynamics. While research groups in the field of time-resolved electron microscopy keep pushing the boundaries of the temporal resolution,¹⁻⁴ atomic-resolution imaging of irreversible nanoscale processes has remained elusive.

Time-resolved studies with high spatial resolution have applications in fields ranging from materials science to structural biology. Microsecond time-resolved electron microscopy can be employed to directly observe dynamics of ferroelectric, ferromagnetic or ferroelastic domains or the propagation of elastic deformations in crystals;⁵ they can shed a light on the folding mechanism of biomolecules⁶ and reveal protein conformational dynamics.⁷

Work is currently underway in our research group to employ the microsecond electron pulses to elucidate the structure and the crystallization dynamics of supercooled water.⁸ In parallel,

the rapid melting and revitrification method is enabling the observation structural dynamics in proteins and viral machines.

A possible line of research for the future is the improvement of the temporal resolution of our electron pulses.

Their duration is determined by the amount of time it takes to extract enough electrons for single- or multi-shot imaging without significantly affecting the coherence properties of the beam. The number of electrons required depends, among other factors, on the detective quantum efficiency of the electron camera, and improvements in electron detectors could significantly reduce the dose necessary to form images. Currently, modern direct detectors represent a substantial improvement in detective quantum efficiency compared to scintillator-based cameras, such as the one in use in our laboratory (TVIPS XF416).⁹ For example, using a Gatan K2 camera in counting mode it appears it would be possible to reduce the acquisition time by a factor 3 to 4, which would enable atomic-resolution imaging with pulses of about 1.5 μs duration.⁹ However, at present, direct detectors are unable to function in counting mode under the typical dose levels required for single-shot imaging.

Considerable improvements could also be made with different gun designs. Compared to the emitter described in this work, commercial high-brightness Schottky electron guns (XFEGs) with the same beam emittance would be able to provide significantly higher currents. This property renders them ideal sources for the generation of highly coherent and intense pulses, but the ultimate limit on the minimum pulse duration depends on their ability to deliver extreme currents for brief periods of time.

Even higher instantaneous brightness could be achieved pulsing the extraction voltage. A rapid spike in extraction voltage would lower the surface barrier, causing a temporary increase in

the emission current.¹⁰ At the same time, electrons extracted during the voltage spike would experience a strong electric field, rapidly advancing towards the accelerator. This would reduce the time they spend in the gun lens area, where they strongly interact and reduce the beam quality.¹¹

Future work in the field of microsecond time-resolved cryo-EM involves the direct observation of microsecond protein dynamics. While this will initially entail proof-of-principle experiments, a suitable long-term target of time-resolved studies might be G protein-coupled receptors (GPCRs). This highly dynamic class of proteins is responsible for the detection of a wide range of chemicals surrounding the cell and for the initiation of the corresponding signaling pathways.¹² For this reason, GPCRs are the target of roughly 35% of the drugs on the market.¹³ Time-resolved experiments could shed a light on the complex conformational changes required to transmit signals. In addition, they could also be a powerful tool to understand the interactions between a drug candidate and the corresponding receptor, including the mechanisms of molecular recognition and ligand-receptor stability.¹⁴

In the pursuit of observing protein dynamics, the method can be further advanced by extending the range of observable conformational changes. For example, alternatives to the light-trigger release of caged compounds could be developed to study the interaction between proteins and light-sensitive molecules, such as nucleic acids. Such methods would also be useful if the caged version of the reactant of interest is not readily available.

Perhaps more importantly, the sample rapidly evaporates upon melting, setting a limit on the duration of the dynamics we can observe. The exact value of the evaporation coefficient of water has been hotly debated for decades, and there is no definitive answer that would allow us to calculate the maximum pulse duration in our setups.¹⁵ However, our observations

indicate that cryo samples fully evaporate after a few tens of microseconds, perhaps even less in the vacuum of the electron microscope. Many relevant conformational dynamics are not completed in such short time interval: for example, the timescale of membrane proteins dynamics is associated to the RC constant of the cell membrane, which is on the order of a few milliseconds.^{16–20}

Because the evaporation rate depends exponentially on the temperature of water, the time window could be extended by simply heating the sample barely above the melting point. However, the lower temperature would also affect the reaction rate, in non-trivial ways.²¹

Thicker samples would delay the complete evaporation of the irradiated area but are also more difficult to screen and control. To solve this issue, we have recently begun to explore the possibility of depositing water on a cryo sample with a custom-made apparatus. After screening, samples of good quality could be rendered thicker by depositing controlled amounts of water, significantly extending the range of timescales which can be probed with our method.

6.1 References

1. Hassan, M. T. Attomicroscopy: from femtosecond to attosecond electron microscopy. *J. Phys. B: At. Mol. Opt. Phys.* 51, 032005 (2018).
2. Feist, A. *et al.* Quantum coherent optical phase modulation in an ultrafast transmission electron microscope. *Nature* 521, 200–203 (2015).
3. Morimoto, Y. & Baum, P. Diffraction and microscopy with attosecond electron pulse trains. *Nature Phys* 14, 252–256 (2018).

4. Ryabov, A., Thurner, J. W., Nabben, D., Tsarev, M. V. & Baum, P. Attosecond metrology in a continuous-beam transmission electron microscope. *Science Advances* 6, eabb1393 (2020).
5. Gorfman, S. Sub-microsecond X-ray crystallography: techniques, challenges, and applications for materials science. *Crystallography Reviews* 20, 210–232 (2014).
6. Visser, E. W. A., Horáček, M. & Zijlstra, P. Plasmon Rulers as a Probe for Real-Time Microsecond Conformational Dynamics of Single Molecules. *Nano Lett.* 18, 7927–7934 (2018).
7. Henzler-Wildman, K. & Kern, D. Dynamic personalities of proteins. *Nature* 450, 964–972 (2007).
8. Krüger, C. R., Mowry, N. J., Bongiovanni, G., Drabbels, M. & Lorenz, U. J. Electron Diffraction of Water in No Man's Land. Preprint at <https://doi.org/10.48550/arXiv.2211.04419> (2022).
9. Ruskin, R. S., Yu, Z. & Grigorieff, N. Quantitative characterization of electron detectors for transmission electron microscopy. *J Struct Biol* 184, 10.1016/j.jsb.2013.10.016 (2013).
10. Orloff, J. *Handbook of Charged Particle Optics*. (CRC Press, 2017).
11. van Veen, A. H. V., Hagen, C. W., Barth, J. E. & Kruit, P. Reduced brightness of the ZrO/W Schottky electron emitter. *Journal of Vacuum Science & Technology B: Microelectronics and Nanometer Structures Processing, Measurement, and Phenomena* 19, 2038–2044 (2001).
12. Latorraca, N. R., Venkatakrisnan, A. J. & Dror, R. O. GPCR Dynamics: Structures in Motion. *Chem. Rev.* 117, 139–155 (2017).
13. Sriram, K. & Insel, P. A. G Protein-Coupled Receptors as Targets for Approved Drugs: How Many Targets and How Many Drugs? *Mol Pharmacol* 93, 251–258 (2018).

14. Guo, D., Heitman, L. H. & IJzerman, A. P. Kinetic Aspects of the Interaction between Ligand and G Protein-Coupled Receptor: The Case of the Adenosine Receptors. *Chem. Rev.* 117, 38–66 (2017).
15. Eames, I. W., Marr, N. J. & Sabir, H. The evaporation coefficient of water: a review. *International Journal of Heat and Mass Transfer* 40, 2963–2973 (1997).
16. Karpuk, N. & Vorobyov, V. Spike sequences and mean firing rate in rat neocortical neurons in vitro. *Brain Research* 973, 16–30 (2003).
17. Rall, W. Time Constants and Electrotonic Length of Membrane Cylinders and Neurons. *Biophys J* 9, 1483–1508 (1969).
18. Scorza, C. A. *et al.* Morphological and electrophysiological properties of pyramidal-like neurons in the stratum oriens of Cornu ammonis 1 and Cornu ammonis 2 area of Proechimys. *Neuroscience* 177, 252–268 (2011).
19. Isokawa, M. Membrane time constant as a tool to assess cell degeneration. *Brain Research Protocols* 1, 114–116 (1997).
20. Orädd, F. & Andersson, M. Tracking Membrane Protein Dynamics in Real Time. *J Membrane Biol* 254, 51–64 (2021).
21. Karplus, M. Aspects of Protein Reaction Dynamics: Deviations from Simple Behavior. *J. Phys. Chem. B* 104, 11–27 (2000).

Appendix I - Supporting information for Chapter 3

A1.1 Dose fractionated imaging with microsecond electron pulses in the presence of beam-induced drift

In Fig. 2 of the main text, we demonstrate drift-corrected imaging with microsecond electron pulses in the presence of large amounts of drift that we induce by irradiating the sample with a laser beam. Here, we show that imaging with microsecond electron pulses offers the same advantage if the drift is not induced by an external stimulus, but by the exposure of the sample to the electron beam.

Supplementary Fig. 3a,c shows drift-corrected images of an ensemble of gold nanoparticles on lacey carbon in an area of the sample that is particularly sensitive to beam-induced drift, with the micrograph in (a) acquired with continuous beam and that in (c) with pulsed illumination (600 μ s pulses). Both images were recorded as movies of 25 frames (1025 ms total exposure time, same total dose) and drift corrected with cisTEM.¹ A diffractogram of the area marked with a black rectangle in the micrograph recorded with electron pulses reveals a number of reflections originating from the gold nanoparticles that are much weaker or even absent in the micrograph acquired with a continuous beam. Pulsed illumination therefore better preserves high-resolution information, even though the sample experiences more beam-induced drift, as the reconstructed drift paths reveal (Supplementary Fig. 3b,d).

A1.2 Estimation of the energy spread

The energy spread for our source in both standard and pulsed conditions can be estimated using the Fermi-Dirac distribution. Following Brosengeest's analysis,² we calculate the

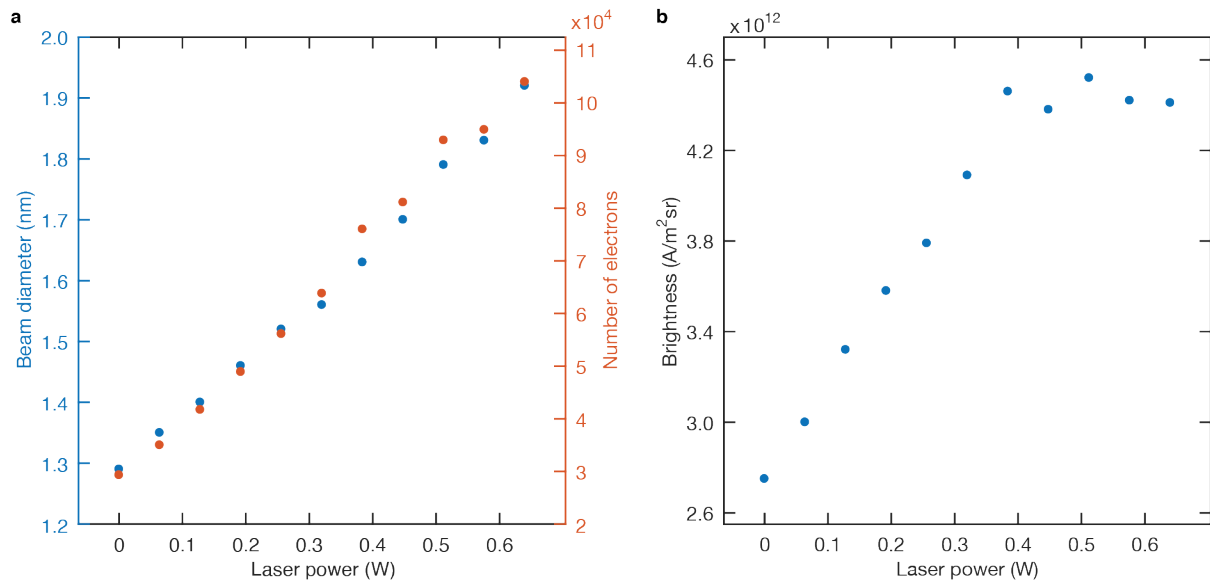
emission probability of electrons as a function of their energy, taking into account quantum tunnelling through the energy barrier, which is significant under the high extraction fields of our Schottky emitter.

We also take into account the impact of the temperature on the work function. We use Richardson's law to calculate the energy barrier at 2400 K, based on the observed increase in probe current in our experiments. We estimate a rise of about 0.6 eV.

Using a Fermi energy of 11 eV and a work function at 1800 K of 2.9 eV, which is lowered by 0.6 eV under an applied electric field of 1 V/nm^2 , we obtain an energy spread of 0.42 eV (FWHM) for the standard Schottky emitter and 0.46 eV (FWHM) for our pulsed source.

We note that these values are somewhat lower than typical measurements for similar sources. However, our calculation does not include electron-electron repulsion and other non-idealities, which should increase the energy spread by roughly a factor of two.

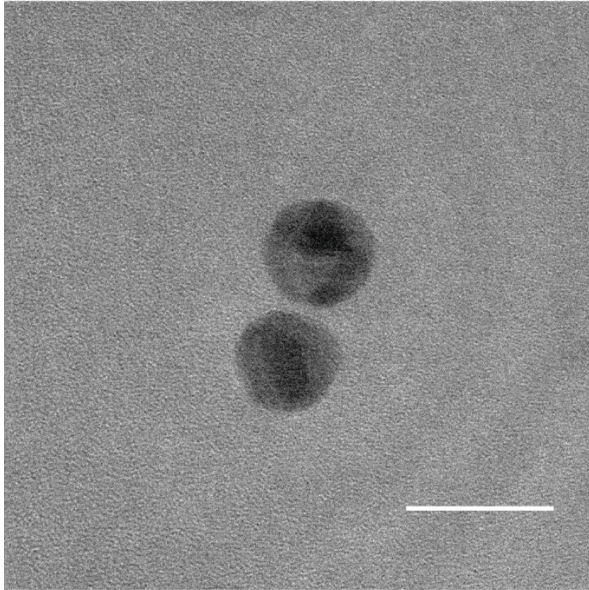
A1.3 Supplementary Figures



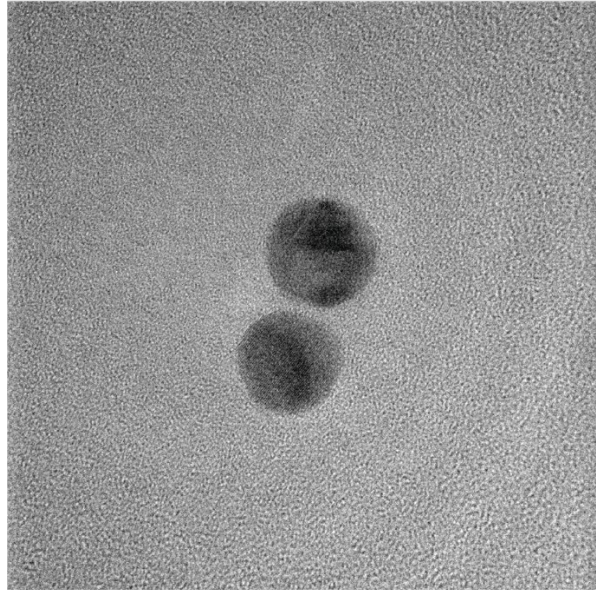
Supplementary Figure 1. Determination of the brightness of the laser-boosted electron pulses.

(a) Beam diameter (blue dots) and number of electrons in a 10 μs pulse (red dots) as a function of boost laser power. (b) Instantaneous brightness of the electron pulses as a function of laser power.

a Continuous electron beam



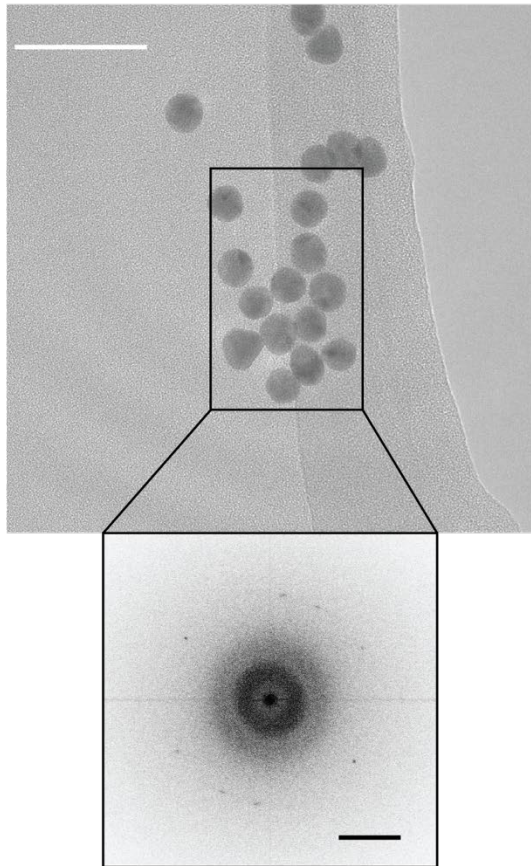
b Electron pulses (480 μ s)



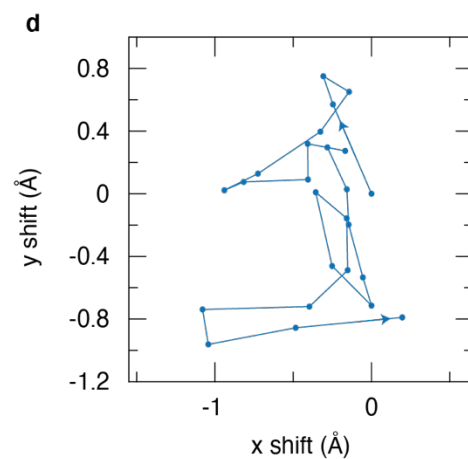
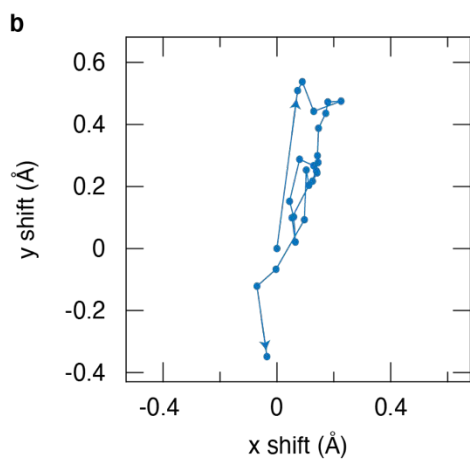
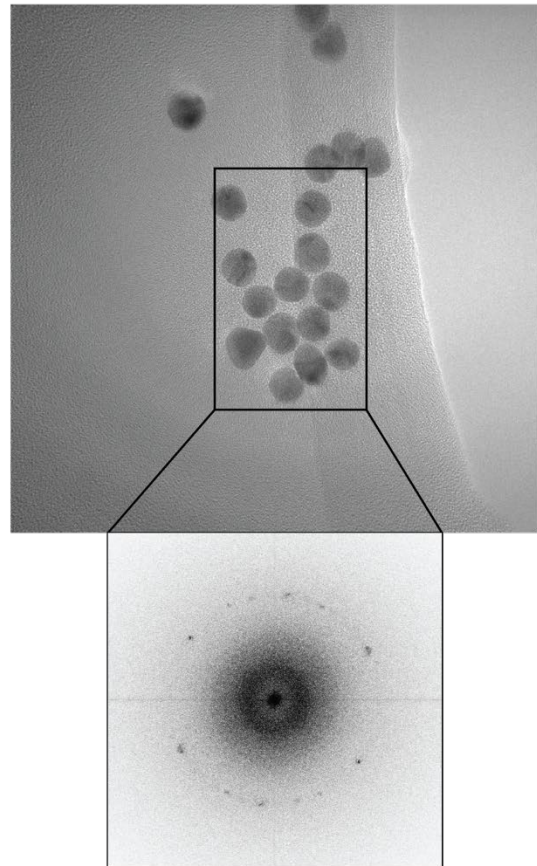
Supplementary Figure 2. Drift-corrected imaging in presence of large amounts of drift. (a, b) Full frame micrographs from which the images in Fig. 2a,c of the main text were taken. Scale bar, 20 nm.

Drift-corrected imaging with microsecond electron pulses
Electron beam-induced drift

a Continuous electron beam

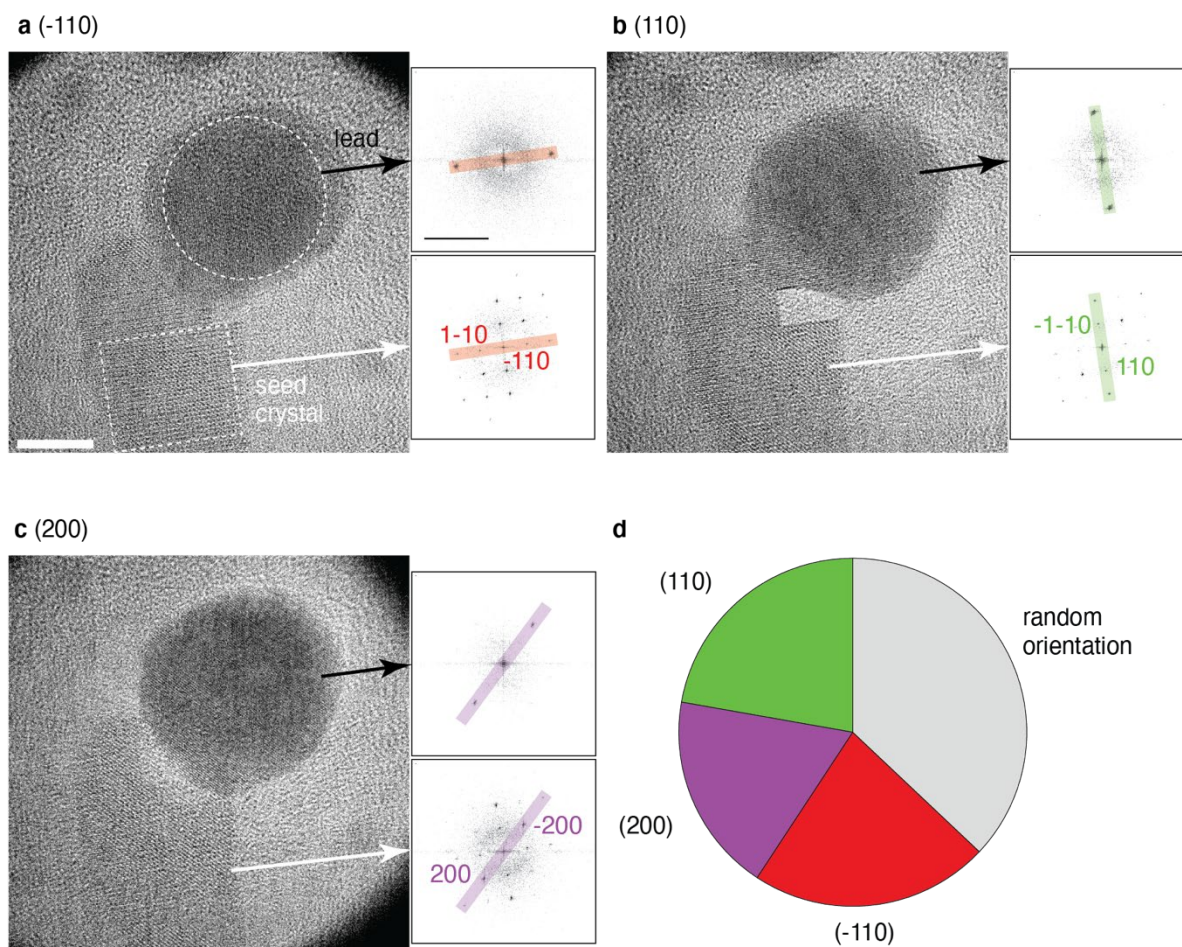


c Electron pulses (600 μ s)



Supplementary Figure 3. Drift-corrected imaging with microsecond electron pulses in the presence of beam-induced drift. (a, c) Drift-corrected images of an ensemble of gold nanoparticles on lacey carbon in a sample area that exhibits large beam-induced drift. The

micrograph in (a) is acquired with a continuous electron beam, while that in (c) is recorded with 600 μs electron pulses. Diffractograms of the area marked with a rectangle reveal several reflections of the gold nanoparticles that are present when the sample is imaged with electron pulses, but weaker or absent when the image is recorded with a continuous beam. Scale bars are 50 nm and 2.5 nm^{-1} . (b, d) Drift path of the specimen during acquisition of the images in (a) and (c), respectively.



Supplementary Figure 4. Crystallization of an individual lead nanoparticle. (a-c) Representative images of different configurations of the lead nanoparticle of Fig. 4a-f of the main text after in situ melting and recrystallization (500 μ s laser pulses, 1 mW). Diffractograms of the lead particle (circle in a) and the adjacent perovskite nanocrystal (rectangle in a) reveal that crystallization preferentially occurs with the lattice planes of both particles aligned (highlighted in the diffractograms), suggesting that the perovskite nanocrystal acts as a nucleation seed. Scale bars, 10 nm and 5 nm^{-1} . (d) Distribution of the orientations of the lattice planes of the lead particle at the interface with the perovskite nanocrystal. In about one third of cases (27 total), the crystal orientation appears to be random. In the remaining cases, the lattice planes of the lead particle are parallel to one of three sets of lattice planes of the perovskite.

A1.4 References

1. Grant, T., Rohou, A. & Grigorieff, N. cisTEM, user-friendly software for single-particle image processing. *eLife* 7, e35383 (2018).
2. Bronsgeest, M. *Physics of Schottky electron sources*. Jenny Stanford Publishing, (2014)

Appendix II - Supporting information for Chapter 4

A2.1 Single-particle reconstructions

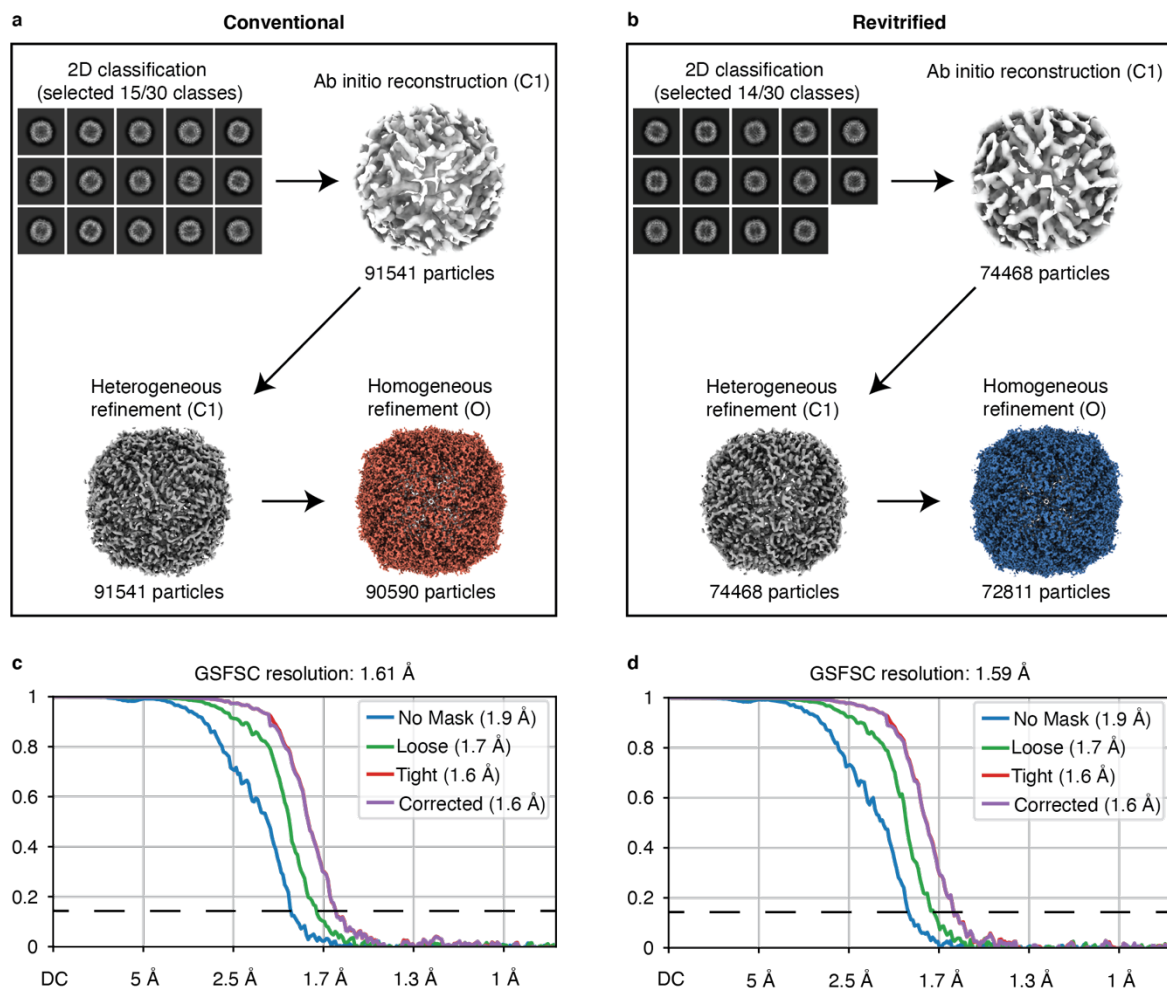
The conventional (revitrified) dataset was processed in CryoSPARC 3.3.1,¹ using 40 fractions and no upsampling. After patch motion correction, CTF estimation yielded 1815 (1552) images with a resolution better than 6.0 Å and relative ice thickness between 1.0 and 1.15, which were retained for further processing. For the revitrified data set, care was taken to exclude images from outside of the revitrified areas.

Particle picking was conducted with the following procedure. Initially, we applied blob picking to the images in the conventional dataset, using a radius between 110 and 120 Å. We then selected 127113 of the 228751 particles picked, based on their NCC and power score, and extracted them with a box size of 560 pixels. Afterwards, we performed one round of 2D classification, with 50 classes. We selected the 16 classes of the highest quality, containing 53418 particles, and used them as a template for template-based particle picking on both datasets. This procedure yielded 730858 (672391) particles, which we selected based on their NCC and power scores. Finally, we extracted the 146702 (113632) remaining particles with a box size of 560 pixels, yielding a total of 114414 (88004) particles.

Reconstructions were obtained with the following procedure. The 114414 (88004) selected particles underwent a first round of 2D classification, with 50 classes. The 92890 (76655) particles belonging to the 12 (14) best classes underwent a second round of 2D classification, this time using a circular mask of 150 Å and 30 classes. The best 15 (14) classes, containing 91541 (74468) particles, were manually selected and used for ab-initio reconstruction, with 2

classes and C1 symmetry. Particles belonging to both classes were then used for a round of heterogeneous refinement, using 2 classes and C1 symmetry. The 90590 (72811) particles belonging to the most populated class were used for a final homogeneous refinement, imposing O symmetry. This last refinement step was performed using per-particle defocus optimization, per-group CTF refinement, and implementing Ewald sphere and anisotropic magnification correction. The procedure yielded a final map at 1.61 Å (1.59 Å), as determined by the Gold Standard Fourier Correlation Shell (GSFSC) at 0.143.

A2.2 Supplementary Figure



Supplementary Figure S1. Details of the workflow for single-particle reconstructions from conventional and revitrified sample areas. (a, b) Workflow for the single-particle reconstructions of apoferritin from conventional (a) and revitrified (b) sample areas. (c, d) Gold Standard Fourier Shell Correlations (GSFSCs) for the conventional (c) and revitrified (d) datasets, with the dashed black line indicating the 0.143 cutoff.

A2.3 References

1. Punjani, A., Rubinstein, J. L., Fleet, D. J. & Brubaker, M. A. cryoSPARC: algorithms for rapid unsupervised cryo-EM structure determination. *Nat Methods* 14, 290–296 (2017).

Appendix III - Supporting information for Chapter 5

A3.1 Single-particle reconstructions

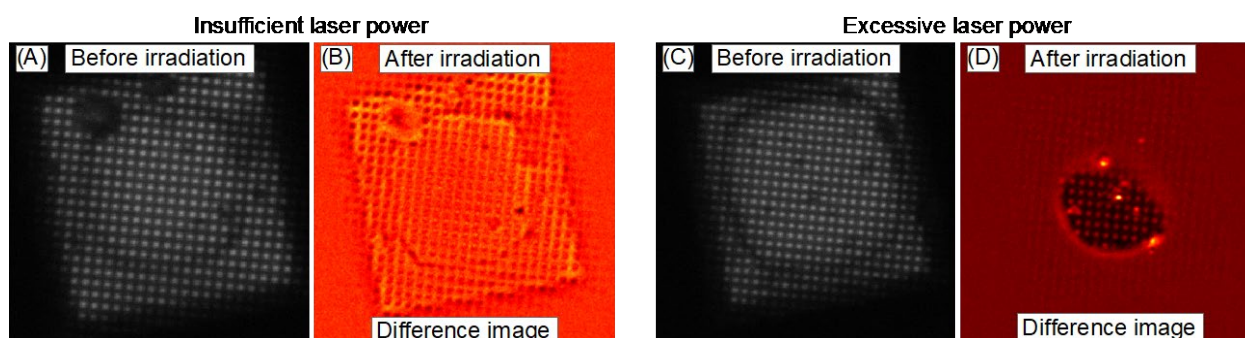
The conventional (revitrified) apoferritin dataset consists of 10145 (12047) movies in EER format, which were processed with CryoSPARC 3.3.2 (Punjani et al., 2017), using 40 fractions and no upsampling. Patch motion correction and CTF estimation were performed on all videos with default settings, yielding 6242 (3671) micrographs with a resolution below 6 Å and a relative ice thickness between 1.0 and 1.1, which were kept for further processing.

The following procedure was used to perform template-based particle picking on both data sets. First, blob picking was applied to the remaining images of the conventional dataset, using a radius between 110 and 120 Å. The 881837 particles found were then filtered based on the NCC and power score. The remaining 596829 particles were extracted with a box size of 560 pixels and Fourier cropped to 256 pixels. After 2D classification with 50 classes, the 12 classes of highest quality were manually selected (222088 particles). Using these classes for template-based particle picking yielded 2937383 (1714924) particles for the conventional (revitrified) dataset. Particles with an NCC score above 0.34 were then extracted with a box size of 560 pixels and Fourier cropped to 256 pixels, yielding a total of 727135 (355918) particles.

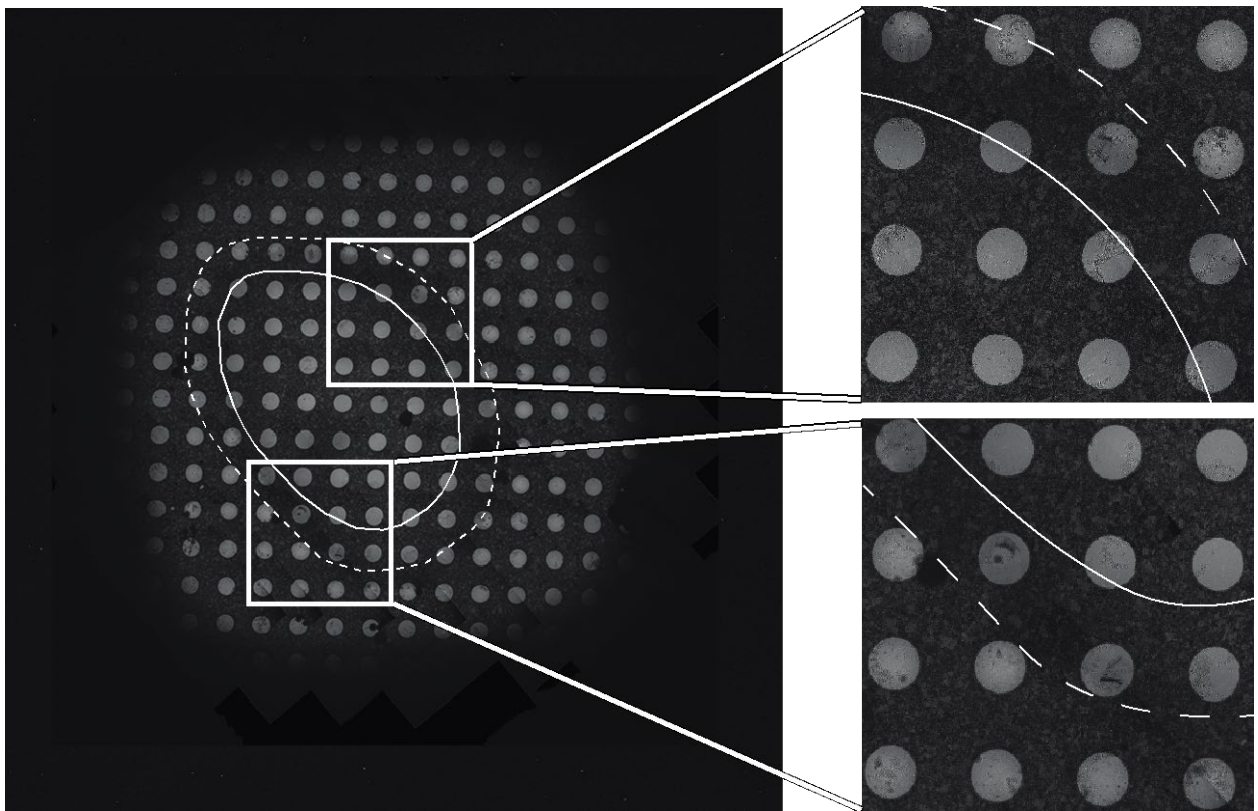
Reconstructions were obtained with the following procedure. The selected particles were subjected to 2D classification with 50 classes, and the best 29 (18) classes were manually selected. The remaining 645679 (264590) particles were subjected to a second round of 2D classification with 30 classes (150 Å circular mask), of which the best 11 (9) classes were

manually selected. The remaining 534606 (212377) particles were used for ab-initio reconstruction with C1 symmetry and 3 classes. Subsequently, two rounds of heterogeneous refinement were performed with 3 classes, using C1 symmetry in the first iteration and O symmetry in the second. After each iteration, the scarcely populated classes were rejected. The remaining particles were then re-extracted with a box size of 600 pixels (without Fourier cropping), leaving 451420 (957860) particles. Homogeneous refinement with O symmetry, using per-particle defocus optimization, per-group CTF refinement, correction of magnification anisotropies, and Ewald sphere correction yielded a 1.47 Å (1.63 Å) resolution map (Gold Standard FSC at 0.143).

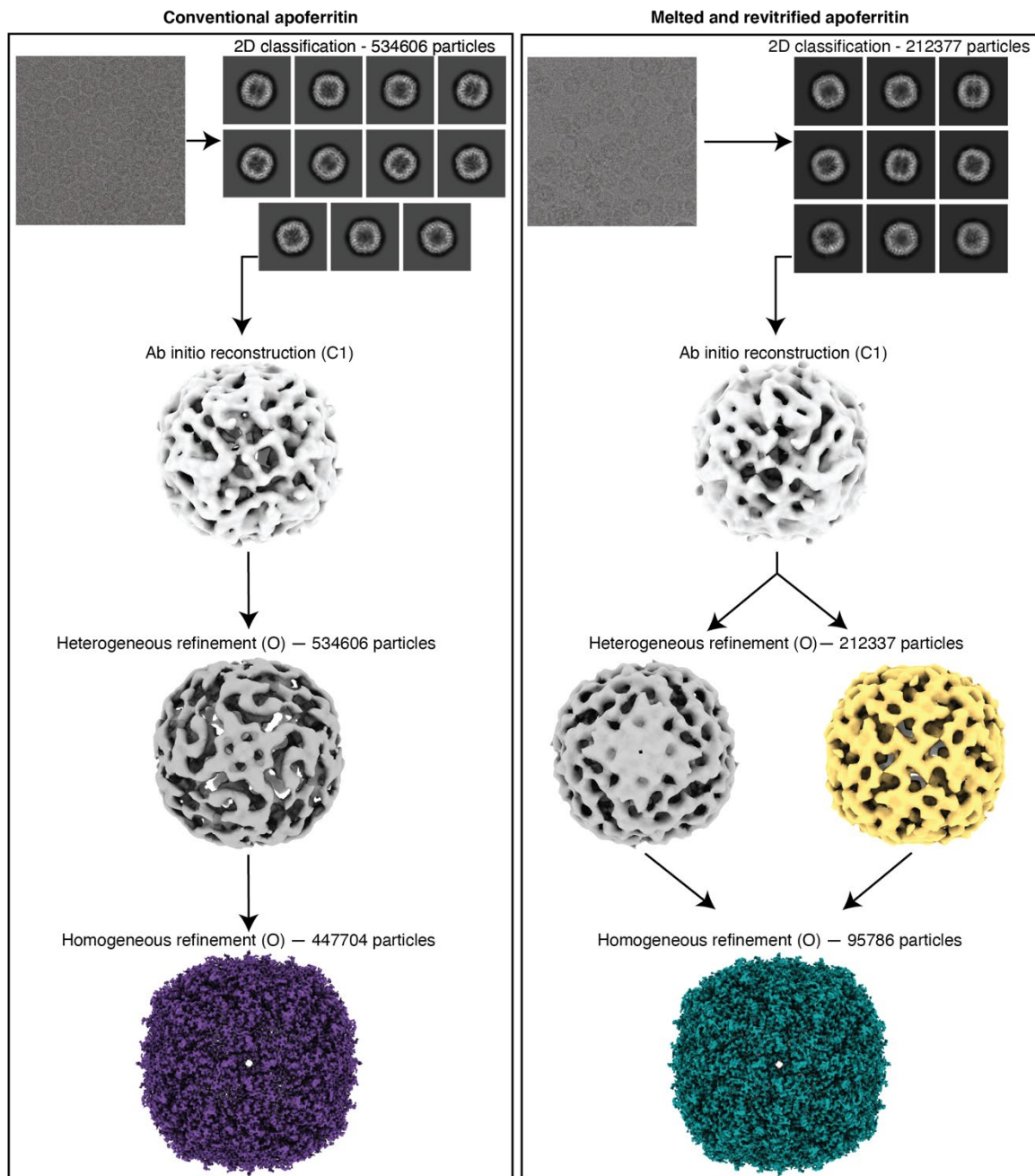
A3.2 Supplementary Figures



Supplementary Figure S1. Optical micrographs of unsuccessful revitrification experiments. (a, b) Insufficient laser power. The difference image (b) does not exhibit the characteristic contrast changes associated with successful melting and revitrification that can be seen in Fig. 2b. Most features in the difference image correspond to structures visible before laser irradiation (a) and therefore likely arise from a change in defocus due to a deformation of the specimen grid under laser irradiation. (c, d) Excessive laser power. The sample evaporates in the center of the grid square, which leads to strong contrast changes in the difference image, with the holey gold film appearing dark in the evaporated area, and the holes bright.



Supplementary Figure S1. Electron micrograph of the revitrified cryo sample from Fig. 2(c) with details of the boundary between the revitrified and crystalline areas. The outline of the revitrified area is marked with a solid line. A dashed line indicates the region in which the formation of large crystals is observed, which causes a thin, dark outline to appear in the optical difference image of Fig. 2(b).



Supplementary Figure S3. Workflow for the single-particle reconstructions of apoferritin from conventional and vitrified sample areas.

Acknowledgments

The work described in this thesis would not have been possible without the help and support of several amazing people.

First of all, I would like to thank my Ph.D. advisor, Professor Ulrich J. Lorenz for the continuous support, feedback and advice throughout these years. Joining the “crazy but not dangerous” lab was truly a unique experience where I had the opportunity and the freedom to explore a wide range of very different scientific fields, while learning how to conduct research.

I would also like to thank past and present members of the LND group. Professor Marcel Drabbels for the discussions and the invaluable help that made this research possible; Annick Gaudin who was always readily available to help with the administrative work; Dr. Pavel Olshin who taught me a great deal of experimental work and shared with me many of the projects of these years; Dr. Jonathan Voss and Oliver Harder for introducing me to cryo-EM and transferring their hard-earned knowledge; Constatin Krüger and Nathan Mowry for the amazing time exploring “No Man’s Land”; Chengcheng Yan for the many evening discussions throughout these years; and of course, all the members of the group with whom I shared countless lunch breaks, discussions, jokes and whiteboard memes.

This work would not have been possible without many other experts working at the EPFL facilities. The modifications of the electron microscope were realized thanks to the amazing work of the Mechanical and Electrical workshops, in particular André Fattet, Yves Morier, and Benjamin Le Geyt, without whom we would not have anything more than a few (incorrect)

CAD designs and ideas on paper. I would also like to thank Lionel Cachoulet from JEOL for the invaluable help in setting up the microscope at the very beginning of the Ph.D.

Cryo-EM reconstructions were possible thanks to Dr. Kevin Lau who prepared amazing apoferritin samples, and Dr. Alex Myasnikov, Dr. Bertrand Beckert and Dr. Sergey Nazarov of the Dubochet Center for Imaging, where we collected all the images that resulted in the 3D reconstructions of this thesis.


I would also like to thank the members of my committee, Prof. Jiri Vanicek, Prof. Henning Stahlberg, Prof. David Flannigan, and Prof. Angus Kirkland for their availability and feedback.

I would like to thank all the people that I have met during these years and / or have supported me unconditionally. I would like to thank the "Nanotech invasion in Switzerland", The Buddies / The Quizards, and, of course, M., who was there for all the goods and the bads.

Lastly, I would like to thank my family and friends in Turin, from supporting me from the very beginning.

GABRIELE BONGIOVANNI

Lausanne, Switzerland

☎ [+41-782486829](tel:+41782486829) ✉ gabriele.bongiovanni@epfl.ch  [Gabriele Bongiovanni](#)

EDUCATION

- Ph.D. in Physical Chemistry, group of Prof. U. Lorenz** **10-2018 – Ongoing**
École polytechnique fédérale de Lausanne (EPFL) *Lausanne, Switzerland*
- M.Sc. Nanotechnologies for the ICTs** **09-2016 – 09-2018**
Politecnico di Torino - Final grade: 110/110 cum laude *Turin, Italy*
- B.Sc. Physical Engineering** **09-2013 – 09-2016**
Politecnico di Torino - Final grade: 110/110 *Turin, Italy*

MAIN RESEARCH PROJECTS


- Microsecond time-resolved cryo-electron microscopy: method development** **Ongoing**
 - Approach to image **protein dynamics** with microsecond temporal resolution
 - Development of an **automated optical setup** for laser melting and revitrification of cryo samples
- Electron diffraction of water in "No Man's Land"** **Ongoing**
 - Development of a **fully-automated time-resolved setup** for **electron diffraction**
 - Elucidation of the structural dynamics of deeply supercooled water
- Microsecond time-resolved electron microscopy at near atomic-resolution** **01-2021**
 - Modification of a commercial transmission electron microscope
 - Generation and characterization of **bright microsecond electron pulses**
 - Demonstration of **microsecond time-resolved** electron microscopy at **near atomic-resolution**

FIRST AND JOINT-FIRST AUTHOR PUBLICATIONS

Electron diffraction of water in No Man's Land

Constantin R. Krüger, Nathan J. Mowry, Gabriele Bongiovanni, Marcel Drabbels, Ulrich J. Lorenz. ArXiv, 2022 


Microsecond melting and revitrification of cryo samples with a correlative light-electron microscopy approach

Gabriele Bongiovanni, Oliver F Harder, Marcel Drabbels, Ulrich J Lorenz, Front. Mol. Biosci., 10 November 2022 

The fragmentation mechanism of gold nanoparticles in water under femtosecond laser irradiation

Gabriele Bongiovanni, Pavel K. Olshin, Chengcheng Yan, Jonathan M. Voss, Marcel Drabbels and Ulrich J. Lorenz, Nanoscale Adv., 2021, 3, 5277-5283 

Atomic-resolution imaging of fast nanoscale dynamics with bright microsecond electron pulses

Pavel K. Olshin, Gabriele Bongiovanni, Marcel Drabbels, and Ulrich J. Lorenz, Nano Lett. 2021, 21, 612–618 

Intense microsecond electron pulses from a Schottky emitter

Gabriele Bongiovanni, Pavel K. Olshin, Marcel Drabbels, and Ulrich J. Lorenz, Appl. Phys. Lett., 2020, 116, 234103 